A NOVEL FRAMEWORK FOR MONITORING OIL SPILL FROM MOVING VESSELS USING SYNTHETIC APERTURE RADAR

by

Lizwe Wandile Mdakane

Submitted in partial fulfillment of the requirements for the degree

Philosophiae Doctor (Electronics)

in the

Department of Electrical, Electronic and Computer Engineering

Faculty of Engineering, Built Environment and Information Technology

UNIVERSITY OF PRETORIA

June 2018

SUMMARY

A NOVEL FRAMEWORK FOR MONITORING OIL SPILL FROM MOVING VESSELS USING SYNTHETIC APERTURE RADAR

by

Lizwe Wandile Mdakane

Promoter(s):	Dr. W. Kleynhans
Department:	Electrical, Electronic and Computer Engineering
University:	University of Pretoria
Degree:	Philosophiae Doctor (Electronics)
Keywords:	SAR, Image processing, Machine Learning, Oil spill

Operational discharges of oil from vessels, whether accidental or deliberate, are a growing concern as the levels of maritime traffic increase. Oil tankers and other kinds of ships are among the suspected offenders of illegal discharges. The international legislation contains minor and well-defined exceptions related to ocean areas (internal waters, marine protected areas, MARPOL "special" areas, territorial seas or exclusive economic zones). These areas often determine whether an action is considered legal or not and define the rights and obligations, including law enforcement obligations.

Synthetic aperture radar (SAR) is the most used remote sensing tool for monitoring oil pollution over vast ocean areas. SAR is an active microwave RS sensor capable of taking measurements day or night and almost independently from atmospheric conditions. Manual oil spill detection in a SAR image is ordinarily done by a trained human interpreter who visually inspects SAR images for any possible spills. However, manual inspection can be time-consuming, biased, inconsistent and subjective. A faster and more robust alternative is to use automated image processing and machine learning methods. The current automated oil detection methods, however, are still not ideal and there is still a need for improvement. Also, data costs have resulted in limited studies on oil spill detection in African oceans. The launch of several Sentinel missions with SAR sensors has considerably improved coverage and

accessibility of data over African oceans. The goal of the study is to develop an automated detection of oil spill discharges from vessels in African seas using the freely available Sentinel SAR data.

A novel oil spill detection framework that can detect possible oil spill candidates and remove unwanted detections (i.e., false positives) was proposed. The framework used a novel linear dark spot detection algorithm and an improved oil spill discrimination process. The linear detection process used a segmentation-based algorithm to isolate linear dark spots (potential oil spills) from other features in the image. The process involved a more efficient feature selection and classification process. The proposed linear detection algorithm was evaluated for detection accuracy and compared to other segmentation-based oil spill detection algorithms, including state-of-the-art oil spill detection methods. The results demonstrated the proposed approach to be a more efficient and robust linear dark spot detection method. An improved discrimination process was presented to reduce false detections from a segmentation-based algorithm. The selection of relevant oil spill features depends on many factors which could influence the accuracy of the classification task. Automated features selection methods were thus considered to improve the discrimination process. Using feature selection, the most significant oil spill features with minimum variations were determined. The significant features were used as input vectors to classify oil spill events from moving vessels. An optimised Gradient Boosting Tree Classifier (GBT) was used for the classification task.

The proposed novel framework showed promising results for monitoring oil spill from moving vessels using SAR in African oceans on a regular basis. Future work includes adding a confidence measure and alert level estimation. The system will incorporate ancillary information such as the oil spill source and the sensitivity of the polluted area to measure environmental impact.

LIST OF ABBREVIATIONS

ACM	Active Contour Model
AdaBoost	Adaptive Boosting
AIS	Automatic Identification System
ANN	Artificial Neural Network
ANOVA	Analysis of Variance
ALOS	Advanced Land Observing Satellite
ASAR	Advanced SAR (Envisat)
ASI	Italian Space Agency
AUC	Area Under Curve
C-band	Frequencies of about 5 GHz
COSMO-SkyMED	COnstellation of small Satellites for Mediterranean basin Observation
CSA	Canadian Space Agency
dB	Decibels
DA	Detection Accuracy
DInSAR	Differential Interferometric SAR
EEZ	Exclusive Economic Zone
EM	Electromagnetic
ENVISAT	Environmental Satellite
EO	Earth Observation
ERS	European Remote-Sensing
ESA	European Space Agency
EW	Extra Wide
FAR	False Alarm Rate
FN	False Negative
FP	False Positive
FPR	False Positive Rate
GBT	Gradient Boosted Tree
GCP	Ground Control Point
GeoTIFF	Georeferenced Tagged Image File Format
GHz	Gigahertz
GRDM	Ground Range Detected Medium

HH	Antenna that transmits and receives with an H-pol
H-pol	Horizontally polarized
HV	Antenna that transmits with an H-pol and receives with a V-pol
Hz	Hertz
IEEE	Institute of Electrical and Electronics Engineers
IMO	International Maritime Organization
InSAR	Interferometric SAR
IR	Infrared
IW	Interferometric Wide
JAXA	Japan Aerospace Exploration Agency
JERS	Japanese Earth Resources Satellite
JPL	Jet Propulsion Laboratory
L-band	Frequencies of about 1 GHz
LiDAR	Light Detection And Ranging
LUT	Look Up Table
MARPOL	Marine Pollution
MDA	Maritime Domain Awareness
MHz	Megahertz
MMSE	Minimum Mean Square Error
MODIS	Moderate Resolution Imaging Spectroradiometer
NASA	National Aeronautics and Space Administration
NRCS	Normalised Radar Cross Section
NIR	Near Infrared
NOAA	National Oceanic and Atmospheric Administration
OWS	Oily Water Separator
PALSAR	Phased Array type L-band SAR
PRF	Pulse repetition frequency
RADAR	Radio Detection and Ranging
RADARSAT	Radar Satellite
RCM	Radarsat Constellation Mission
RFE	Recursive Feature Elimination
ROC	Receiver Operating Characteristic
ROI	Region Of Interest

SAR	Synthetic Aperture Radar
Sat-AIS	Satellite AIS
ScanSAR	Wide-swath SAR imaging mode
SCNA	ScanSAR Narrow Band-A
SeaSAT	Sea Satellite
SLAR	Side Looking Airborne Radar
SLC	Single Look Complex
SLR	Side-Looking Radar
SM	Stripmap Mode
SNR	Signal to Noise Ratio
SPF	Signed Pressure Force
SVM	Support Vector Machine
TIR	Thermal Infrared
TN	True Negative
TP	True Positive
TPR	True Positive Rate
TRM	Transmit/Receive Modules
UAV	Autonomous Underwater Vehicle
UV	Ultraviolet
VH	Antenna that transmits with a V-pol and receives with an H-pol
VIR	Visible/Infrared
VNIR	Visible/Near-Infrared
V-pol	Vertically polarized
VV	Antenna that transmits and receives with a V-pol
WV	Wave Mode
WGS84	World Geodetic System 1984
X-band	Frequencies of about 10 GHz

TABLE OF CONTENTS

CHAPTER 1 INTRODUCTION

1.1 PROBLEM STATEMENT

1.1.1 Context of the problem

Petroleum products play an essential role in the transportation, plastics and fertiliser industries [1]. Liquid petroleum hydrocarbon (oil) products consist of various unrefined and refined liquid components. Unrefined petroleum (crude oil) are dense hydrocarbon compounds that from small volatile to large non-valotile compounds [2]. Petroleum products are mixtures of fewer hydrocarbon compounds that are more specific and less variable. Examples of petroleum products include gasoline and diesel fuel. Crude oil and other oil products are predominantly (about 90% [3]) are transported across the ocean using oil-tankers. The massive oil quantities carried by ships often results in an almost inevitable risk of oil pollution. There can be as many as 10–15 transfers involved in the moving of oil [1]. Oil spills can happen in water, ice or on land during oil shipping or storage [4]. Once the oil is spilt, it soon spreads to create a thin oil film on the ocean surface, known as an oil-slick, see example in Fig. 1.1. In this thesis, the terms oil spill, oil slick and bilge dumps refer to maritime oil pollution released due to human activity into the ocean environment.

Oil spills are a result of the intentional or unintentional release of oil to the ocean environment, see Fig. 1.2. Accidental oil spills are mainly caused by oil tankers or on offshore oil platforms and can result in massive quantities spills which often attract a lot of media attention. Deliberated oil spill are often caused by vessels illegally discharging oily waste during cleaning operations. A vessel's oil leaking from the engine and other debris is stored in a vessel storage area called a bilge. A bilge (also known as a bilge well) is found in the bottom of part of a ship and is used to store water waste from the daily routine operations of vessels. Bilge waste includes lubricating oil, cleaning diesel oil, oily

Figure 1.1. Oil slick floating (dark substance) on the ocean surface. Taken from [5], with permission.

sludge, spills from the engine room, water leaks from internal pipes and seawater filtrations. The law requires the retrieval of oily bilge waste-water to be in the harbours. However, vessels often dump bilge waste before entering a port in efforts to save costs and time spent at the port [6, 7]. Commonly fewer quantities of oil are spilt during illegal bilge dumping. However, it happens so frequently that bilge dumping is the highest contributor to ocean oil spills. In fact, discharges of bilge and fuel oil are comparable to about five Exxon-Valdez oil spills (one of the most significant recorded oil spills in the United States) yearly [8, 9]. The rate of oil pollution from ships is expected to rise as the levels of maritime activities increase [7].

Oil spill over the sea surface often results in significant damage to the ocean environment, plants and animals. The impact depends on the location, season, amount, toxicity, oceanic conditions and the length of exposure to the oil. The consequences on the environment of the marine ecosystem is especially destructive after a massive oil spill caused by a marine accident. The plants and animals that come into contact with the oil contaminated ocean surface are the most at risk [3], see Fig. 1.3. In addition to the impact on the maritime ecosystem, oil spills can also have a damaging effect on the economic, social and natural resources in the coastal and marine protected areas [11]. Tourism and

Figure 1.2. Image showing oil spill (brown substance) caused by a vessels. Taken from [10], with permission.

recreation activities may be affected by an oil spill that drifts to coastal areas. Oil-tainted seafood may be toxic to humans and can also affect their economic value. Cleaning up processes can be very costly (ranging from 40 to 400 US dollars per litre) depending on the type and location (shorelines are the most expensive) of the oil spill [12]. A rapid response to all oil spill events is required to minimise the ecological impact produced.

The harmful impact of oil spills on the maritime ecosystem led to the creation of the International Convention for the Prevention of Pollution of the Sea by Oil in 1954 [13]. The convention defined international laws that prohibited any oil spill at the ocean. The rules were able to decrease the number of vessels that are illegally dumping bilge waste at sea. However, there is still sufficient evidence of numerous and repeated illegal bilge dumping offences. Most illegal bilge dump events usually occur offshore, prior to a ship arriving at a port, where surveillance is limited. Advancements in remote

Figure 1.3. Dead fish due to an oil spill incident. Taken from [14], with permission.

sensing technology can assist operators to detect oil spills before they cause widespread damage. Remote sensing uses imaging sensors aboard airborne or spaceborne platforms to capture large areas over the Earth's surface at a high altitude. Spaceborne platforms can cover larger areas at a lower cost than airborne and they are mostly used to find potential oil spills before sending airborne platforms to confirm the spill. Remote sensing consists of various imaging sensors across the electromagnetic spectrum.

Synthetic aperture radar (SAR) has been demonstrated to be the key sensor for oil slick observation [15, 16, 17]. SAR is the most used remote sensing (RS) tool for monitoring oil pollution over vast ocean areas. It is an active microwave RS sensor capable of making measurements day or night and almost independently from atmospheric conditions [18, 19, 20, 21]. The ocean's short gravity waves reflect radar energy, resulting in a bright SAR image. The presence of an oil spill dampens the gravity waves and reduces the energy returning to the radar sensor, resulting in a darker patches (denoted as a darkspots). The dampening effect allows oil spills to be detected from a SAR image. However, the

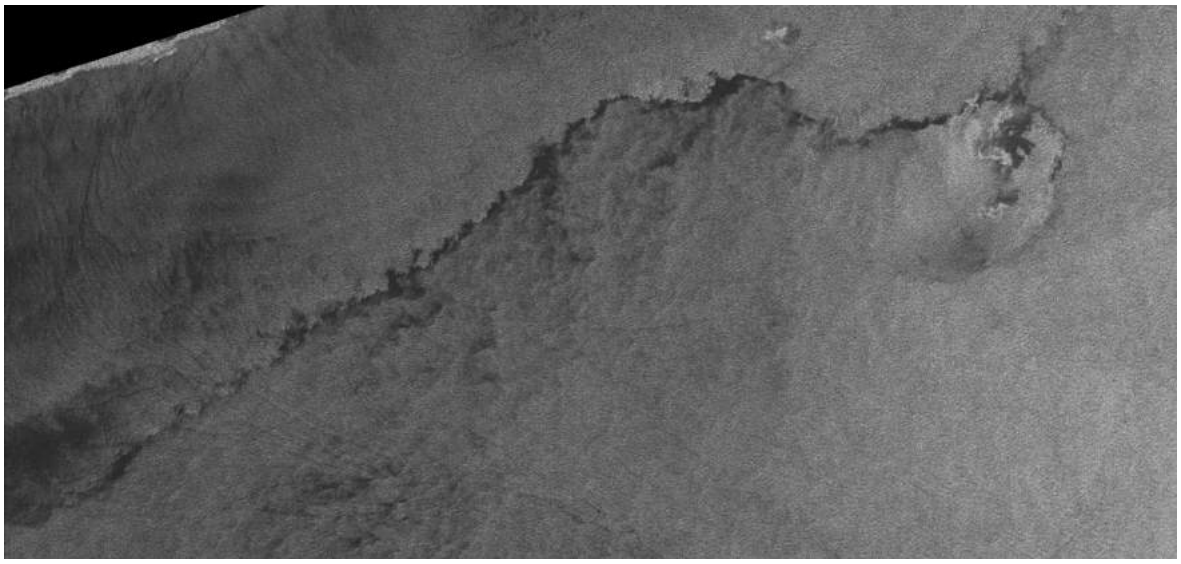

Figure 1.4. SAR image showing dark region caused by look-alike.

dampening effect is not unique to oil spills; other natural phenomena exhibit a similar effect which introduces false alarms in the detection chain which can be a challenge, see Fig. 1.4. False alarms mostly consist of naturally occurring phenomena known as oil spill look-alikes which can resemble oil spills (e.g., natural seepage). Despite the limitations, trained operators are often able to discriminate between natural phenomena and discharges from vessels by analysing spill candidate shape, the ocean conditions and the proximity of the vessel responsible. Key features from SAR images include a linear dark region with a bright spot at the end, representing the vessel responsible, see illustration in Fig. 1.5.

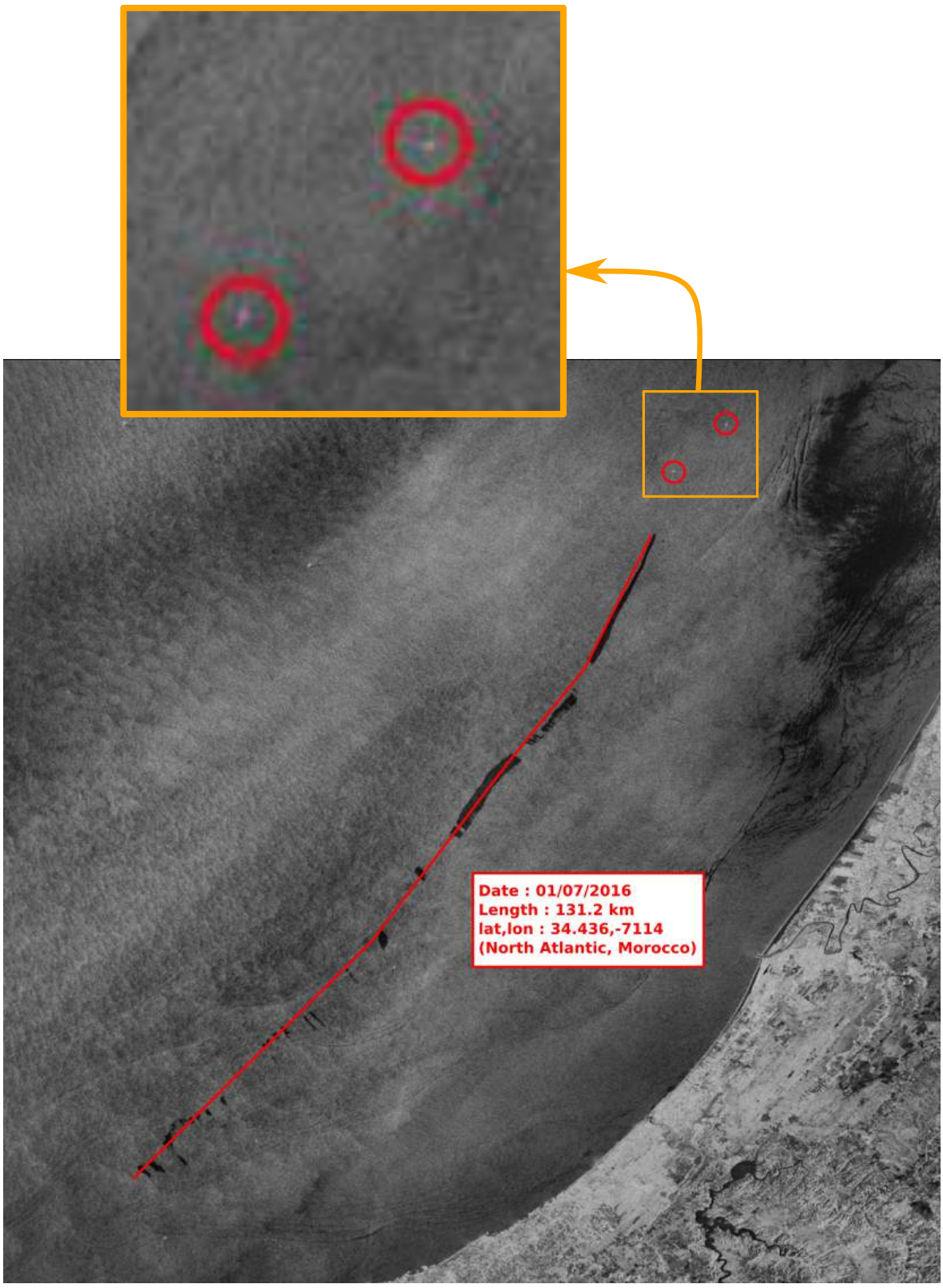

Figure 1.5. SAR image captured in Morocco showing oil spill (red line) and possible vessel spill sources (red circles within the orange box).

1.1.2 Research gap

SAR imagery may be regularly acquired over the ocean, but the images still need to be inspected and analysed for any potential oil spill. This step is usually time sensitive as the offender is normally moving and the oil samples are required for prosecution. Thus oil spill monitoring agencies need to inspect SAR images for oil spills as soon as possible. Manual or automatic techniques can be used to detect and quantify ocean oil spills using SAR imagery. Manual inspection involves a human operator, usually an expert in the field, to analyse all the images visually. The limitations of manual inspection are that it depends on the knowledge of the operator and can be a biased, non-repeatable process. SAR images can be huge and thus time-consuming to analyse, particularly the small illegal oil spills from bilge dumping. Oil spill discharges from ships can also be monitored automatically using image processing methods on SAR images. Usually, a semi-automated approach is adopted where an image processing algorithm is used to detect potential oil spills and the operator verifies the detections to reduce false alarms. A lower rate of false alarms is essential as law enforcement needs to dispatch a team to confirm and apprehend the offender. An ideal system is a fully-automated approach where image processing with a machine learning algorithm is used to detect potential oil spills and remove false targets. This information can help operators and air patrols to plan countermeasures to lessen the pollution effects efficiently.

Ocean pollution monitoring application has shown automated methods to be faster and more robust when compared to manual inspection by an expert and thus can be used to supplement manual inspection. However, designing an automated oil spill detection system is no small feat. The ocean is too vast to monitor all oil spill events, particularly when the area has limited SAR satellite coverage. Many SAR images or oil spill examples are often required to develop a robust algorithm as it needs to be trained on a more extensive set of possible examples of oil spill events. The second issue is that natural phenomena that look like oil spill events (known as look-alikes) appear much more frequently than the actual oil spill events. Because of this issue, further manual analysis is recommended to verify each automated detection. Lastly, oil spill events mostly appear in batches, that is, all oil spills extracted from a single image constitute a single batch. The issue here is that similarities and dissimilarities between batches (e.g., difference in image quality and ocean conditions) can influence the training of automated methods. However, even with the outlined challenges above, SAR's capability to detect oil spills is vital for maritime pollution surveillance, particularly for monitoring large areas, day or night, under any weather condition.

The detection of oil spills caused by vessels using SAR can be a challenging task that requires an accurate representation of potential oil spill events. There have been many studies of ocean pollution detection, however, only a few studies have been done on oil slick monitoring using SAR data for Africa's oceans. The limited studies are mainly due to the lack of data in these areas. However, these areas can now be monitored because of the increase in free global SAR data. Also, more work is needed on developing an automated oil spill detection approach that is accurate enough to discern between real and false targets. Especially since the detection of oil spills in SAR is highly susceptible to these look-alikes, particularly at low and high wind speed.

1.2 RESEARCH OBJECTIVE AND QUESTIONS

The primary objective is to detect oil spills from vessels from SAR imagery using image processing and machine learning methods. This research will answer the following questions:

- What are the current state-of-the-art methods for oil spill monitoring using SAR?
- Can automated detection of the oil spill caused by vessels using SAR imagery be improved?
- What are the limitations, given the data availability of Africa's oceans?

1.3 HYPOTHESIS AND APPROACH

The study propose an improved oil spill detection system. The main hypothesis is: **Automated detection of oil spill caused by vessels using SAR imagery can be improved**. The system is developed using the following approach:

- The current state-of-the-art methods for automated oil spill detection is established from a comprehensive review of literature.
- Darkspot detection is regarded as the most critical step for a successful oil spill detection system. Therefore, the first step is to develop an improved darkspot detection method.
- A discrimination step is required to separate man-made oil spill from false targets (i.e., oil spill look-alikes). The study further improves the proposed system by developing a more robust discrimination step.

1.4 RESEARCH GOALS AND CONTRIBUTION

Oil spill detection using SAR has been successfully demonstrated since the early 90's. The current automated methods, however, are still not ideal and there is still a need for improvement. Also, there have been limited studies on oil spill detection in the African oceans. Even though the current oil spill detection methods are expected to work for any ocean, it is still necessary to test them in African oceans.

Illegal operational oil discharges from vessels have been demonstrated to exceed that of large-scale tanker accidents. The goal of this study to develop an automated detection system of oil spill discharges from vessels using SAR data. The second goal is to demonstrate the use of a SAR based automated oil spill monitoring system in an African context and encourage the operational use of SAR data to monitor these oceans.

The contribution of the study is towards the development of a novel automated oil spill detection system based on SAR data. The work also contributes to the lack of an automated system for ocean pollution monitoring in Africa's coastal areas. As part of the research, the original contributes were published to a high-ranking peer-reviewed journal (IEEE J-STARS) and were discussed in remote sensing conferences (IEEE IGARSS Conference).

1.5 OVERVIEW OF STUDY

The study is divided into several chapters that follow five main categories.

Introduction chapter

The scope, objectives and contribution of the work is presented in the Introduction chapter, see chapter (1 on page 1). The chapter also discusses the context of the study by clearly stating the research gap, formulating several research questions and approaches to solve them.

Background chapters

The background, theory and current state-of-the-art methods relevant to oil spill detection using SAR data are presented. The study split the background into four chapters with topics discussing:

- **Maritime Oil Pollution** (chapter 2, page 12): presenting an overview of the ocean pollution sources, impact and response.
- **Oil Spill Remote Sensing** (chapter 3, page 28): presenting monitoring efforts using remote sensing.
- **Oil Spill Imaging using SAR** (chapter 4, page 40): presented a technical description of oil spill imaging using SAR.
- **Oil Spill Detection using SAR** (chapter 5, page 58): presented a literature review on automated image processing techniques.

Methodology chapter

The methodology chapter presents the description of the proposed novel oil detection framework, see chapter 6 on page 71. The chapter presents the mathematical formulation and implementation of The novel segmentation-based linear dark-spot detection algorithms and the improved oil spill discrimination algorithms.

Results and discussion chapter

This chapter presents the results and analysis of the proposed segmentation-based algorithm methods and the improvement of using the proposed discrimination process, see chapter 7 on page 91. The chapter also presents a dataset description section describing the study area, SAR dataset and the preprocessing chain.

Conclusion chapter

The conclusion chapter presents final remarks and future recommendations for similar work, see chapter 8, page 120. Final remarks present a recap of the noteworthy details of the study.

CHAPTER 2 MARITIME OIL POLLUTION

2.1 OIL SPILL SOURCE

According to the United Nations Convention on the Law of the Sea, 1982:

> Marine pollution is the introduction by man, directly or indirectly, of substances or energy into the marine environment, including estuaries, which results or is likely to result in such deleterious effects as harm to living resources and marine life, hazards to human health, hindrance to marine activities, including fishing and other legitimate uses of the sea, impairment of quality for use of sea water and reduction of amenities [22].

Oil spills occur because of natural and man-made sources, see Table 2.1. There are two types of oils, that is, biogenic oils and mineral oils [23]. Biogenic oils occur because of ocean plants and animal growth. Biogenic oil spills appear as a thin layer of oil over the sea surface [24]. Mineral oils appear as a thick layer that consists of different mixtures of refined petroleum products including crude oil [2].

2.1.1 Natural oil spill

Not all oil spills originate from man-made activities. Natural geological sources, named oil seeps, can release a natural oil spill into the marine environment [2]. They appear as a thin layer of oil over the ocean surface and occur because of ocean plants and animal growth. Natural oil spills are not very soluble in water and have lower toxicity compared to petroleum products and have a little impact on the marine life [25]. The most notable effect on marine ecosystem is smothering. The Woods

Table 2.1. Oil products found on the ocean surface.

	Natural Spill	**Man-made Spill**
Biogenic Oil	Surfactants	Fish and Vegetable oil products
Mineral Oil	Oil Seeps	Crude oil and petroleum products

Hole Oceanographic Institution declares that natural seeps of oil and gas contribute as much as one half of the oil in the ocean [26, 27]. Gas bubbles coated with oil are released into the atmosphere through faults and fractures in the seabed to form a natural oil slick on the sea surface. Natural oil spills evaporate at a rate, do not disperse or mix with water through emulsions and are more persistent than crude oil.

2.1.2 Man-made oil spill

Ship accidents (collisions and groundings), illegal operational discharges and offshore production are the prominent sources of maritime oil pollution [28]. These are due to human error, negligence or equipment malfunction or failure. Accidental oil spill occurs in large quantities and are mainly due to accidents or equipment failures. They can be caused by both vessels and oil platforms and often attract media attention. Deliberate bilge dumping may occur in fewer quantities, but they appear more frequently than ship accidents. Operational discharges from tankers cause 45%, where the bulk of observed oil spills correlate with vessel traffic routes. In the last decade, maritime transportation has been steadily growing which increases the potential number of illegal bilge waste discharges. About 90% of the world's oil is transported across the ocean using oil-tankers. Oil is also used as fuel to power the engines and as a lubricant for machines to run smoothly. Vessels transporting massive oil quantities, or using oil as fuel as well as large oil platforms in the ocean, often pose in an almost inevitable risk of oil pollution, see Fig. 2.1.

Figure 2.1. Image showing oil spill caused by Exxon Valdez tanker incident. (Taken from [29], with permission).

2.1.2.1 Large oil spill accidents

The Prestige tanker sunk off the coast of Galicia in 2002 and resulted in an oil leak that spanned over thousands of kilometres' of the coastline. The most massive accidental oil spill in history occurred in 2010 when the British Petrol's drilling rig Deepwater Horizon (DWH) exploded in the Mexico Gulf. The oil leaked for 87 days and released approximately 780 000 m^3 of oil in the Atlantic Ocean. Oil spill can also be caused by submarines. In 2011, an oil spill was caused by the crack of a submarine fault in the Bohai Sea, China. The accident resulted in approximately 4400 m^3 of crude oil leaking into the sea and about 15 700 m^3 of mineral oil leaking into the seabed [30], see top 20 oil spills list in Table 2.2.

Table 2.2. A summary of the top 20 major spills that have occurred globally since 1967 [31].

Ship name	Year	Location	Spill Size (tonnes)
ATLANTIC EMPRESS	1979	Off Tobago, West Indies	287,000
ABT SUMMER	1991	Off Angola	260,000
CASTILLO DE BELLVER	1983	Off Saldanha Bay, South Africa	252,000
AMOCO CADIZ	1978	Off Brittany, France	223,000
HAVEN	1991	Genoa, Italy	144,000
ODYSSEY	1988	Off Nova Scotia, Canada	132,000
TORREY CANYON	1967	Scilly Isles, UK	119,000
SEA STAR	1972	Gulf of Oman	115,000
IRENES SERENADE	1980	Navarino Bay, Greece	100,000
URQUIOLA	1976	La Coruna, Spain	100,000
HAWAIIAN PATRIOT	1977	Off Honolulu	95,000
INDEPENDENTA	1979	Bosphorus, Turkey	94,000
JAKOB MAERSK	1975	Oporto, Portugal	88,000
BRAER	1993	Shetland Islands, UK	85,000
AEGEAN SEA	1992	La Coruna, Spain	74,000
SEA EMPRESS	1996	Milford Haven, UK	72000
KHARK 5	1989	Off Atlantic coast of Morocco	70,000
NOVA	1985	Off Kharg Island, Gulf of Iran	70,000
KATINA P	1992	Off Maputo, Mozambique	67,000
PRESTIGE	2002	Off Galicia, Spain	63,000
EXXON VALDEZ	1989	Prince William Sound, Alaska, USA	37,000
HEBEI SPIRIT	2007	South Korea	11,000

Figure 2.2. Image showing an oil spill caused by a vessel on the blue ocean surface. (Taken from [35], with permission).

2.1.2.2 Oil spill from vessel discharges

Oil tankers and other kinds of vessels are among the suspected offenders of unlawful discharges [32]. Oil spills can occur from inland, coastal and ocean facilities and during transportation. Oil facilities include oil productions, oil refineries and bulk oil storage in above and below ground storage tanks. Oil transportation spills can be caused by oil pipeline ruptures, tank spills and road transportation [33, 34].

Even though the public is more aware of severe accidental oil spills, a significant proportion of oil spills are caused by deliberate discharges in the form of bilge and fuel oil from tankers or cargos [3, 30], see Fig. 2.2. Studies have reported that the cumulative impact of small spills can add up to about 10 million gallons ($\approx 30.000\,\mathrm{m}^3$) per year worldwide [8]. Illegal oil spills involve intentional discharging of oily substances over the limit prescribed by MARPOL (discussed in section 2.3.1), or in restricted areas. An oil spill that violates MARPOL limits due to intentional, reckless or negligent actions are absolute

and strict liability offences. Ships can illegally dump oily waste in two ways [11]. They can use the Oily Water Separator (OWS) or using a bypass pipe (called the "magic pipe") to directly dump waste directly overboard. Oil spill violations also indicate other illegal implications such as falsified records or withholding of information in ship records (e.g., Oil Record Book). Illegal discharges occur because of two reasons. First reason is that vessel operatives find a financial advantage in dumping bilge prior arriving at a port. Second reason for oil spill is that, there is a low chance of being discovered and thus can avoid prosecution. To save costs, operators neglect the proper training and maintenance of equipment such as pipes, pumps and OWS, making the pollution prevention system ineffective. Other costs associated with illegal discharges include the direct cost of using port reception facilities (PRF) and the potential indirect cost if the ship must stay for a length of time in port to use PRF [11].

Illegal ship operations accumulate from smaller but recurrent oil discharges which results in a higher volume of oil into the ocean. The amount of oil generated and stored on a vessel depends on the type, age and size of the vessel. The amount and components produced from bilge waste water differ significantly from vessels to vessel. Five general discharges are as follows [11, 36]:

Oily bilge water: as defined in MARPOL Annex I, is water polluted by oily products entering the bilge wells and bilge pipes.

Oil residue (sludge): as defined in MARPOL Annex I, is residual waste from oil products generated during the normal operation of a ship. These include residual waste from fuel purification, lubricating oil, oil filtering machinery and waste oil collected in drip trays.

Cargo residue waste: is waste emanating from tanker vessels that carry different types of cargo, ranging from petroleum products to chemicals and food products.

Crude oil cargo residue waste: is the unpumpable quantities of cargo residue that remains after a complete crude oil discharge operation from a tanker. The amount of crude oil cargo residue depend on size and nature of the cargo tankers.

Oily waste tanks: is waste collected by oil tanks in large vessels. That is, all ships over 400 gross tonnage (gt) are required to have containers for collecting oily residues.

The type of vessel is an essential component in the investigation to identify the kind of substance discharges.

Figure 2.3. Burning BURMAH AGATE tanker incident, Texas, November 1979. (Taken from [5], with permission).

2.2 OIL IN THE OCEAN

The oil spill processes are determined by the type of oil and the environmental conditions at the time of the oil spill. Oil is made up of many components with various properties that affect their behaviour and environmental effect. Oil spill models depend on the successful prediction of oil spill behaviour on the ocean surface. Also, maritime oil pollution responders need to know the current status and ultimate fate of the oil to take measures to minimise the overall impact of the spill. A detailed discussion of oil spill components, behaviour and fate is presented in the next section.

2.2.1 Oil slick properties

The properties of oil discussed here are viscosity, density and flash point. Viscosity measures the resistance of an oil spill to flow in water, where lighter oil spills have lower viscosity and thus flow rapidly at sea. The viscosity is also affected by temperature such that oils that flow readily at high

temperatures can become a slow-moving, viscous mass at low temperatures. Density (volume of oil) is also significant as it indicates whether a particular oil will float or sink in water. Most oils float because they have a lower density than water. However, after a long time, oil spill density increases due to evaporation on lighter oil components. The flash point is the lowest temperature at which vapours of the oil spill will ignite when exposed to an open flame, see Fig. 2.3. There is a broad spectrum of flash-points for petroleum products, many of which are considered ignitable, mainly when newly produced. Crude oils may be ignitable for up to 24 hours till the most of the volatile components have evaporated [12].

2.2.2 Oil slick behaviour

Oil slick behaviour refers to the specific oil spill processes that occur after an oil spill and determines the fate and effects of a particular spill on the environment. Oil released into the ocean surface is affected by two essential transformation processes. The first process is due to weathering and a second transformation is due to a group of processes (including spreading, movement of oil slicks and sinking and over washing) related to the flow of the oil spill. The "weathering" term combines a wide variety of physical, chemical and biological processes that spilt oil undergoes in the environment. These events mainly modify the spreading of the slick and its persistence, see illustration in Fig. 2.4.

The weathering process includes evaporation, emulsification, natural dispersion, dissolution, microbial degradation, photo-oxidation and other processes such as sedimentation and oil suspended particle interactions [37]. There is overlap in the weathering and spreading processes, with weathering changing the oil movements in the sea and the spreading can affect the weathering process. Spreading is where an oil slick physically expands to maximise its surface area. Wind speed, slick surface tension and slick thickness are the primary indicators of how rapidly and to what extent oil will spread on water. However, surface tension alone does not account for spreading behaviour. Also affecting the asymmetry is the wind stress change as the wind passes from oil-free waters to the oil slick. A difference in wind direction often leads the asymmetric or irregular shaped oil slicks.

After an oil spill, among the potential chemical, physical and biological weathering processes, evaporation is usually the dominant weathering process. The evaporation effect is particularly significant on

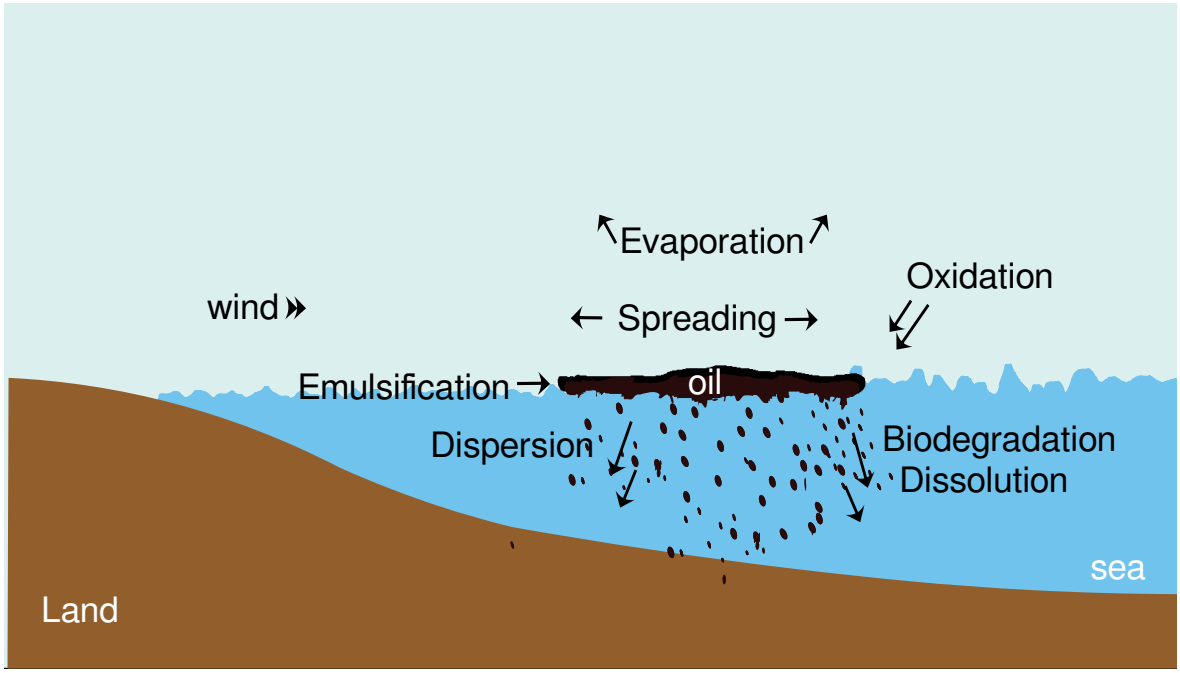

Figure 2.4. Oil spill weathering process.

the oil remaining on land or water after a spill. For example, if oil evaporates rapidly, cleanup is less intense, but the hydrocarbons in the oil enter the atmosphere and cause air pollution.

Oil slicks dampen capillary and short gravity waves, lessening surface roughness. The dampening effect decreases wind-ocean momentum transfer, forming thick oil spills. An oil spill, before it weathers out, may persist on the sea surface for a while. In general, light refined products (e.g., gasoline, diesel) and light crude oils do not persist on the surface of the sea for any considerable length of time due to rapid evaporation of the volatile components and they are more likely to disperse and dissipate naturally, especially in rough seas. Such oils tend to be more toxic and a significant threat to marine plants and animals if sufficient concentrations of oil enter the water column through wave action and are not rapidly diluted by natural sea movements. In contrast, heavy crude oil and heavy fuel oils, while lower in toxicity, are considerably more persistent in the marine environment due to the lesser volatile compound content. Hence, they do not readily evaporate, disperse or dissipate naturally and rough sea conditions are more likely to accelerate the emulsification process.

Figure 2.5. Image showing the impact of an oil spill on the ecosystem, tourism and environment. Taken from [5], with permission.

2.2.3 Oil spill impact

Oil spill events are one of the major marine ecological disasters that often result in a detrimental outcome to the ocean ecosystem and human beings [30, 38, 39]. Oil pollution can enter the marine organisms' food chain, impacting health and population dynamics, see illustrations in Fig. 2.5. It can also have a severe economic impact due to drastic reduction of tourism, closure of fisheries and clean-up costs [40]. The impact of oil spills on the ocean environment depends heavily upon the type, viscosity, toxicity, amount, the length of exposure and the sensitivity of the local organisms. It also depends on location, season, ocean depth, meteorological and oceanic conditions. Wind, waves and surface currents can scatter a large oil spill over a wide area within a few hours in the open sea [12]. Oil spill events can present a long term impact to the marine environment. Even after the oil spill has disappeared or been cleaned up, the recovery of the ecosystem can take upto five years [41].

Figure 2.6. Image showing a seabird covered in oil. Taken from [29], with permission.

The animals and plants that come into contact with the contaminated sea surface are most susceptible to oil spills. Examples include marine mammals, reptiles and some bird species and plants/animals in aquatic agriculture facilities [42], as shown in Fig. 2.6 and Fig. 2.7. A high seabirds' mortality rate correlates with busy shipping routes [43, 44]. Between 1998 and 2008, approximately 350,000 to 390,000 seabirds were killed annually off the Grand Banks (Canada) as a result of illegal discharges of oil from ships [45]. In Alaska about 250,000 seabirds were killed after the Exxon Valdez 41 000 m^3, oil spill on March 24, 1989 [46]. All marine mammals are susceptible to oil pollution when they ingest contaminated food. In the event of a massive oil spill, most fish will swim away, however, if the oil coats their gills, they can die from asphyxiation. When dolphins surface to breathe, oil can restrict their blowholes and airways. After the Deepwater Horizon oil spill, studies found that Barataria Bay dolphins were more likely to have moderate to severe lung disease, commonly described by significant alveolar interstitial syndrome, lung masses and pulmonary consolidation [47].

Figure 2.7. Image showing a turtle covered in oil. Taken from [5], with permission.

2.3 OIL SPILL RESPONSE

An early warning of oil spill accidents and illegal discharges is crucial for coastal environmental protection and reduction of economic losses [17, 48, 1], see Fig. 2.8. Four key actions need to be undertaken to prevent and limit oil spill damages: prevention, monitoring, warning and damage quantification. To minimise a potential oil spill all political and technical measures to be taken at an international level well in advance of the polluting event. Prevention includes periodic certification of oil tankers. Monitoring action is related to all efforts to continuously and efficiently observe illegal discharges and accidents. A combination of an automatic system based on remote sensing images and expert input is ideal. Once the oil is detected, a warning action with risk assessment is launched to establish response actions on the field. The monitoring action is continued to observe oil spill evolution and dynamics with emphasis to the source of the warning. Damage quantification is an after-event action which aims to predict future oil spills and supports protection action.

Figure 2.8. Cleaning up of oil spill on Korean beaches following the HEBEI SPIRIT oil spill in 2007. (Taken from [5], with permission).

2.3.1 Oil spill prevention laws

Strict international rules (Annexes) have been agreed to in order to prevent illegal oil spills in marine environments. The International Convention for the Prevention of Pollution from Ships (MARPOL 73/78 Annex I), adopted at the International Maritime Organisation (IMO) in 1973 and modified by the Protocol of 1978, defined international regulations that specifically deal with prevention of oil pollution by ships in a maritime environment. MARPOL Annex I regulations state that "any discharge into the sea of oil or oily mixtures from ships shall be prohibited" [49, 11, 50].

The international legislation contains explicit laws related to ocean areas (internal waters, marine protected areas, MARPOL special areas, territorial seas or exclusive economic zones) [11]. These areas often determine whether an action is considered legal or not and define the rights and obligations,

including law enforcement obligations. For example, all oil discharges from ships are entirely prohibited in particular areas unless the oil spill is not visible on or below the surface of the water [11]. A discharge outside these areas is possible if certain conditions are satisfied, for example, the oil content does not originate from bilge waste. Ships must report any oil spill incidents above authorised levels. However, the expected risk of fines is less than the cost of compliance especially when the chance of being caught is small [51]. As a result, some vessels do not report incidents and continue to discharge oil in forbidden areas illegally [6].

Proving a MARPOL infringement requires gathering evidence to delineate the spill with regards to the type of oil, the concentration of oil, the distance from shore and speed of the vessel [11, 36]. Further information such as the size of the spill and its impact on the natural ecosystem may be used to determine the level of punishment. The enforcement process involves, but is not limited to, operational authorities, vessel inspection authorities and administrative and judicial enforcement authorities. Operational authorities are responsible for monitoring the marine environment. The illegal discharge enforcement chain involves two steps: Step 1 is to check initial indications of a possible violation using three primary sources of information, including detection at sea, inspection in port and information received. Step 2 is further investigation and collecting evidence to be used for four primary purposes, including characterising the spill, determining the source of the spill, proving intent (recklessness or negligence) and gathering information that could later support the case. The collection, sharing and organising of evidence is critical from all authorities involved even before a formal request for judicial assistance has been made. The evidence is collected with care to ensure that it is acceptable in the courts of the State building the case. For evidence to be collected promptly, coastal stations need to have proper authorisation to take critical decisions such as dispatching a ship to investigate the site. They should be well informed of the enforcement chain to guide them about when to involve administrative or judicial authorities to start an investigation formally [11].

2.3.2 Oil spill monitoring

Although the oil industry is entirely informed of the international laws and the risks related to marine pollution, there is still evidence of numerous and repeated oil spill offences [1]. Oil spill surveillance is thus a critical part of oil spill disaster management. The knowledge of oil slick location, size and dynamics are starting points to plan countermeasures to minimise the effects of pollution [3] effectively.

There are mainly two techniques for oil spill detection:

1. In-Situ: In the in-situ technique, researchers need to travel to the place with sensors and collect the data. Autonomous underwater vehicles (AUV) are used for travelling purposes.
2. Remote Sensing: In remote sensing, the sensors (e.g., optical and microwaves) are mounted on the satellite and capture the Earth's surface (discussed in chapter 3).

Spaceborne and airborne remote sensing are complementary monitoring instruments that should be used in combination to achieve maximum coverage. Spaceborne remote sensing can cover much broader areas at a lower cost but also at a lower resolution. Airborne remote sensing has a smaller coverage but can be immediately dispatched to start further on-site investigations. Satellite surveillance is thus useful for monitoring a large area and providing an initial indication of a spill. Aerial surveillance can then be used to collect evidence which can help to prosecute the offenders successfully [11].

2.4 SUMMARY

According to the United Nations Convention on the Law of the Sea, oil spills (biogenic and mineral oils) are a form of marine pollution. Ship accidents and illegal operational discharges are the prominent sources of maritime oil pollution. The law (MARPOL) requires the retrieval of oil from vessels to be performed in the harbours. However, a significant proportion of oil spills are caused by deliberate discharges in the form of bilge and fuel oil from tankers or cargo vessels. Marine oil spills can be highly dangerous and may result in the destruction of the ecology of the coastal and marine ecosystems and the species that inhabit them. Thus, a rapid response to all oil spills are required to minimise the environmental impact.

Oil spills in the marine environment weather out quickly, thus a timely collection of evidence is critical. All response operators need to work together, from identifying the oil spill to collecting the evidence, for a successful prosecution. Remote sensing surveillance through satellite and aircraft instruments should be readily available to check the possible pollution sites with the shortest possible time delay. Consequently, satellite acquisition preparation and flight plans should be organised to optimise both the use of satellite and aerial monitoring. A successful operational surveillance system depends on a rapid and reliable warning capability. Using remote sensing (RS) and AIS data (ships positioning system),

the oil spill and ship responsible for pollution at sea can be identified [52, 53]. The RS data from the satellite is a useful tool in combination with standard observation techniques to ensure successful oil spill monitoring. The use of satellite RS data has significant advantages such as broad area (global) coverage and costs less compared to aircraft monitoring. The next chapter discusses using remote sensing tools for oil spill detection and discusses their advantages and limitations.

CHAPTER 3 OIL SPILL REMOTE SENSING

3.1 RS OVERVIEW

Imaging in remote sensing (RS) can be conducted from both satellite and aircraft platforms. In many ways, the sensors have similar characteristics, but the platform differences in altitude and stability can lead to very different image properties. The use of RS data in combination with standard observation is essential to ensure a successful oil spill surveillance system. RS provides a timely means to map out the locations and approximate concentrations of oil spill events in many conditions. Also, RS can determine the oil spill's properties, its degree of weathering, its source and its potential impact on the environment. However, the cost of sending a surveillance aircraft to check a possible oil spill location is high. Thus automatic detection should be followed with operator inspection of the reported possible oil spill locations before sending a surveillance aircraft.

RS measurements are made using either passive or active sensors mounted on an aircraft or spacecraft platform. Passive RS measures the sun's energy emanating from the earth's surface, while active RS measures the return energy radiated from a platform onto the earth's surface. Active sensors provide their energy and can operate during day or night. The measurements are used to construct an image of the landscape beneath the platform. The energy is transmitted from the sensor/sun to the Earth's surface where it is scattered or emitted back to the sensor and then processed into image products ready for application by the user, see illustration in Fig. 3.1. RS image properties are described by the sensor's spectral bands, spatial resolution, radiometric resolution, temporal resolution and swath. Spectral bands provide the number and location of the spectral measurements given by a particular sensor. Spatial resolution describes the amount of ground detail presented by pixel size, where the higher the spatial resolution, the smaller the details that can be recognised in the images. The radiometric resolution represents the range and a discernible number of discrete brightness values in the image. The temporal

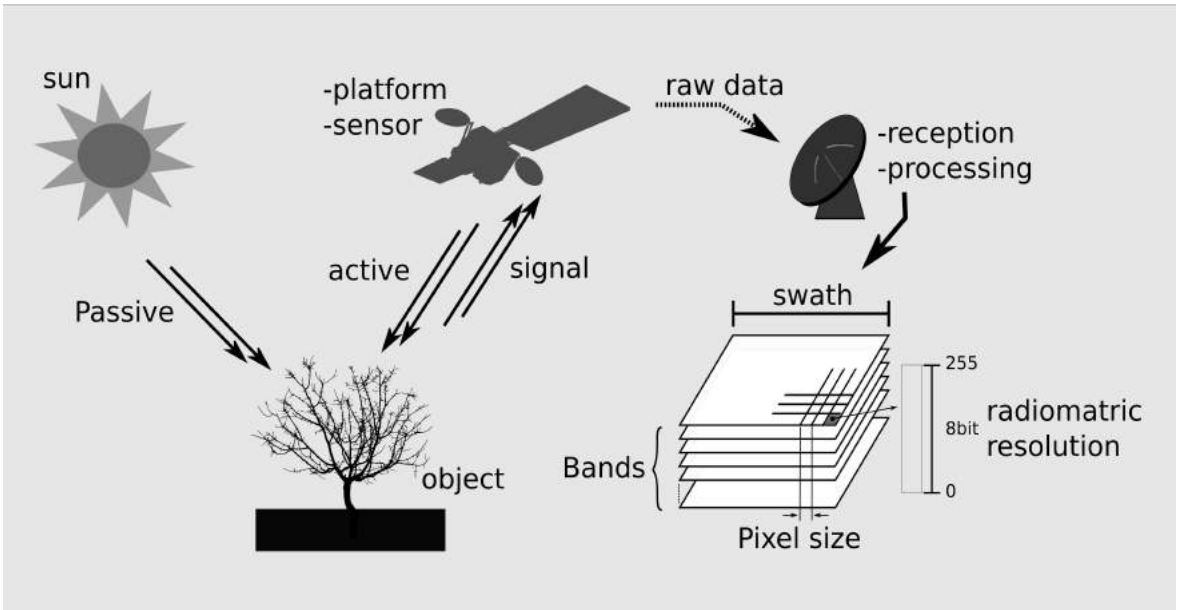

Figure 3.1. Schematic depicting remote sensing processes including digital image description, i.e., bands, resolution and swath.

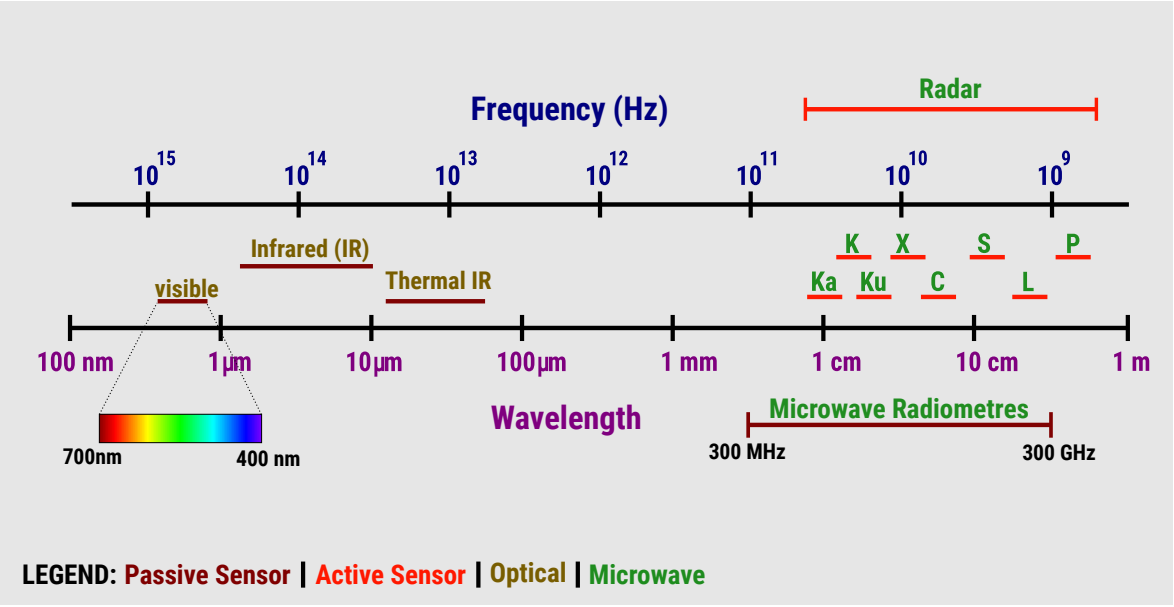

Figure 3.2. Types of Active and Passive Remote Sensing Sensors Electromagnetic energy range chart.

resolution represents the sensor imaging frequency of the same scene. Finally, swath describes the frame size of an image in equivalent ground kilometres. All the properties together determine the application and data volume generated by a particular sensor.

Table 3.1. Subregions of the spectrum for the optical wavelengths and microwave frequencies [54].

Optical Wavelengths		**Microwave Frequencies**	
Name	Wavelength	Band	Frequency
Ultraviolet (UV)	10 – 400 nm	Ka	25 – 40 GHz
Ultraviolet-B (UV-B)	280 – 320 nm	Ku	12 – 18 GHz
Visible (V)	400 – 700 nm	X	8 – 12 GHz
Near infrared (NIR)	0.7 – 3.5 µm	C	4 – 8 GHz
Visible/near infrared (VNIR)	0.4 – 3.5 µm	S	2 – 4 GHz
Thermal infrared (TIR)	3.5 – 20 µm	L	1 – 2 GHz
Visible/infrared (VIR)	0.4 – 20 µm	P	0.3 – 1 GHz

RS sensors measure electromagnetic energy in the optical, thermal and microwave regions. Possibly the most notable aspect of the image data in a remote sensing system is the spectrum of wavelengths used in the image acquisition sensors [54]. In principle, RS systems can measure energy emanating from the earth's surface in any reasonable range of wavelengths, see sensor frequency and wavelength chart in Fig. 3.2. Wavelength λ (in metres) is related to the frequency f (in Hz) by

$$\lambda = \frac{c}{f} \tag{3.1}$$

where c is the speed of light in vacuum. The significance of the different wavelength ranges lies in the interaction mechanism between the electromagnetic radiation and the examined materials. The relevant ranges utilised for oil spill RS are between about 0.4 and 12 µm (the visible/infrared range) and between about 30 to 300 mm (the microwave range), see Table 3.1. Frequency is commonly used to describe microwave wavelength ranges, that is, 1 GHz and 10 GHz is used to for microwave range of 30 to 300 mm. Radar frequencies were described with letters (frequency bands) for purposes of secrecy during the World War II [55] and were set as the universal standard after that, as shown in Table 3.1.

Each region of wavelength has its benefits concerning the data it can provide to the remote sensing method. Depending on the wavelength or frequency range utilised by the sensor, different features can be mapped [54]. Sensors at the visible and infrared regions of the EM spectrum can estimate:

- soil moister and mineral content,
- level of sedimentation of water,
- vegetation pigmentation, moisture content and cellular structure.

Sensors at the thermal infrared region of the EM spectrum can measure radiation emitted from target to estimate thermal characteristics for [56]:

- vegetation in agriculture and forestry,
- soil moister studies,
- forest fires.

Sensors at the microwave region of the EM spectrum use active imaging based on radar systems to measure surface the roughness to estimate [57]:

- vegetation type,
- oil spill detection,
- soil moister content.

Radar systems can further use the magnitude of the returned signal to map highly reflective targets such as vessels.

3.2 OIL SPILL RS EFFORTS

It is necessary to set up broad area surveillance systems capable of monitoring oil spill at regular intervals, especially at night, in ice or among seaweeds. Specialised instruments are sometimes required to detect oil spills. Remote sensing (RS) of oil involves the use of sensors other than human vision to detect or map oil spills. The oil slick is detected and tracked using instruments on-board aircraft or satellites platforms. This section provides a review of monitoring systems using various remote sensing

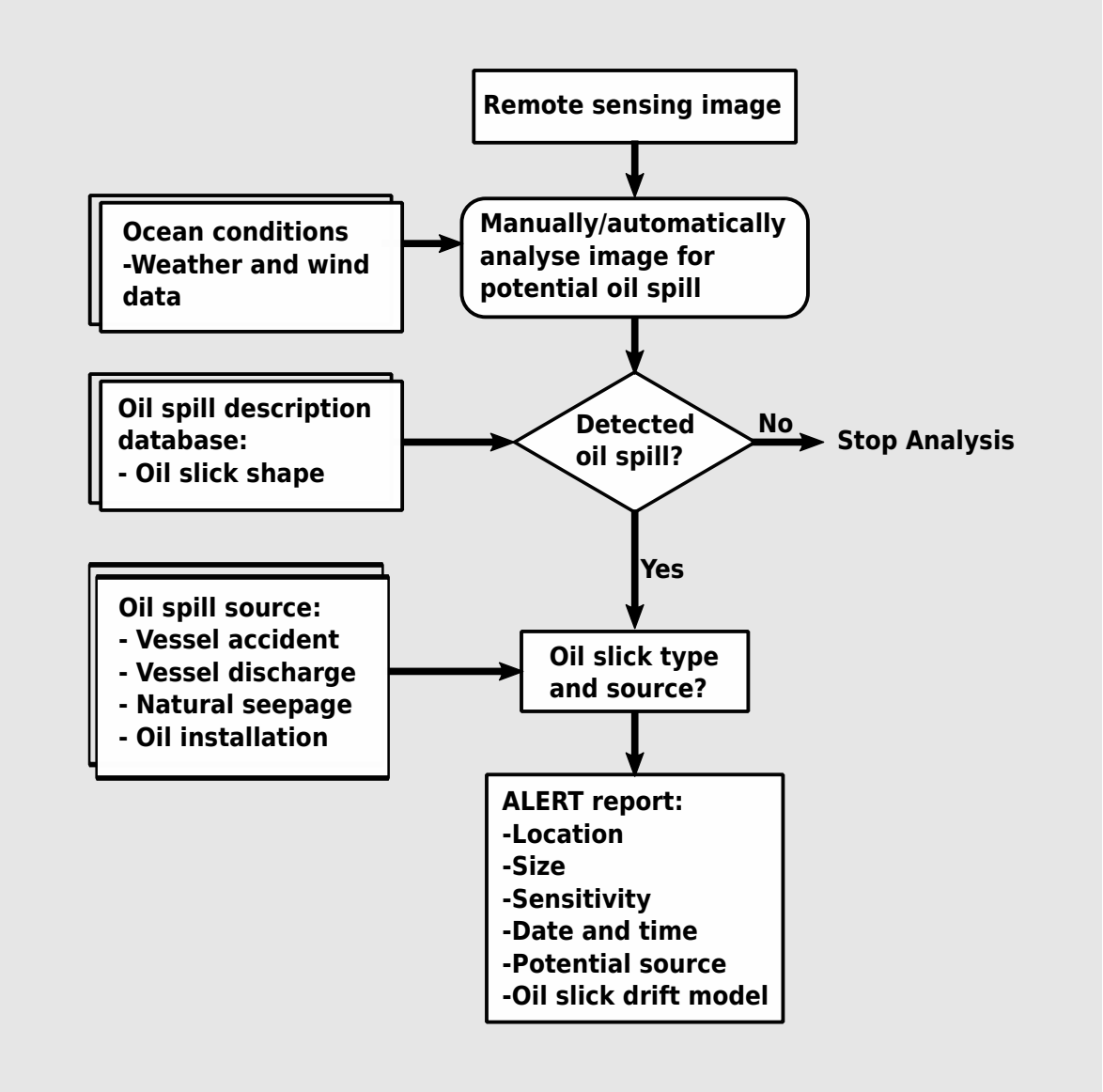

Figure 3.3. Flow diagram for oil spill detection using remote sensing images.

tools, including their strengths and weaknesses for oil spill monitoring. The study did not go into detail on remote sensing technical description of the sensors but focused on their oil spill monitoring capabilities. A general hierarchy for oil spill detection techniques using remote sensing is presented in Fig. 3.3.

3.2.1 Optical sensors

Optical techniques are the most common means of remote sensing. Most optical RS systems acquire data using sensors from visible through the mid-infrared range of the EM spectrum [54]. Different wavelengths emitted by the Earth's surface can be resolved to help understand the properties of the imaged earth surface region. Optical sensors are, however, affected by cloud cover, aerosols and fog. Optical sensor wavelength bands are within and adjacent to the visible/infrared (VIR), see Table 3.1. The ultraviolet (UV) band occurs at shorter wavelengths than the visible. The near-infrared (NIR) band occurs at longer wavelengths than the visible and like the visible is dominated by reflected solar radiation. The thermal-infrared (TIR) band includes those wavelengths dominated by thermal emission from the Earth's surface.

3.2.1.1 Visible

In the visible region of the electromagnetic spectrum (approximately 400 – 700 nm), oil has a higher surface reflectance than water but also shows limited nonspecific absorption tendencies. Thin oil slick (also denoted as *sheen*) shows up silvery and reflects light over a broad spectral region down to the blue giving it a rainbow like appearance, see example in Fig. 3.4. As there is no substantial information in the 500 – 600 nm region, this region is often filtered out to improve contrast. Overall, however, oil has no specific characteristics that distinguish it from the background. Therefore, methods that separate particular EM spectral regions do not improve detection ability. Visible RS methods are not ideal for oil spill detection as there are many obstructions and false alarms. Obstruction such caused by clouds can limit the visibility of the oil spill. Sunglint, wind sheens and biogenic material (such as surface seaweeds or sunken kelp beds) can be mistaken for oil and generate false alerts. Further, it is challenging to detect oil spill on shorelines due to seaweeds false alarms and dark shores. Visible RS is thus mainly used to document already identified discharges.

In summary, visible sensors are subject to the same restraints as visual surveillance since their usefulness for oil detection is limited. Nevertheless, visible RS is an effective way to document oil spills and provide baseline data on shorelines or relative locations.

Figure 3.4. Sheen in waters near Cebu City, Philippines. The thinnest oil Sheen (0.05 – 0.2 µm thickness) appear silvery; followed by a iridescent (or rainbow) oil sheen (0.3 – 3 µm); and thicker oil sheen (>3 µm) have a metallic or brown to black appearance. (Taken from [5], with permission).

3.2.1.2 Infrared

Thick oil slick absorbs infrared (IR) radiation from the sun and re-emits a portion of this radiation as thermal energy, primarily in the 8 µm to 14 µm region. In IR images, thick oil appears hot on a cold ocean surface. Intermediate thicknesses of oil appear cool and thin slicks are not detected. IR imagery may detect oil spill at night when it looks 'colder' than the surrounding sea. At a certain thickness evaporative cooling of the slick exceeds its radiative heating causing the slick to appear cold compared to the surrounding water [58]. Moderately thin oil slick can also reduce the of thermal radiation emitted by the water and cause the slick to appear colder compared the surrounding water. The oil slick thickness transitions are not fully understood. Studies suggest that the minimum detectable thickness is between 10 µm and 70 µm and the shifts are within the hot and cold layer extends within 50 µm and

150 µm and [17].

A high spatial resolution IR system and low water-in-oil emulsions are essential for a successful IR oil spill detection [58]. The relevant thickness data in the thermal IR can be used to guide response operators where to place cleaning equipment at the thicker parts of the slick.

In summary, the advantage of infrared RS over visible RS s that they provide information regarding relative thickness since only thicker slicks can be detected. However, IR is not perfect as several false targets, such as seaweeds, oceanic front and shoreline, can interfere

3.2.1.3 Ultraviolet

Oil slicks exhibit a high reflectivity of Ultraviolet (UV) radiation. UV sensors can be utilised to detect oil sheens, including thin layers (<0.01 µm). A combination of UV and IR sensors are usually employed together to identify oil spills and provide their corresponding thickness information [59, 58]. Similar to visible sensors, UV systems are also subject to several obstructions and false alarms (wind slicks, sun glints and biogenic material). Using UV together with IR can improve interferences and false alarms and provide a more accurate indication of oil than using either technique alone. Since these interferences are often different than those for IR sensing, combining IR and UV can provide better detection accuracy of oil spills than using each system separately. However, overlaying UV data with IR is often complicated and thus are not commonly used together.

3.2.2 Laser fluorosensors

Laser fluorosensors use a laser in the ultraviolet spectrum to trigger the fluorescing phenomenon and can detect oil spill from the visible light. Aromatic compounds in oils absorb ultraviolet light and become electronically excited. The process of fluorescence emission quickly removes the excitation, primarily in the visible region of the spectrum. Because very few other compounds show this tendency, fluorescence is a strong indication of the presence of oil. Natural fluorescing materials, such as chlorophyll, fluoresce at sufficiently different wavelengths than oil. Various classes of oil yield slightly different fluorescent intensities and spectral signatures. It is thus possible, under ideal conditions,

to discriminate between types of oil [12]. Further, data in the visible light return can be utilised to determine the oil spill type and thickness.

In summary, laser fluorosensors have significant potential as they are subject to very few interferences and can discriminate oil from look-alikes not only on the sea but also in ice and snow. Disadvantages of laser fluorosensors include the high cost of these sensors and their large size and weight [12].

3.2.3 Microwave sensors

3.2.3.1 Radiometers

Oil spills emit greater microwave radiation than the surrounding water and thus appear as bright targets on a darker ocean surface [7]. A microwave radiometer is a passive sensor that can detect oil spills by distinguishing the difference in emissivity between water (emissivity factor $= 0.4$) and oil slick (emissivity factor $= 0.8$). The sensor signal return is influenced by the amount of oil and can be employed to estimate the slick thickness. Microwave radiometers methods that use multiple polarizations to measure oil slick thickness have been proposed [60]. However, the dependence on the oil slick thickness also means certain oil thickness cannot be detected. Other challenges of using the microwave radiation sensor include the difficulty in obtaining high spatial resolution, the low signal-to-noise ratio and the interference from biogenic materials [58].

In summary, passive microwave radiometers may have potential as all-weather oil sensors. Hower, the number of environmental and oil specific parameters that are required to detect oil spills successfully makes the sensor less reliable.

3.2.3.2 Radar

RADAR is an acronym for Radio Detection and Ranging. It transmits an electromagnetic signal to a target and measures its distance using the time delay from the return signal reflected from the target. Radars provide their own signal (active remote-sensing) to detect the presence of objects. This allows them to operate during day or night and they can penetrate clouds and rain. Therefore radar images can be acquired not only during the day or night but also under (almost) all weather conditions. Imaging,

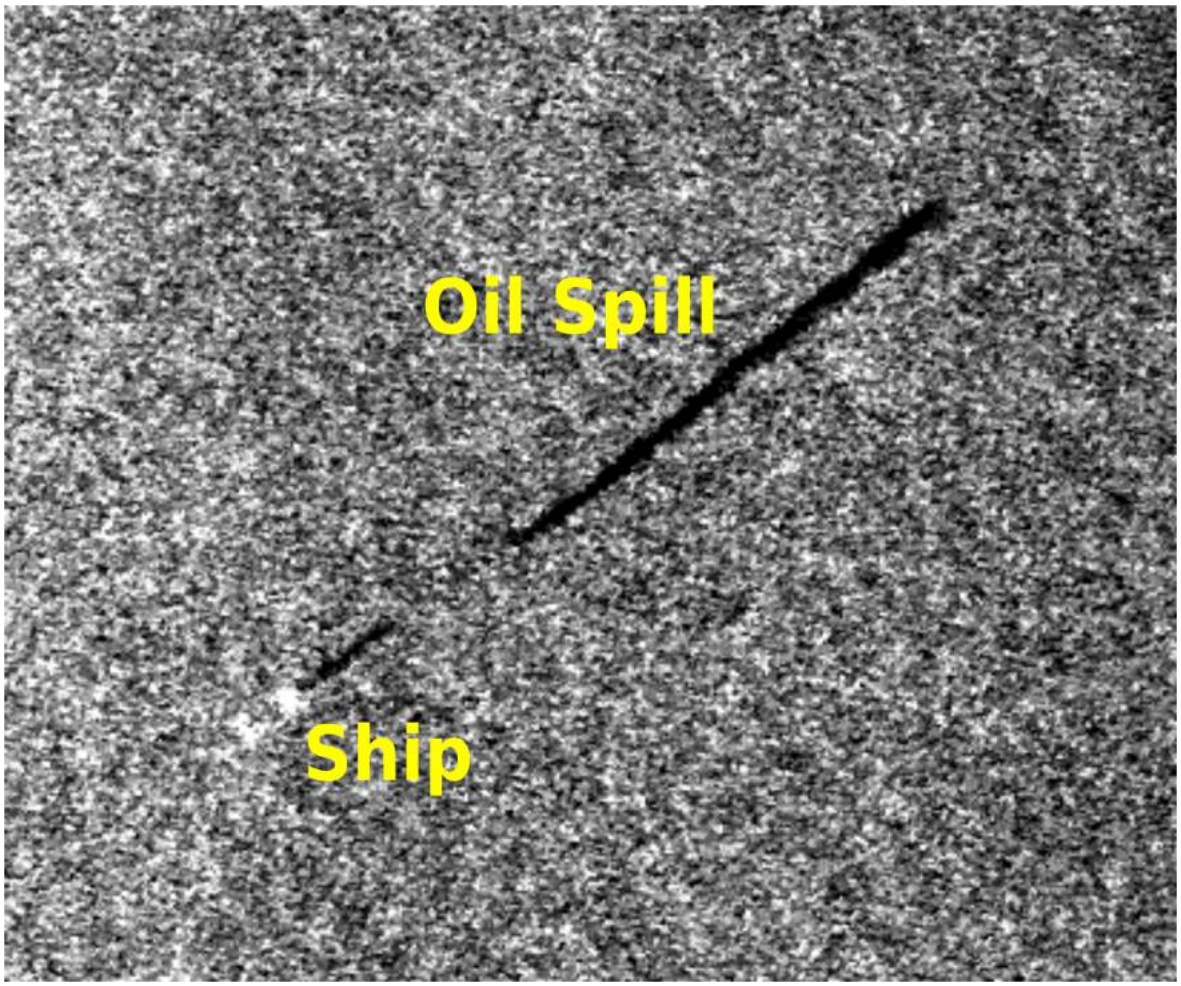

Figure 3.5. SAR image with an oil spill (dark region) and ship (bright spot).

remote sensing radars, such as SAR, produce high-resolution images of surfaces [18, 19, 20, 21, 61]. Synthetic Aperture Radar (SAR) and Side-Looking Airborne Radar (SLAR) are the two fundamental types of radar that can be used to detect oil spills and for environmental RS applications. SLAR is an older, but less expensive technology, which uses a long antenna to achieve spatial resolution. SAR is a system which applies signal processing to increase the resolution exceeding the constraint of the physical antenna aperture [62, 63, 64].

Capillary waves on the ocean surface reflect radar energy, generating a *bright* image called sea clutter. The presence of an oil spill on the sea surface causes a dampening effect on the capillary waves which then reduces radar energy. The appearance of an oil slick is thus detected as a *dark* region on the sea clutter, see Fig. 3.5. The source of the oil spill (e.g., vessel) can also be detected as *bright spots* from the same SAR image [65, 66]. Unfortunately, there are many false targets, including calm winds, wave

Table 3.2. Strengths and weaknesses of different remote sensing tools used for oil spill surveillance, adapted from [12].

RS Sensor	Cleanup Support	Night Operation	Fog/Cloud Visibilty	Shoreline Survey	Spill Mapping	Discharge Surveillance	Coverage Width
Visible	3	1	1	3	2	3	4
Infrared	4	3	2	2	3	4	3
Ultraviolet	3	1	1	2	3	3	3
Laser fluorosensor	5	4	4	5	1	5	2
Radiometers	2	4	4	2	2	3	3
Radar	2	5	5	2	4	4	5

Suitability scale: from poorly = 2 to ideally = 5 suitable, and 1 = not suitable/applicable.

shadows behind land or structures, seaweed beds that calm the water just above them and biogenic oils. As a result, radar can be ineffective in locations where there are a lot of islands, fresh water inflows, ice and other features which produce hundreds of such false targets.

In summary, SAR is intrinsically the only viable and practical imaging radar technique to achieve high spatial resolution, also from space platforms. Radar optimised for oil spills is useful in oil spill remote sensing, particularly for searches of large areas (on satellite platform), during the day or night and under most weather conditions. However, the technique is highly prone to false targets and is limited to a narrow range of wind speeds.

3.3 SUMMARY

No single sensor was able to provide all the information required for oil spill contingency planning. Hence, a combination of sensors is recommended, if available, for oil spill surveillance. However, the user may not have multiple RS tools. This section examined the characteristics and applications of different RS sensors to better understand the strengths and weaknesses of each for oil spill surveillance. Several RS tools can be used to detect oil spill. However, the advantages of each sensor significantly

differ, see Table 3.2. From the table we can see that the laser flourosensor is the most useful sensor for detecting the type and thickness of oil spill. The SAR based microwave sensor is the most practical sensor, however, as it can cover a much larger area at a lower cost when compared to laser flourosensors. SAR can thus be used as an early detection sensor and a laser flourosensor (if available) can be used to verify the oil spill.

The main aim of the study is to detect and monitor oil spills over a large area, day and night, under most weather conditions. SAR has proven to be the most appropriate sensor and provides easy accessible (freely available) data for this study. Also, SAR is the most used remote sensing (RS) tool for monitoring oil pollution in literature [18, 19, 20, 21, 15, 16, 17]. The next chapter discusses using synthetic aperture radar (SAR) oil spill imaging processes, including SAR missions, variants, interaction with the ocean, interaction with the oil spill and SAR limitation.

CHAPTER 4 OIL SPILL IMAGING USING SAR

4.1 SAR SYSTEMS OVERVIEW

SAR is a system which employs signal processing to increase the resolution beyond the restriction of physical antenna aperture. It uses an active microwave EM sensor to image Earth in both day and night and for almost all weather conditions. In SAR, a forward motion of actual antenna is used to "synthesize" a very long antenna [55]. SAR allows the possibility of using longer wavelengths while still achieving good resolution with antenna structures of reasonable size. The potential of SAR in a diverse range of applications led to the development of many airborne and spaceborne SAR systems.

4.1.1 SAR variants

SAR sensors retrieve information of a target from the amplitude and phase characteristics of scattering target [67]. Each SAR system has its own configuration in terms of frequency, polarization, resolution and swath width. The electromagnetic waves generated by radars are generally plane-polarized. For Earth remote sensing, the radars transmit and receive in either the vertical (V) or the horizontal (H) plane. Antennas that both broadcast and receive in either V or H are called co-polarized (VV or HH) or cross-polarized (VH or HV) antennas. The transmitted pulse interacts with the Earth's surface in four possible ways. It can be transmitted through the target, absorbed by it, scattered away from it, or backscattered toward the receiving antenna. The amplitude and phase of the backscattered signal depend on the physical (i.e., geometry, roughness) and electrical properties (i.e., permittivity) of the imaged object.

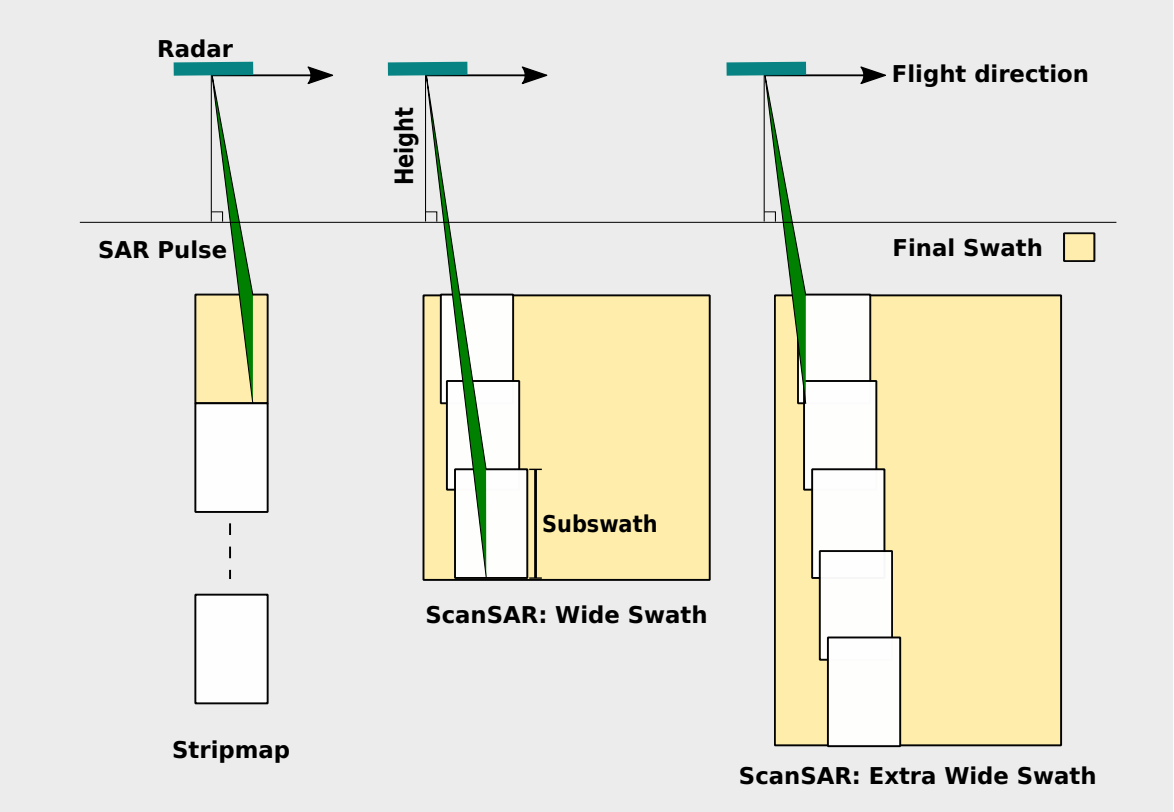

Figure 4.1. An example of SAR modes and their respective to Swath Coverage.

Current SAR systems are capable of operating in different imaging modes by controlling the antenna radiation pattern [68, 69], see illustration in Fig. 4.1. For a planar antenna this is done by dividing the antenna into sub-apertures and controlling the phase and amplitude of each sub-aperture through transmit/receive modules (TRM). Typically a few hundred TRMs are employed, with their settings controlled by software. The most fundamental mode is the Stripmap operation, where the pattern is fixed to one swath, thus imaging a single continuous strip. If a wider swath is required, the system can be operated in the ScanSAR mode. Here the antenna elevation pattern is successively steered to different elevation angles corresponding to multiple sub-swaths. Each sub-swath is illuminated by multiple pulses but for a shorter time than in the Stripmap case. The timing is adjusted such that the time-varying elevation patterns repeat cyclically the imaging of multiple continuous sub-swaths. After appropriate processing this yields a wide-swath SAR image, however, the azimuth resolution is degraded when compared to the Stripmap mode. The ScanSAR mode has a swath width of 350 km – 500 km and a resolution of 75 m – 150 m.

Spotlight mode is used to achieve a better resolution in the azimuth direction. In Spotlight mode, the

antenna pattern is steered in azimuth towards a fixed point to illuminate a given region. A prolonged illumination time over the area is used to improve the synthetic aperture length, therefore achieving a higher resolution. However, the Spotlight mode is limited to imaging patches, that is, it cannot continually image large regions along the radar flight path. More imaging modes have been proposed to improve SAR imaging, for example, TOPS or the wave modes. However, the attained improvements are the expense of other features [70].

4.1.2 SAR missions

Imaging radar has proved itself as an essential and competent Earth remote sensing instrument since 1978 with the successful launch of SeaSat satellite. SeaSat was the first nonmilitary Earth-orbiting satellite carrying a SAR wide swath remote sensing sensor intended for oceans and sea ice applications. The SeaSat mission, however, also showed SAR capability for land applications such as terrain discrimination and target detection. The SeaSat SAR operated at L-band with a single HH polarization channel [71]. SeaSat SAR only imaged Earth for only 105 days due to a massive electric system failure, but the data was enough to encourage further advancements in SAR development. Within the short lifespan, SeaSat observed the ocean surface and internal waves by revealing additional features such as current boundaries, eddies and a number of atmospheric patterns. After SeaSat, several satellites carrying SAR systems have been launched by different countries. The Shuttle Imaging Radar missions SIR-A and SIR-B were launched in 1981 and 1984, respectively. The satellites were extensively used for the validation of wave imaging models developed from SeaSat data [72]. The European Space Agency (ESA) then launched the ERS-1 and ERS-2 satellites in 1991 and 1995, respectively. In 1994, the first multifrequency and multi-polarized spaceborne data launched through the SIR-C/X-SAR mission . In 1995, the first mission with multiple beam modes, varying resolutions and look angles was launched by the Canadian Space Agency (CSA) through the Radarsat-1 mission. In 2002, the first satellite to acquire dual polarized beam mode on a regular basis was launched from ESA's Envisat mission. A fully polarimetric mode satellite was realised in 2006 with the launch of the ALOS satellite by JAXA in 2006. The German Aerospace Center (DLR) launched the first X-band sensor on a satellite in space through the TerraSAR-X mission in 2007. There are many other countries that also contributed to further milestones in spaceborne SAR development (e.g., Italy and Korea). An overview of spaceborne SAR missions is presented in Table 4.1. Numerous oceanographic applications were developed using SAR satellites [73, 74, 75, 44, 76]. However, not all SAR satellite missions focus on

marine observation, some satellites (such as TerraSAR-X, TanDEM-X and COSMO-SKYMED) are mainly used for land applications [77, 78, 79].

SAR system developments (e.g., digital beamforming, MIMO, bistatic and multistatic, large reflector antennas) are focused on achieving increased information content SAR images. The increased information includes [80]:

- multichannel operation (polarimetry and multifrequency),
- improved range and azimuth resolution,
- time series (a frequent revisiting of the same area) and
- observation angle diversity (interferometry and tomography).

The end goal of spaceborne SAR systems is to provide continuous monitoring of Earth's surface using high temporal, high resolution, wide-swath, in a quasi-continuous way.

Table 4.1. An overview of spaceborne SAR sensors.

Satellite	Operation	Operator, Country	Band (Polarisation)	Resolution (m)	Swath (km)
SeaSat	1978	NASA/JPL, USA	L (HH)	25	100
ERS-1	1991 - 2000	ESA, Europe	C (VV)	25	100
JERS-1	1992 - 1998	JAXA, Japan	L (HH)	18	75
SIR-C	1994	NASA/JPL, USA	L & C (quad)	30	15 - 90
ERS-2	1995 - 2011	ESA, Europe	C (VV)	25	100
RADARSAT-1	1995	CSA, Canada	C (HH)	10 - 100	50 - 500
EnviSat	2002 - 2012	ESA, Europe	C (dual)	25 - 1000	100 - 400
ALOS/PalSAR	2006 - 2011	JAXA, Japan	L (quad)	10 - 100	70 - 360
COSMO-Skymed-1/4	2007… 2010 - present	ASI/MiD, Italy	X (dual)	1 - 16	10 - 200
RADARSAT-2	2008 - present	CSA, Canada	C (quad)	3 - 100	10 - 500
TerraSAR-X/Tandem-X	2007/2010 - present	DLR, German	X (quad)	1 - 16	10 - 100
Kompsat-5	2013	KARI, Korea	X (dual)	1 - 20	5 - 10
ALOS-2	2013	JAXA, Japan	L (quad)	3 - 100	25 - 350
Sentinel-1A/1B	2014/2016 - present	ESA	C (dual)	5 - 50	20 - 400

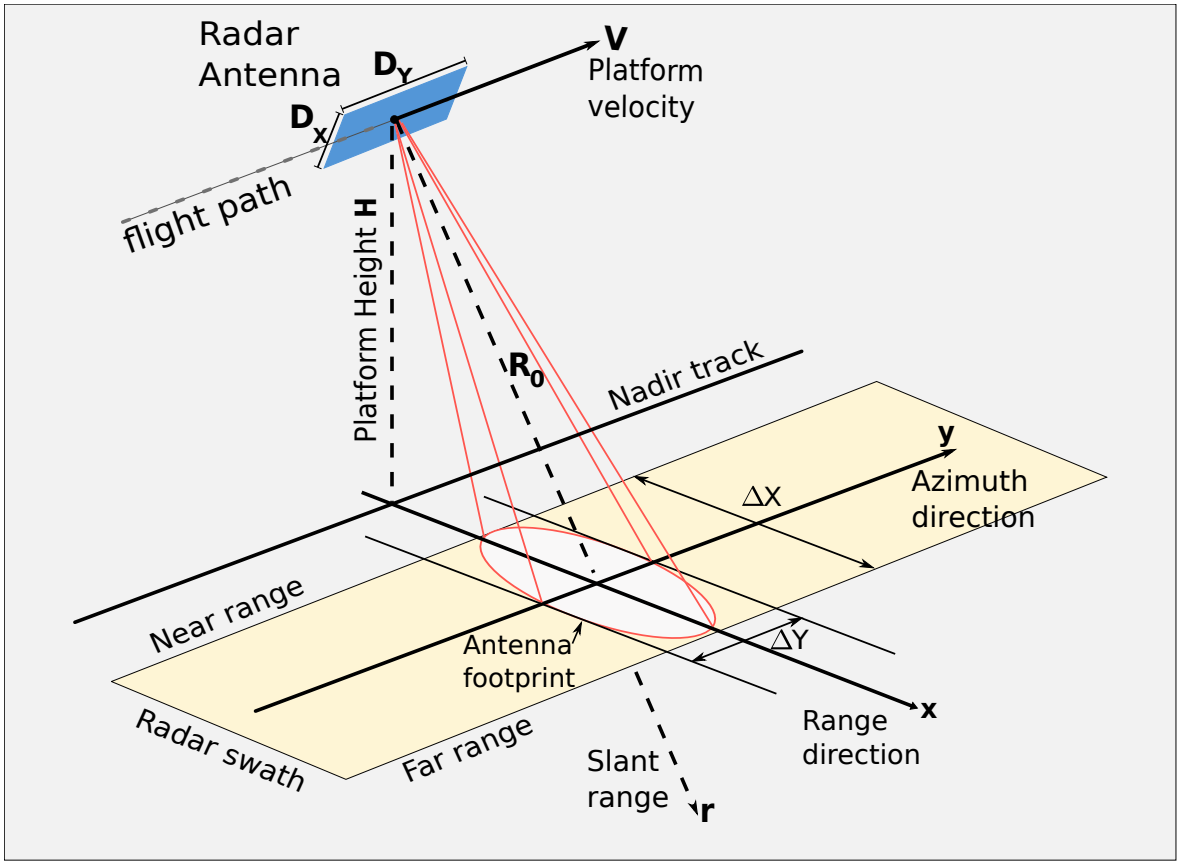

Figure 4.2. SAR imaging geometry and footprint.

4.2 SAR PRINCIPLES

The geometry for a typical radar and its footprint are illustrated in Fig. 4.2. SAR systems have a side-looking imaging geometry and are based on a pulsed radar mounted on a platform moving with velocity V at altitude H. The illuminated ground area is called the radar "antenna footprint". Radar images are typically acquired in strips as the satellite or aircraft carrying the radar system moves along its flight path. The strips, also referred to as "radar swath" or "tracks", varies typically from a few kilometres to 20 km in the airborne case and from 30 to 500 km in the spaceborne case. To separate objects in the cross-track direction (x) and the along-track direction (y) within a radar image, two different methods must be implemented. The along-track, also known as "azimuth direction", is parallel to the movement of the imaging platform direction. The cross-track, also known as "ground range direction", is perpendicular to the along-track direction. The radial axis or range along the line-of-sight is referred to as "slant-range" (r). The slant range is often a more convenient parameter than the ground range because it is directly measured along the line connecting the radar and the object

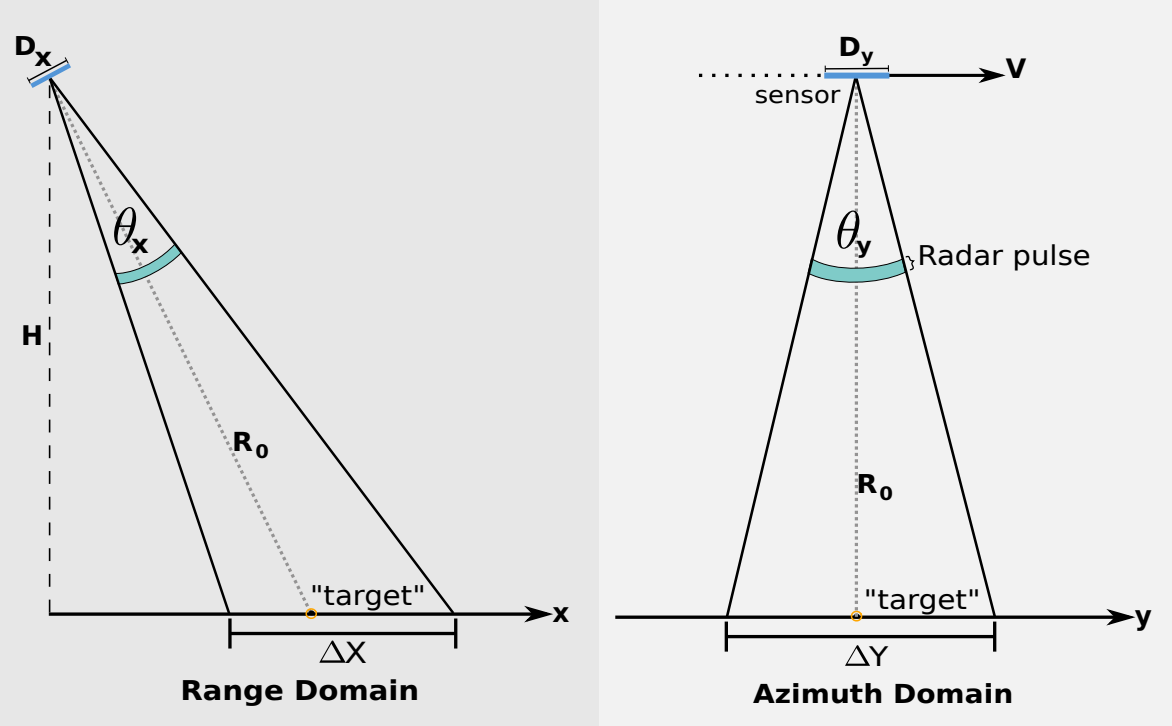

Figure 4.3. Azimuth and Range broadside geometry.

being imaged, often called the target or the scatterer [21], see Fig. 4.3.

A typical radar system consists of the transmitter, switch, antenna, receiver and data recorder. The transmitter generates a high power of electromagnetic wave at radio wavelengths. The antenna transmits the EM pulse or "radar pulse" towards the area to be imaged and collects returned echoes, see Fig. 4.3. The physical antenna ("radar antenna") is rectangular with width and length dimensions ($D_x \times D_y$). These dimensions are significant because they determine the area or "antenna footprint", illuminated by the antenna. The dimension of the antenna footprint ($\Delta X \times \Delta Y$) is defined from the antenna beamwidths (θ_x, θ_y), given by

$$\theta_x \approx \frac{\lambda}{D_x} \quad \text{and} \quad \theta_y \approx \frac{\lambda}{D_y}, \tag{4.1}$$

where λ is the transmitted wavelength corresponding to the carrier frequency ($f_c = c/\lambda$) and c is the speed of light [71, 64]. While the radar beam sweeps over a fixed "target" (also called a scatterer), the distance R between the scatterer and the platform will vary symmetrically about its minimum value R_0. From Fig. 4.3, the approximated expressions of the range swath (ΔX) and the azimuth swath (ΔY) can be derived as

$$\Delta X \approx \frac{R_0 \theta_x}{\cos\theta} \quad \text{and} \quad \Delta Y \approx R_0 \theta_y, \tag{4.2}$$

where R_0 is the distance between the radar and the antenna footprint centre. The minimum and maximum ranges (referred to as "near range" and "'far range") determined by the time between the pulse transmission and the start and end of the reception period.

4.2.1 SAR resolution

Spatial resolution is one of the essential properties in a SAR imaging system [71]. It represents the capability of the imaging system to separate between two adjacent scatterers that can still be resolved in the final image. To achieve high resolution in range, very short pulse duration with high energy is necessary, however, it is difficult to be achieved with practical transmitters [55]. A "pulse compression" method is adopted to achieve the range resolution similar to the use of short pulses [64]. That is, the radar emits linearly modulated pulses called a "chirp" that are in frequency for a duration of time Δt. The pulse length (τ) is compressed to a sufficient duration equal to $1/B$ using signal processing methods such as the matched filter [81]. The slant range resolution is then given by

$$\delta_r = \frac{c\tau}{2}, \tag{4.3}$$

where c is the speed of light. The ground range resolution δ_x is the change in ground range associated with a slant range of δ_r, with

$$\delta_x = \frac{c\tau}{2sin\theta}, \tag{4.4}$$

where θ is the angle of incidence. So, the ground range resolution varies non-linearly across the swath. The ground range resolution is equal to half the footprint of the radar pulse on the surface and is different for different incidence angles.

A high resolution in azimuth thus requires large antennas. The solution to achieve high resolution without the use of a large antenna is given by the concept of "synthetic aperture" [82, 19, 83, 84]. This larger aperture network does not physically exist but is synthesised by sequentially gathering data (using the small single antenna) at different positions which collectively define the antenna array. The antenna is sequentially positioned along the flight direction in a straight line for each transmit,

receive and store operation [19, 55]. The maximum length for the synthetic aperture is the length of the flight path from which a scatterer is illuminated and is equal to the size of the antenna footprint on the ground (ΔY) [55, 64]. When a scatterer, at a given range R_0, is coherently integrated along the flight track, the azimuth resolution is then equal to

$$\delta_y = \frac{D_Y}{2}. \tag{4.5}$$

Equation (4.5) shows that SAR is independent of the distance between the ground and sensor, and is equal to half the size of the physical antenna length (D_Y) [85].

For a conventional single-channel SAR a higher azimuth resolution cannot be achieved for wide swath. Improving the azimuth resolution results in a greater Doppler bandwidth of the received echo signal and thus increasing the *PRF* due to higher sampling. The echo window length is then reduced which restricts the time accessible for receiving the echoes and thus decreasing swath width [64]. The difference between these ranges (the swath-width) is always selected to lie within the main lobe of the elevation beam. Since transmission and reception cannot overlap, the swath-width is restricted by the *PRF* and the condition

$$swath < \frac{c}{2 * PRF} \tag{4.6}$$

must hold. Disrupting these limits will cause image ambiguities such as target appearing at multiple or incorrect positions in the image. Methods such as multichannel digital beamforming have been developed to overcome these constraints [86].

4.2.2 SAR signal processing

The objective of SAR processing is to reconstruct the imaged scene from the many pulses reflected by every single target, received by the antenna and registered at all positions along the flight path [87]. The returned signal is converted to the digital number by the receiver and the function of the data recorder is to store data values for later processing and display [55, 71, 88, 86]. Some procedures have been developed to efficiently process SAR data from its raw signals into well-focused images [64]. The most straightforward and accurate technique to achieve image formation is the 2-D matched filter or “Range-Doppler” algorithm [89, 55]. Once raw data have been processed in terms of range

(pulse compression) and azimuth (SAR synthesis), a two-dimensional table of complex data (antenna direction, satellite track) physically related to the sensor is obtained and can now be described as an image.

4.2.2.1 SAR complex image

A SAR image describes the Earth's surface as a 2-D array divided into small areas represented as pixels formed by columns and rows. The SAR system properties determine the pixel size (area covered) [71]. The image is in a multiplex format where a single pixel comprised of amplitude (intensity squared) and phase (angle) information. Each pixel is considered to be the equivalent size as a separate resolution cell. However, this assumption is not always valid for a processed complex SAR image where the pixel size depends on the sampling interval [90, 67]. The amplitudes of each pixel are proportional to the magnitude of radar backscatter and they depend on the SAR system properties (i.e., wavelength, polarization) and scattering objects physical (i.e., geometry, roughness) and electrical properties (i.e., permittivity) [91, 64]. Phases of a complex SAR image are randomly distributed over the interval $(0, 2\pi]$, granted that there are more than 4–8 randomly distributed primary scatterers within a resolution cell [67]. Thus, phase does not provide information on the scattering objects. This type of SAR data is also referred to as Single-Look Complex (SLC). The advantage SLC data is the phase information which is the foundation of interferometric techniques. However, SLC images are very speckled and can be visually challenging to interpret due to the rectangular pixel geometry (e.g., Sentinel-1 SLC EW mode image pixel geometry dimensions are $5.9\,\text{m} \times 34.7\,\text{m}$ in range and azimuth direction, respectively [69]).

4.2.2.2 SAR multilook image

A way to improve the estimation of the mean intensity (σ) is to average L independent intensity values related to the same position. Multilooking is a process that maintains σ but reduces the estimator variance to σ^2/L. Multilooking provides easily usable images with square pixels based on ground geometry. Sub-sampling (in azimuth) and over-sampling (in range) filtering is done on the data in terms of nominal resolution, such that speckle reduction and look angle variation along the swath can be noted. The final image is displayed regarding intensity values so that each image pixel indicates the reflectivity of the corresponding point on the ground. This involves two additional steps applied to the

output of the processor: calibration and geocoding. The calibration ensures that the intensity value represents the sigma zero (σ_0) value of the reflectivity, i.e., the normalised radar cross section (NRCS) to the area. Conventional calibration is a non-trivial task requiring both internal instrument calibration as well as external SAR calibration using targets of known reflectivity or fixed corner reflectors [90]. In contrast, geocoding assures that the location of any pixel in the SAR image is directly correlated with the position on the Earth's surface. The data are over-sampled in range and sub-sampled in azimuth. For a Sentinel 1 GRD EW mode (high resolution) image, the pixel size is 25 m $\times$ 25 m (compared with the 5.9 m $\times$ 34.7 m SLC pixel size) [69]. However, the cost for the improved estimation accuracy is spatial resolution loss (by a factor L) and the loss of complex values.

4.2.2.3 SAR speckle

Speckle, usually referred to as noise, is a physical measurement of the resolution cell structure at sub-resolution level. Several randomly distributed elemental scatterers within a small area of the imaged scene (resolution cell) cause an adverse effect called *speckle* effect [55]. The coherent sum of randomly distributed elemental scatterers amplitudes and phases,

$$Ae^{j\phi} = \sum_i A_i e^{j\phi_i}. \tag{4.7}$$

Equation (4.7) results in strong variations of the backscattering from multiple neighbouring resolution cells [92], see illustration in Fig. 4.4. The amplitudes (A_i) and phases (ϕ_i) for each i^{th} elemental scatterer within each resolution cell results from several factors, including propagation attenuation, scattering of the illuminated targets and antenna direction [93]. Consequently, the power or *intensity* ($I = \sqrt{A}$) and the phase in the final image are no longer deterministic, but follow instead an exponential and uniform distribution, respectively.

Speckle is regarded as multiplicative noise, i.e., its variance increases with its intensity and cannot be reduced by increasing the transmit signal power [93]. To mitigate speckle a technique known as multilook is utilised, which is basically a non-coherent averaging of the intensity image. Independent *looks* of a target resolution cell are obtained by averaging L spatial observations. Multilooking can significantly decrease speckle effect and consequently the interpretability of the SAR image. However, the improved interpretability comes at a loss to image resolution. Furthermore, using very high-

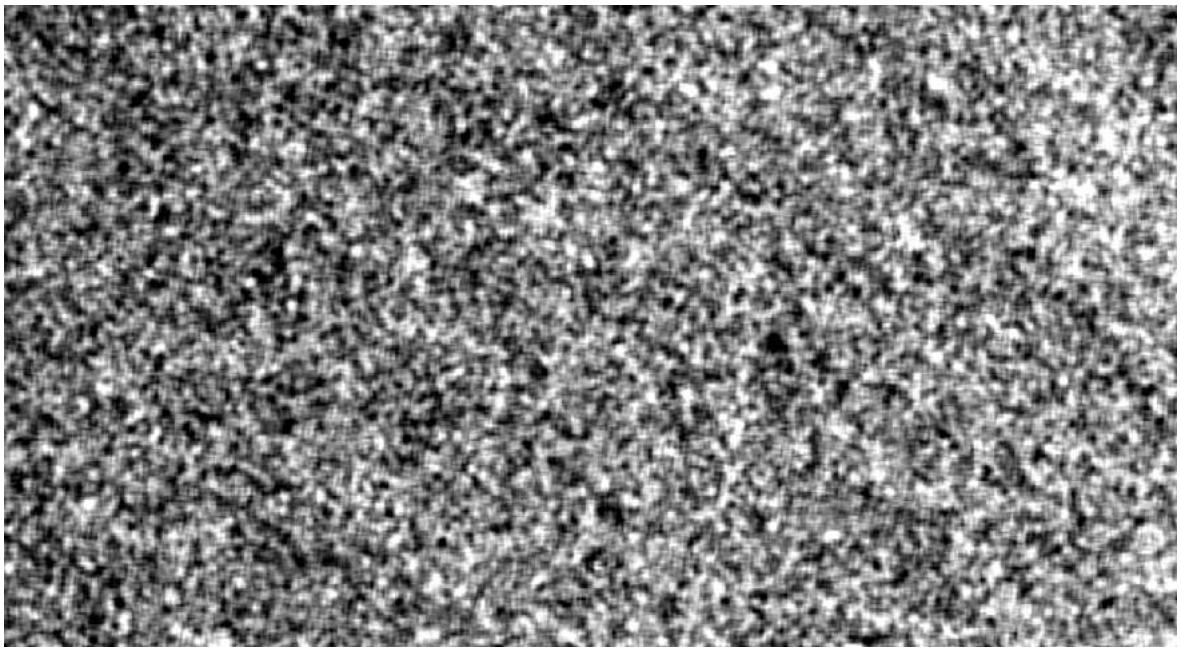

Figure 4.4. Typical speckle pattern.

resolution modes reduces the impact of speckle due to the decreased number of scatterer objects within each resolution cell.

4.3 SAR IMAGING OIL SPILL

The radar backscatter measures surface scattering and volume scattering from the ocean surface and man-made objects such as vessels, respectively. The ocean surface roughness and dielectric constant are the main properties for ocean radar imaging. The wavelengths of the small-scale wave (also called short-gravity waves) of the ocean surface must satisfy the Bragg resonance condition,

$$L_{Bragg} = \lambda/(2\sin\theta_i), \tag{4.8}$$

where L_{Bragg} is the wavelength of small-scale waves, λ is the radar wavelength and θ_i is the incidence angle [94, 95, 96]. The radar backscatter is emphasised by temporal and spatial variations of the Bragg waves created by maritime features such as ocean waves, internal waves and ocean wind. The above mentioned maritime features determine surface roughness, see examples of surface roughness in Fig.4.5. Whether a surface is rough or smooth is also subject to the radar wavelength and incidence angle [67]. The SAR response to Bragg scattering means that the instrument can view any large-scale ocean or atmospheric feature that generates, dampens or modulates these waves. These features include

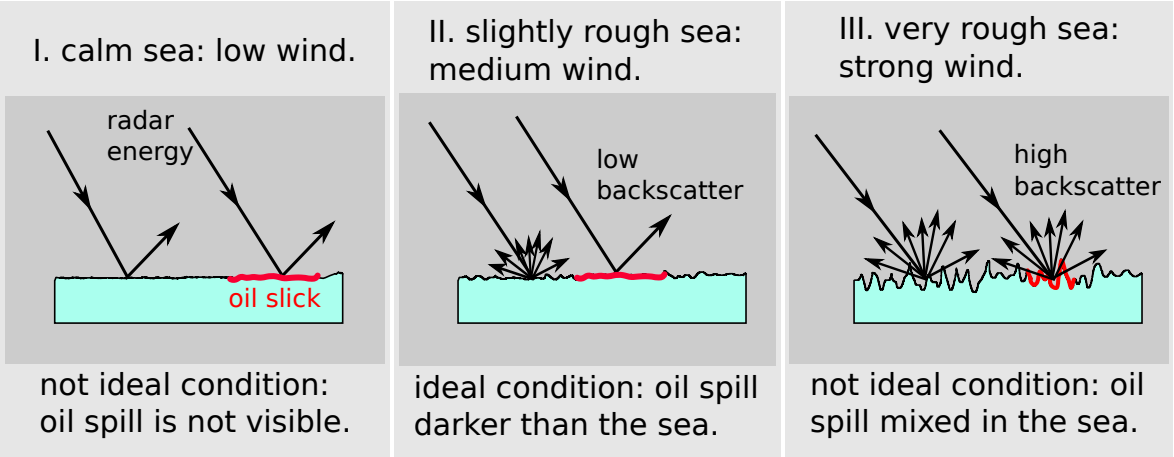

Figure 4.5. Example of SAR backscatter variations on different ocean surfaces.

surface slicks, ocean currents, long-period surface waves and internal waves. The atmospheric features include rain, wind bursts and weather fronts. Other than in topographic applications, microwave signals do not penetrate the surface of the ocean beyond a few millimetres. The SAR image represents a two-dimensional radar backscatter map of the ocean surface roughness.

SAR generates electromagnetic pulses that "illuminate" the ocean surface. Radar pulses are reflected by capillary waves that the wind creates at the surface of the sea (sea clutter). Without Bragg waves, the surface is "mirror-like" and most of the incident microwave is reflected away in the specular direction. Oil and other natural phenomena (surface current patterns, i.e. and biological activity) has a larger surface tension than water and they suppress capillary waves and reduce the level of the signal returned to the emitter. The suppressed regions appear as darkspots on a SAR image due to the low energy returned. In general, oil slicks can be classified based on characteristics of the shape of darkspot [97, 98], see Fig. 4.6:

1. Thin, linear dark patches might be oil spills caused by a moving ship or a stationary object, such as an oil platform, releasing a small amount of oil under certain wind and surface current conditions. Because of spreading and wind, older oil spills may appear wider than fresh spills.
2. Thin, piece-wise linear slicks caused by a moving ship changing directions, or a thin slick altered by wind or changes in surface current affecting oil released from a stationary object.

A stationary source releasing a larger amount of oil is identified by a wide dark patches. Spills captured

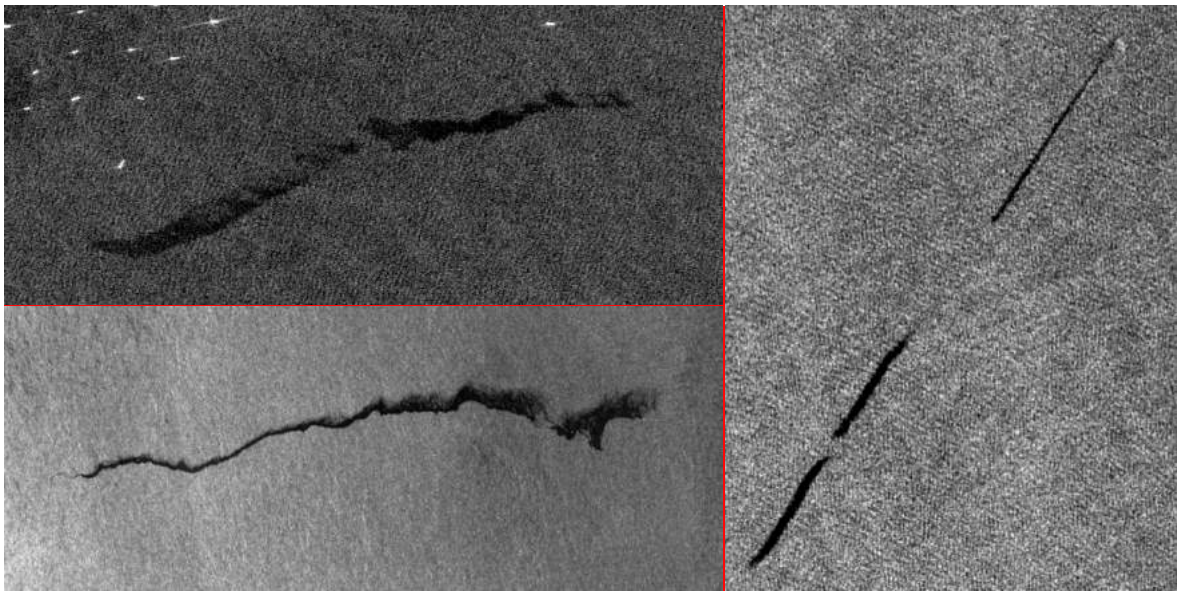

Figure 4.6. Examples of different shaped oil slicks (linear darkspots) caused by moving vessels. Bright spots on the top left of the top left image represent vessels. (Red boundaries separate the images).

early appear regular while older spills are more irregular due to the wind and surface current effects. Specular reflectors such as ships, offshore structures and icebergs are also visible [99]. Physical objects such as oil platforms and ships increase the level of the signal returned to the emitter and are seen as very bright spots on a SAR image [100, 101], see Fig. 4.6 top left image. The presence of vessels or a platform near a dark object increases the probability that the detected darkspot is an oil spill. If there is not a bright spot, then the darkspot tails can be due to a wind sheltering action caused by natural profiles, such as island bays. This makes SAR a critical sensor to detect an oil spill event with its source at sea.

4.3.1 Oil spill look-alikes

SAR provides a variety of information about oceanographic and sea ice processes [102]. For the ice-free ocean, SAR is used in the study of internal waves [103], surface waves [104] and ocean eddies [105]. Other phenomena visible in SAR include shallow-bottom topography, ocean currents, surface patterns of rain and wind and the presence of oil and other surface-modifying substances [106].

The main problem in the detection of oil slick features is to separate the dark features caused by oil slick from other look-alikes such as calm sea surfaces, rain cells, upwelling and biogenic slicks, see

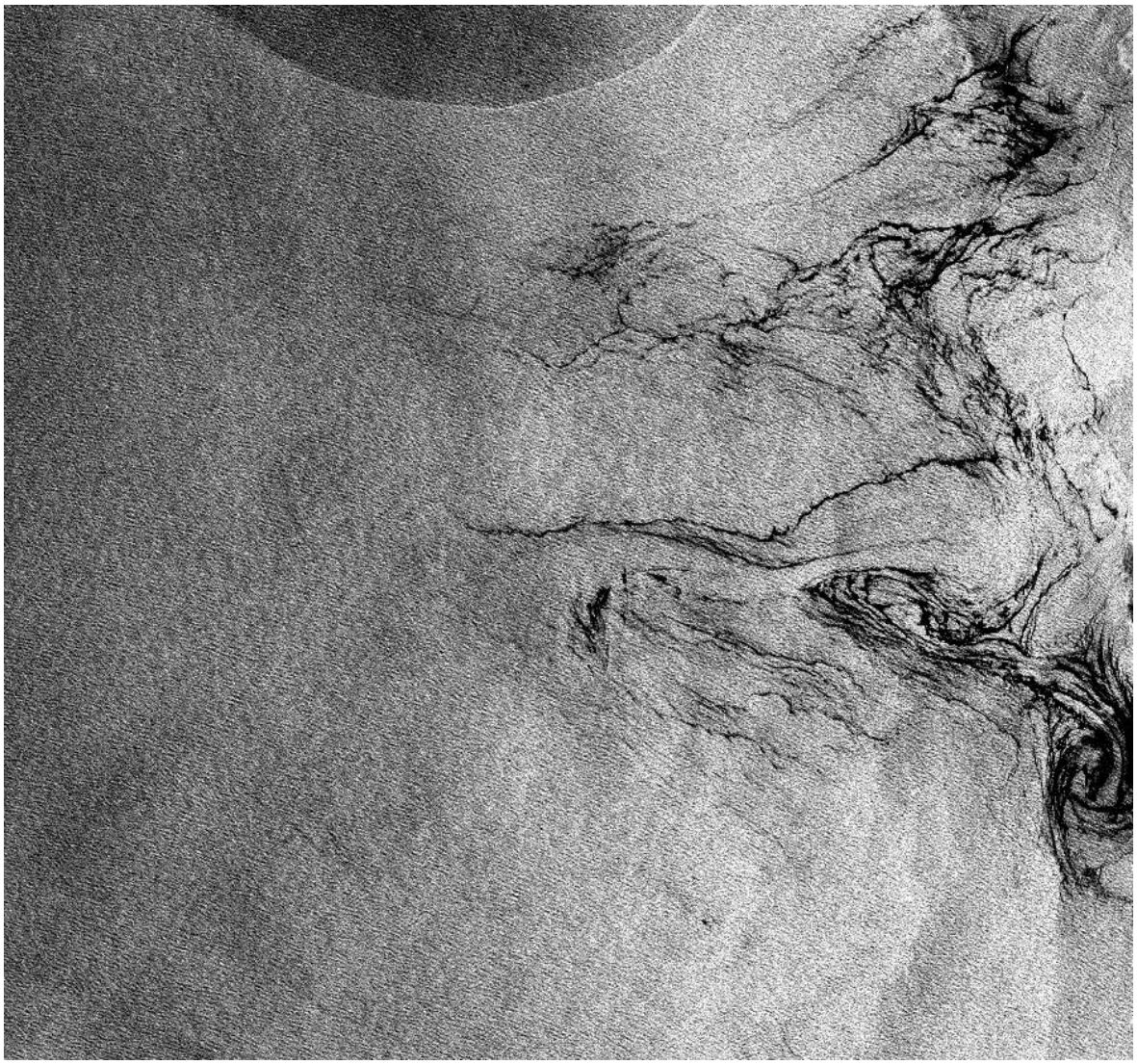

Figure 4.7. SAR image with multiple non-oil darkspots (i.e., oil spill look-alikes).

Fig. 4.7. If oil is discharged from a moving ship, a linear dark oil trail appears in SAR images, but the shapes of slicks become complex if the oil is discharged from a manoeuvring ship and strong non-uniform surface currents are present.

4.3.2 SAR parameters

To successfully detect oil spill from SAR, a set of particular conditions are required. These include internal SAR instrument requirements and external environmental conditions. The SAR viewing geometry along with the wavelength and polarization of the radar signal is the fundamental factor that influences the normalised radar cross section (NRCS). As discussed, radar images describe the backscatter return from the ocean surface roughness at the scale of the radar wavelength. The radar backscatter is also a function of the viewing geometry and incidence angle of the SAR where high incidence angles can decrease the backscatter. SAR polarization of the incoming radar signal influences the scattering properties of a material. The ability to detect oil spills from SAR is dependent on these parameters [17].

4.3.2.1 SAR sensor parameters

The backscatter of the ocean surface rapidly decreases with increasing radar incidence angle. Since oil spill damping of the Bragg resonant wave is more efficient at shorter wavelengths, frequency bands such X-band (2.4 cm to 3.75 cm) and C-band (3.75 cm to 7.5cm) are most used since they have approximately the same scale as the Bragg waves [107]. Experimental work on oil spills has shown that vertical antenna polarizations for both transmission and reception (VV) yield better contrast between oil slick and ocean surface than other configurations [67, 95]. According to radar theory, the radar backscatter is higher when using VV polarization because of the larger dielectric constant of the ocean surface [82]. Cross-polarized (VH or HV) images are generally not used due to weaker backscatter than co-polarized images [108]. Polarimetric data, especially when acquired as fully polarimetric data, can yield more information than single polarization data, thus potentially improve detection accuracy and assist classification of oil spills [109, 110, 15]. SAR sensors cannot achieve high spatial resolution and broad swath coverage simultaneously. Application requirements thus determine the choice between using high resolution or large swath. Because of the vast area covered by the ocean, typically large swath width is recommended for monitoring oil spill.

4.3.2.2 Ocean conditions

Oil spill detection by SAR is considerably affected by the sea state linked with wind speed, see illustration in Fig. 4.5. In fact, the low sea state does not produce sufficient surface roughness in the surrounding sea area, while high sea state generates homogeneous backscattering. Generally, depending on the oil spill type and thickness, the critical low wind speed level is in the range 2 – 4 ms^{-1}, while the critical high wind speed level is in the range of 12 – 14 ms^{-1} [3]. Where at low wind, an oil slick is impossible to detect since the contrast between an oil spill and the low backscatter (due to limited sea surface roughness) is very small making discrimination very difficult, see Fig. 4.8. At high wind speeds, the oil spill will rapidly spread and mix with sea water; the ocean surface becomes very rough, such that the damping effect becomes negligible. Oil dispersion is also caused by dissolution, oxidisation and bio-degradation. Thus, with increasing time from the oil discharge and with increasing wind speed, oil slicks become nearly impossible to detect. The time it takes oil to disperse varies from a day to weeks, depending on several factors such as the type of oil, amount of discharge and meteorological conditions, see section 2.2.2.

4.4 SUMMARY

SAR allows high-resolution imagery from a small size physical antenna while using longer wavelengths. Surface roughness and permittivity are the fundamental properties that govern microwave EM wave interaction with the elementary scatterers. The ocean, at wind speeds greater than 2 – 4 ms^{-1}, creates small gravity and capillary waves (or sea clutter) which increase radar backscatter returning a brighter image. For a calm sea state (i.e., at low wind speed), the ocean surface deflects the radar signal, returning a darker image. Marine oil spill simulates similar conditions by damping ocean capillary waves, which creates a reflective surface. Possible oil spills can then be detected by analysing the darkspots from SAR imagery. The damping effect is not unique to oil, other phenomena (denoted as look-alikes) can dampen ocean capillary waves and can be confused with an actual oil spill. Specular reflectors such as ships and offshore structures highly reflect radar backscatter, returning very bright spots in the image. SAR can detect not only possible oil spills but also the source of the spill. For this reason, SAR is the most used remote sensing tool for oil spill monitoring.

There are important factors to consider when imaging oil spills, including sensor parameters and

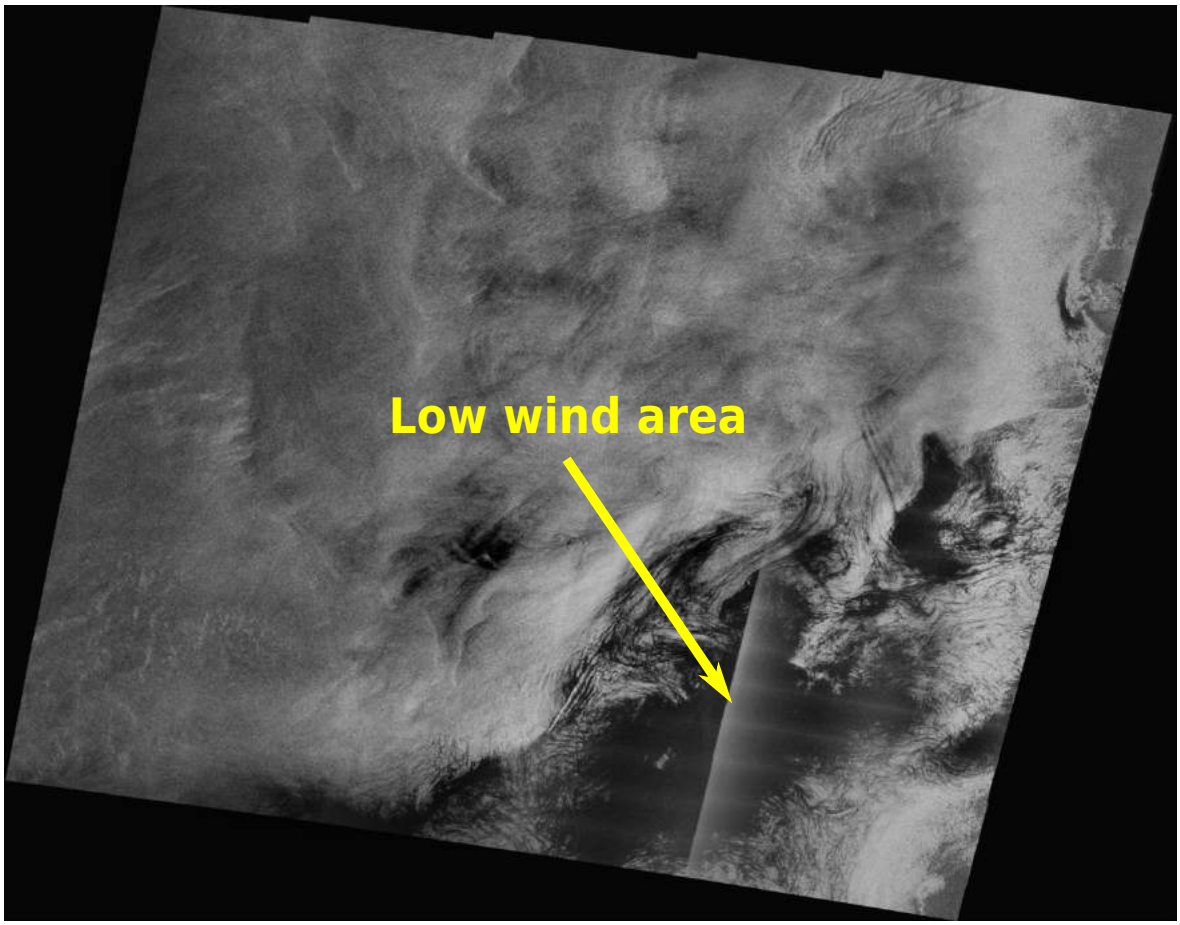

Figure 4.8. SAR image with dark region caused by low wind in the area.

ocean conditions. The most suitable SAR configuration for slick detection is C-band (3.75 – 7.5 cm) single-polarized VV SAR at incidence angles in the range of 20° to 45°. For an oil spill to be detectable, wind speeds must be between 2 – 14 ms^{-1}.

CHAPTER 5 OIL SPILL DETECTION USING SAR: A REVIEW

5.1 BACKGROUND

Digital grey-tones represent SAR backscattered signal for each resolution cell. The grey-tones are related to the backscatter of the scattering object where a dark (pixel value= 0) represents a low backscatter return and bright (high pixel value) represents a high backscatter return.

Manual oil spill detection in a SAR image is usually done by a trained human interpreter who visually inspects SAR images for any possible spills [44]. The operator assigns confidence levels on the detected possible oil spills based on multiple indicators from the images and external information concerning location, weather conditions, wind speed, correlating responsible source, natural slicks or low-wind areas nearby, and oil slick features, see section 4.3. Extracting the information can be a time-consuming task, particularly when many images must be examined [32, 38]. Furthermore, there is no guarantee of consistency between analysts or a measure of the performance they achieve [111]. These limitations motivate the search for automatic algorithms to derive the relevant information more quickly, or, in some circumstances, more sensitively, and in a reproducible manner.

It is more feasible to use automatic oil detection approaches as the number of SAR scenes to be analysed and their complexity increases [16]. Numerous image processing methods have been used for oil spill detection from SAR images [32, 7, 112]. The detection process can be broadly divided into four broad categories, see flowchart in Fig. 5.1 [97, 32, 38, 44]. Preprocessing refers to any processing done prior to darkspot detection, these include image enhancement processes or the removal of land areas. Darkspot detection involves identifying all dark regions (low value pixels) caused by damping

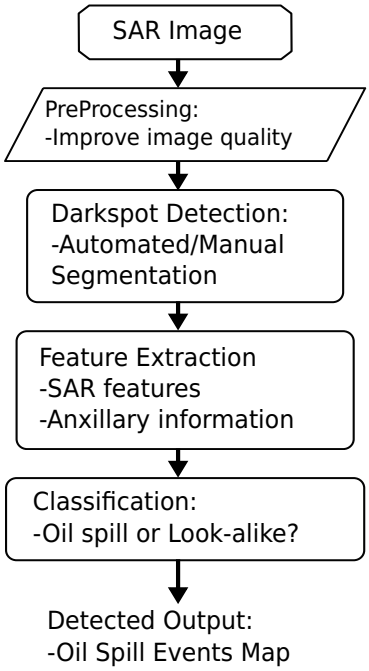

Figure 5.1. Typical automated oil spill detection process with SAR imagery.

effects due to the presence of oil slicks, see section 4.3. Discrimination involves two steps: feature extraction and classification. Feature extraction refers to the calculating of various features from the detected darkspot, such as geometry and mean intensity, to be used as input for further analysis [113]. The classification uses machine learning algorithms, which analyse the extracted features to classify the detected darkspot as oil pollutants or natural features [17, 114].

5.2 PREPROCESSING

However, oil spill detection can be challenging, especially when there is a presence of intensity inhomogeneity, speckle noise, wind speeds, and weak oil spill boundaries in an image [17, 113, 95]. Intensity inhomogeneity and speckle noise may cause unwanted effects during segmentation. Low winds result in decreased Bragg waves resulting in darker regions that may limit oil spill visibility [95, 106]. High winds may split or disperse oil spill and decrease the chances of detecting them [17, 113].

The main drawback of all SAR images is the presence of speckle. Speckle is a signal dependent

granular noise that visually degrades the appearance of SAR images, refer to section 4.2.2.3. Speckle may severely diminish the performances of automated image analysis. It has been observed that segmentation and classification can be improved if speckle is reduced [32]. Speckle reduction through speckle filtering techniques is thus regarded as an essential SAR preprocessing step [115]. SAR speckle is usually modelled as a multiplicative noise, and as a consequence, a number of filtering algorithms dealing with multiplicative noise have been proposed and used in the SAR image processing [116, 117, 118, 119, 120]. The most used methods for single polarization SAR data, include the Lee filter [121, 71], Frost filter [122] and Kuan filter [123]. The ideal speckle filter should adaptively reduce the standard deviation while preserving the mean, object edges and textural information [124, 115].

Wind velocity information is essential for a successful oil spill detection system. Espedal and Wahl developed a procedure to use wind history information for SAR oil spill detection [125]. Solberg *et al.* proposed a threshold-based oil spill detected algorithm that used wind as input [16]. Wind velocity can be obtained from external sources (e.g., weather stations) or derived directly from a SAR image. Wind direction retrieval and wind speed retrieval from SAR are performed to produce 180° ambiguous wind velocity vectors. The resolution of the ambiguity in the wind direction is resolved by comparing with coarser wind directions from a numerical weather model. The output of the algorithm is the wind velocity vectors for the SAR image location. Salvatori *et al.* estimate the wind speed from the SAR image by applying an inverted CMOD4 model (developed by ESA for wind vector evaluation of C-band scatterometer) [126].

5.3 DARKSPOT DETECTION

In a SAR image, an oil spill appears as a dark object (denoted as darkspot) when compared to the brighter ocean surface. Other darkspots include low wind areas, organic film, fronts, areas sheltered by land, rain cells, current shear zones, grease i.e., internal waves, upwelling zones, downwelling zones and eddies, see section 4.3.1. Potential oil spills can be detected by isolating, contouring and cropping the border area of all dark signatures, through appropriate threshold and segmentation processing of the image.

Darkspot detection is a two-class classification problem where each pixel is assigned to either a darkspot class or a surrounding sea class. Typically, darkspot detection can be performed either in

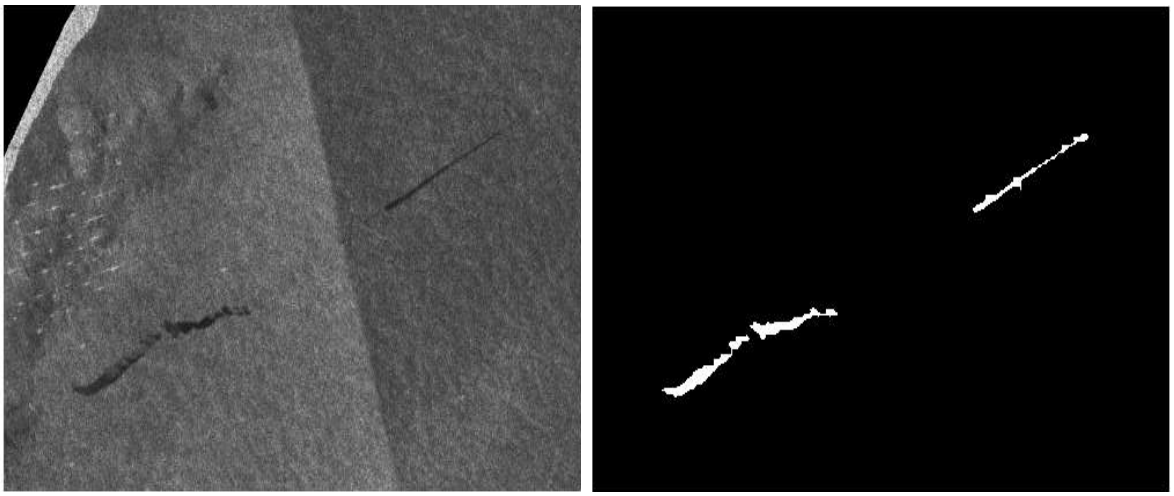

Figure 5.2. Example of a Sentinel-1A Extra Wide mode SAR sub-image (left) and segmented sub-image (right) with oil spills.

manually or automatically. Manual darkspot detection involves an operator that investigates the images and selects regions with the probable oil slicks. Automatic darkspot detection suggests using a fully-automated or semi-automated oil spill detection system to select regions with the probable oil slicks [3]. Several image processing algorithms have been presented for darkspot detection using SAR images. The algorithms can be grouped as, but are not limited to, adaptive thresholding methods [16, 127], hysteresis thresholding [128], mathematical morphological thresholding [129, 130], edge detection methods [131], region-based methods [132, 133] and neural networks based methods [134].

Threshold methods are darkspot detection methods based on the image grey-tone histogram analysis. The threshold value is an essential parameter for threshold methods as it determines the division of darkspots from the surrounding sea. In 1999, Solberg *et al.* [16] presented an adaptive threshold algorithm to detect darkspots from SAR images. The authors calculated a threshold value k dB set below local mean backscatter values across a moving window that adaptively changed according to the region wind speed information. The method was tested using 84 images and was able to detect all oil spills from the test set. The shortcomings of Threshold-based methods is the high dependence on the threshold value which can also lead to over-segmentation [133].

Edge detection methods suffer from over-segmentation and split edges and they extract all abrupt changes in image intensities [133]. This is not ideal for SAR images due to the presence of speckle noise. Edge detectors are sensitive to the rough sea state noise, which results in lots of false alarms that

can be difficult to eliminate [135]. In addition, detected edge points need to be linked into a continuous edge, which is difficult to implement in most cases because of the split darkspot [132].

In comparison with the conventional intensity thresholding and edge detection methods, the ACM and level set approach can directly extract features from noisy images, allowing an extraction of smooth and ideal boundaries. Oil spill events in rough seas or strong ocean surface currents can also be detected, including all other darkspot present in the image. However, it is not trivial to discriminate the oil spill from look-alikes caused by natural phenomena (e.g., natural oil spills, surface currents and eddies) [32]. These algorithms are also not ideal, however, as they tend to be computationally expensive, sensitive to initialisation and are also limited by weak edge boundaries [133].

Artificial Neural Networks (ANNs) have also been proposed for darkspot segmentation [136, 137]. They have been reported to outperform the established edge detection and adaptive thresholding approaches [136]. However, to accurately detect ocean pollution with neural network algorithms, the user requires a large dataset with many ocean pollution samples for training [134].

5.4 FEATURE EXTRACTION

Feature extraction involves the extraction of a vector of features that quantitatively describe relevant characteristics of the object. Extracted features should exhibit a clear relationship between the value of the selected feature and the probability of it being an oil spill [136]. The most common features of darkspots and a limited area outside the darkspot (oil spill free area) were extracted from the sub-images. These features can be categorised as geometric, physical and texture features. Geometric features describe the geometry and shape of the segmented darkspots. A wide range of geometrical features have been proposed, where some features have been found more useful than others [138]. Physical features describe the backscatter values of the darkspot and its surroundings. These are considered as the most important features for discriminating oil spills from look-alikes [136]. Textural features describe the underlying texture of the darkspot and the region around it. These have been shown to be the least important features for oil slick discrimination [138, 136]. However, some studies have shown that Haralick textures [139], can be useful to a certain extent [140]. A detailed description can be found in Table 5.1 and from literature [141] and [138]. Feature extraction is a very important task as it is input for classification, it helps the system to discriminate the oil spills from look-alikes.

Table 5.1. Common oil spill discrimination features.

Object Geometry Features:
Area (A), Perimeter (P)
Perimeter to Area ratio (P/A)
Complexity (C)
Shape factor 1 and 2 (SP1, SP2)
Physical Features:
Object: Mean, Std deviation, Power to mean ratio (OMe, OSd, Opm)
Background: Mean, Std deviation, Power to mean ratio (BMe, BSd, Bpm)
Object/Background: Mean, Std deviation, Power to mean ratio (RaMe, RaSd, Opm/Bpm)
Border gradient: Mean, Std deviation, Power to mean ratio (GMe, GSd, Gpm)
Contrast ratio: Mean, Std deviation, Local area (ConRaMe, ConRaSd, ConLa)
Border gradient: Min, Max (Gmin, Gmax)
Contrast: Mean, Max (ConMe, ConMax)
Mean difference to neighbours (NDm)
Object Texture Features:
Obejct: Spectral, Shape and Mean Haralick textures (TSp, TSh, THm)

5.4.1 Oil spill features

Once a possible oil slick (darkspot) has been detected from the SAR image, a set of objective measurements which are meant to separate a real oil slick from a look-alike is accomplished. There are three main groups of features that can be measured from darkspots, namely, geometry, physical, and texture information. The features are extracted from all detected darkspots and a limited area outside the darkspot (oil spill free area) in the SAR image.

5.4.1.1 Geometrical features

Geometrical features involve the analysis of the object's geometry and shape features. The shape of the slick is essential regarding discriminating between oil spills and look-alikes. The shape can also determine the cause of pollution. Oil spills ordinarily have a more regular form than look-alikes, especially, fresh oil spills from moving vessels [7]. The regular form refers to oil slicks that are linearly shaped due to vessel movements. The orientation and complexity of the oil slick can assist in distinguishing between oil and look-alikes [142]. The most common features are reported in Table 5.1.

5.4.1.2 Physical features

Physical features are based on the backscatter values of the segmented darkspot and its surroundings. These are considered as the most important features for oil spill discrimination from look-alikes. Similar to geometrical features, a wide range of physical features have been proposed. The most common features are reported in Table 5.1.

5.4.1.3 Texture features

Texture features are considered the least important for oil slick discrimination [32]. However, some studies have shown that textures based on the GLCM measure can be useful to a certain extent [143, 137] These are textures based on shape, spectral information and the mean Haralick textures. The challenge with texture features is that they are highly affected by the GLCM parameters, i.e., window size, angle and distance. The most common features are reported in Table 5.1.

5.4.2 Contextual features

In some cases it may not be possible to discriminate oil spills from natural/man-made look-alikes using only darkspot features [44]. The discrimination is particularly difficult in presence of natural oil slicks or areas with low wind speeds [32]. In these situations more information is necessary, critical information include the sea state (wind speed and direction), nearby source (automatic information

system (AIS) ship tracking, location of oil rigs, pipeline), location of spill for impact analysis (national territory borders and coastlines). Espedal *et al.* successfully developed an oil spill detection procedure that used wind history information for SAR [125]. The authors were able to determine the age of the spill by analysing the wind history together with the oil slick shape to approximate the oil spill start and end time.

5.4.2.1 Ships information

Usually a bright spot can be seen in the vicinity, representing a ship or platform. The presence of vessels or a platform near a darkspot increases the probability that the detected darkspot is an oil spill. If there is not a bright spot, then the darkspot tails can be due to a wind sheltering action caused by natural profiles, such as island bays. Ships are assumed to be the source of the pollution, and the presence of a vessel is therefore regarded as a significant characteristic of an illicit discharge [52].

5.4.2.2 Wind information

The information of wind speeds can considerably improve the discrimination of oil spills from look-alikes [52]. The wind speed history information is also essential for analysing the shape, size and age of the oil slick. The life-span of the oil spill and wind speeds can be used to determine how persistent is the slick and consequently help determine the oil spill type [3].

5.4.2.3 Geolocation information

Geographic location is a necessary feature for improving oil spill discrimination. Knowledge of coastal lines can help reduce false alarms caused by the sudden changes from a region wind is blowing to low wind region (sheltering action). Additional geographic features such as the location of the natural oil slick, marine protected areas and oil platform locations can be especially useful for oil spill detection [3].

5.4.2.4 Multiple images and polarisation

Multiple images may be required to examine adjacent scenes along the same pass and other scenes from different dates of the same location. Images from other sensors such as optical data can also be used with SAR to improve results. Multifrequency and multi-polarization SAR is often preferred for oil spill discrimination. Images from other satellites (e.g., optical imagery) can also be used to reduce false detections.

However, contextual features may not always be available/visible in the image. For example, multiple images over the same area are particularly difficult to obtain from the same source. Because of the lower revisit time of spaceborne sensors, the associated ship of a detected linear darkspot can be outside the captured scene. Adjacent scenes depend on the spill alignment to the path of acquisition, and different dates depend on the satellite temporal resolution and spill life span. Another challenge is the computational cost of processing and interpreting large quantities of images rapidly and accurately during an emergency.

5.5 OIL SPILL DISCRIMINATION

As a number of phenomena can create dark patches in a SAR image (see section 4.3.1), it can be challenging to accurately discriminate the real oil spill features from look-alikes. The last discrimination step usually involves a classification process based on machine learning algorithms [17, 114]. Classification differentiates between oil spills and look-alikes. It includes testing of the selected features against predefined values that describe oil spills. Generally, statistical methods are used to compute probabilities to decide an unknown object class category. That is, darkspots that are above a given probability threshold are considered to be oil spills or not oil spills based on its features.

Kubat *et al.* [144], provided a comprehensive overview of the issues of developing a machine learning system related to oil spill detection. The author examined common issues such as problem formulation, selection of evaluation measures, imbalanced class distribution and data preparation. An accuracy test is required to compare the number of correctly classified dumps over falsely classified targets. However, the large number of false targets over the actual oil spill presents a problem (that is, an image can

have two oil spill events and hundreds of false alarms). This is a big challenge when evaluating bilge detection algorithms, thus more effective methods are required over traditional methods [144].

5.5.1 Feature selection

The use of all the features described in section 5.4 may not be a feasible choice due to the curse of dimensionality. In fact, not all oil spill features have the same discriminating power, some of the features may be correlated, some are not always consistent. Much work has been done on oil spill feature selection and feature ranking to determine features that yield the highest classification. Also, the capability of the selected features is measured using various evaluation measures. The feature selection method is terminated when the most significant features have been determined or when the highest value of the evaluation measure is accomplished [145].

A feature selection method, based on genetic algorithm optimisation, that concurrently searches for the best feature combinations has been shown to achieve higher classification accuracy than standard sequential selection methods [141, 32]. The main drawback of the genetic based algorithm is the increased demand in computational resources. Fiscella *et al.* identified several features that contributed significantly in the discrimination process [146]. The features were based on ocean conditions (wind speed) and the source of the oil spill (described by darkspot form factor). Statistical methods such as the one-way analysis of variance (ANOVA) have been successfully used to select the effective feature variables [98]. The ANOVA uses probability values to determine if a variable is statistically significant [147].

Topouzelis *et al.* [148] in a 2012 study concluded that there was not a single optimum feature combination out of the 25 most common combinations considered but several sets of combinations existed which contained at least some critical features. Lui *et al.* only found five features to be important for identification of ocean oil spills in SAR imagery. Oil spill and look-alike darkspot features that have high variance (e.g., perimeter and area features) or lack of variance (e.g., minimum border gradient feature) between them are regarded as least important features and are usually discarded. High variance features included the darkspot size [136].

5.5.2 Oil spill classification

A variety of classification approaches have been used to distinguish oil spills and look-alikes from vectors of feature descriptors [148, 140, 149, 150, 16, 146, 136, 151]. Most classification algorithms are based on probability theory [142, 44, 145]. The methods use statistical information obtained from previous measurements of physical and geometrical characteristics for both oil spills and natural features. The probability approach uses statistical information obtained from extracted features to discriminate between oil spills and other natural phenomena. Detected oil slicks are usually classified into probability categories, that is, either low, medium or high probability. As per conventional method, first a training dataset is used as input for a classification algorithm and then test datasets are checked. Accuracy and efficiency of classification depend on the chosen algorithm. Rather than using the traditional two-class approach of oil spills and look-alikes classes, Gambardella *et al.* [152] proposed a one-class classification paradigm where the classifier was trained using only instances of oil spills.

The most common approaches include a Mahalanobis classifier [146], a statistical classifier [16, 142, 97], a neural network approach [136], a fuzzy logic classifier [153, 151, 98, 154], and a combination of a statistical classifier and a rule-based approach [51]. Fuzzy logic simulates the ways in which humans granulate information and reason with it [155]. The system uses a set of conditions based on known oil features which are used to classify oil spills from look-alikes. In certain cases fuzzy logic systems can yield higher detection accuracy and a lower false alarm rate (FAR) over statistical, neural network and other methods [98]. Keramitsologou *et al.* developed a fully automated system based on artificial intelligence fuzzy logic for the identification of possible oil spills present on SAR satellite images [151]. The system identified darkspots from SAR images and assigned a probability for each darkspot to be an oil spill. Solberg *et al.* [16] presented a method based on a combination of using prior knowledge, Gaussian densities and rule-based density corrections. The proposed algorithms achieved a classification accuracy of 94%, detecting 67 out of 71 oil spills, and a 1% false alarm rate, that is, only 75 out of 6980 look-alikes were wrongly classified. Singha *et al.* [136] developed an oil spill detection approach that used Artificial Neural Networks (ANN) to segment and classify oil spills from look-alikes. The authors correctly identified 91.6% of reported oil spills and 98.3% of look-alike phenomena found from 97 ERS-2 SAR and ENVISAT ASAR.

5.6 SUMMARY

Oil spill in SAR images appear as dark regions (termed darkspots) due to a dampening effect on the short gravity waves and thus can be detected on SAR images. Automated methods have been demonstrated as the more practical approach for oil slick monitoring from SAR images.

Darkspot detection is regarded as the most important for a successful oil spill detection system. Low winds, intensity inhomogeneity and speckle noise may cause unwanted effects during segmentation [95, 106]. High winds may split or disperse oil slick and decrease the chances of detecting it [17, 113]. The first step is to improve SAR image quality and remove unwanted features such as land in the image. This step is known as a preprocessing step and has been shown to improve the detection accuracy. The following step is to isolate darkspots, using segmentation methods, identifying all pixels caused by damping effects all possible oil spill objects. The segmentation process (or darkspot detection) can be achieved in numerous ways, where most methods are based on thresholding, edge detection and object detection. Not all darkspots in a SAR image are oil slicks, other non-oil slick objects have a similar dampening effect on capillary waves and can be incorrectly identified as oil spills. To limit the incorrect detections (false alarms) more processing is required. When all darkspots have been identified, the last step is to discriminate real oil spills from look-alikes. The discrimination uses machine learning algorithms, which use darkspot characteristics (extracted features) to classify the detected darkspots as oil pollutants or natural features. Extracted features include geometry, physical, textural and contextual information from each darkspot object. Statistical classifiers are the most used classifiers as they are rather simple, reliable and can be easily reproduced [32].

Darkspot detection is traditionally a time-consuming process [32]. An efficient and effective darkspot detection approach is essential for developing an automated oil slick detection system. Current methods based on thresholding, edge detection and object detection may be effective in detecting darkspots but are still not ideal. Region-based algorithms such as active contour models (ACM) and level set methods have been demonstrated to outperform earlier efforts that are based on adaptive thresholds or edge detection techniques [135, 132, 156]. However, region-based methods are computationally costly which can be a major limitation when a large number of SAR images need to be processed. Thus, a new efficient and effective darkspot detection approach is essential for developing an automated oil slick detection system.

Using all available features as input for a given classifier classification is computationally impractical. The selection of features that yield the highest discrimination of oil spills from look-alikes is still a challenge. The main difficulty is defining the features that will yield consistent performance. Thus, a reliable set of features is required for optimal discrimination. The main challenge is to identify a set of good features that can be used to discriminate between oil slicks and look-alikes. Also, the difference in classifiers and datasets make it difficult to directly compare classification and different detection approaches in terms of classification accuracy [51].

Considering the current oil spill detection challenges, particularly the segmentation and feature selection step, the study propose a novel oil spill detection framework. The proposed framework improves the current segmentation limitations and also improve the discrimination of illegal oil spill discharges from look-alikes. The next chapter presents the methodology of the proposed novel framework which includes a linear darkspot detection algorithms with improved discrimination process.

CHAPTER 6 A NOVEL FRAMEWORK FOR OIL SPILL DETECTION USING SAR

6.1 INTRODUCTION

Oil slick over the sea surface formed as a result of oil-tanker accidents or illegal bilge dumping of tankers can cause significant environmental damage depending on the location and amount. A rapid response is required to minimise the ecological impact caused. Oil slick discharges from ships can be monitored automatically using image processing methods on SAR images. However, this can be challenging when there is a presence of intensity inhomogeneity, speckle noise, wind speeds, and weak oil slick boundaries in an image. Intensity inhomogeneity and speckle noise may cause unwanted effects during segmentation. Low winds result in decreased Bragg waves resulting in darker regions that may limit oil slick visibility. High winds may split or disperse oil slick and decrease the chances of detecting it. Even with these challenges, numerous image processing methods have been used for oil slick detection from SAR images. However, these are still not ideal.

The oil spills from vessel discharges are regarded as a primary source of oil slicks and are estimated to be higher than accidental oil spills [157]. The study focused on the task of detecting oil spills from moving vessels using only the most critical features derived from a SAR image. The proposed framework consists of three main steps, that is, the preprocessing, the linear darkspot detection and the oil spill discrimination, see flowchart in Fig. 6.1. The framework uses a novel linear darkspot detection and an improved discrimination process. The linear detection process uses a segmentation-based algorithm to isolate linear darkspots from other features in the image. The improved discrimination process was accomplished by investigating the most relevant oil spill features to be used as input in a classification algorithm.

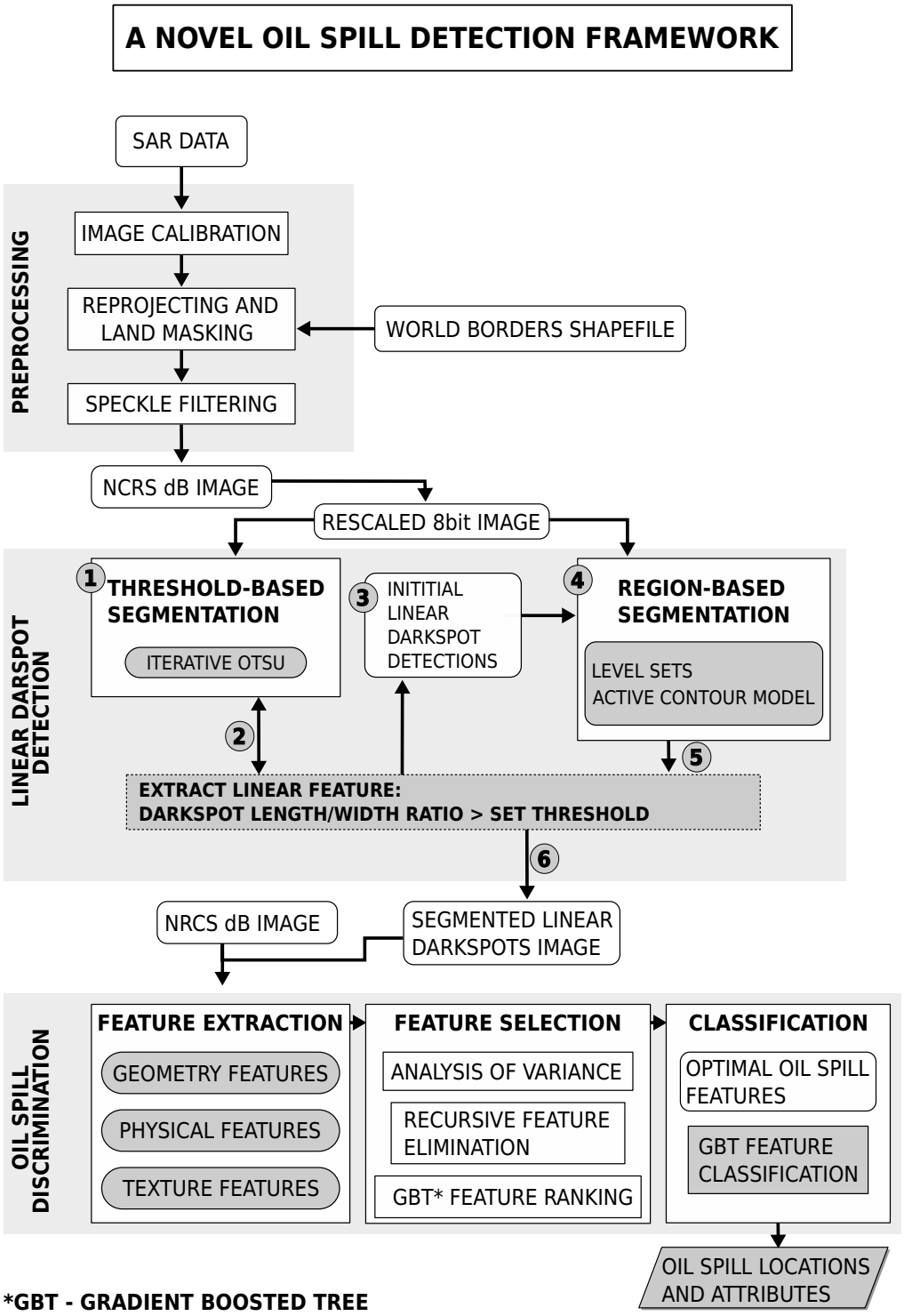

Figure 6.1. The flowchart of the proposed novel framework for monitoring oil spills from moving vessels using SAR.

6.2 PREPROCESSING

The SAR data were downloaded as 16bit (unsigned) images that needed to be preprocessed for oil spill detection. The preprocessing steps includes an 8-bit rescaled image and a calibrated dB scale sigma nought (σ_0) image, as shown in Fig. 6.1.

6.2.1 Image calibration

After removing land, the 16-bit SAR images were radiometrically corrected using a calibration algorithm. The calibration uses a look-up table [158] to create a sigma nought image (given in decibels (dB)). Calibrated pixel values are directly related to the radar backscatter of the scene and are used to calculate physical features (backscatter values). Sigma nought, also termed normalised radar cross section (NRCS), is a dimensionless quantity given in decibels (dB). The calibration was done using a look-up table provided in the metadata.

6.2.2 Reprojection and land masking

All images were reprojected (geo-referenced) by converting all pixel coordinates (x,y) to geographic (latitude, longitude) using WGS84 global geodetic ellipsoid reference from the tie point grids of the source product. A land masking operation was then applied to remove land areas and isolate ocean areas, any pixel on land was assigned a null value using a world land shapefile as mask.

6.2.3 Rescaling to 8-bit gray image

The NRCS images were converted to 8-bit values using a re-scale algorithm. A min–max re-scale algorithm was used, with the maximum value set equal to the mean value plus three times the standard deviation value. The 8-bit image was used to produce a segmented image and to calculate gradient and texture features.

6.2.4 Speckle filtering

The 8-bit and NRCS images were enhanced using a refined Lee filter to reduce speckle noise, intensity inhomogeneity and preserve edges [121, 159], see Fig. 6.2 (details in section 6.2.4.1). The enhanced Lee filter uses a fixed (7×7) sliding window to detect an edge and its orientation (using a local gradient estimate).

6.2.4.1 Lee speckle filter description

The Lee speckle filter, known as Lee sigma filter, is based on the concept that 95.5% of pixels are distributed within the two-sigma range from its mean [121]. The filter reduces speckle noise using by replacing the centre pixel with a moving window with the average of the pixels within two-sigma range of the centre pixel. Pixels farther from the two-sigma range are regarded as outliers and are excluded from the calculation of the mean. The despeckling is performed by separating homogeneous areas with high-contrasting distributed scatterers. The filter combines the uncorrelated multiplicative speckle model [159]:

$$I(t) = R(t) \cdot u(t), \tag{6.1}$$

where $t = (x, y)$ is the spatial coordinate, $I(t)$ represent the intensity or amplitude of a SAR image, $R(t)$ is the reflectance (noise free), and $u(t)$ is a speckle noise [160]. $R(t)$ and $u(t)$ are assumed to be statistically independent and the local statistics of the ideal image $R(t)$ can be replaced as a function of the observed local statistics. Given the observation $I(t)$, the original signal $R(t)$ is estimated so that the minimum mean square error (MMSE) is achieved. The linear MMSE filter estimate can be written as a weighted sum of the observed and local mean values ($\hat{I}$ and $\hat{u}$):

$$\hat{R}(t) = \hat{I}(t) + w(t)[I(t) - \hat{I}], \tag{6.2}$$

where w is the weighting function given by

$$w(t) = 1 - \frac{C_u^2}{C_I^2(t)}. \tag{6.3}$$

$C_I = \sigma_I / \hat{I}$ is the observed coefficient of variation and $C_u = \sigma_u / \hat{u}$ is the noise variation coefficient.

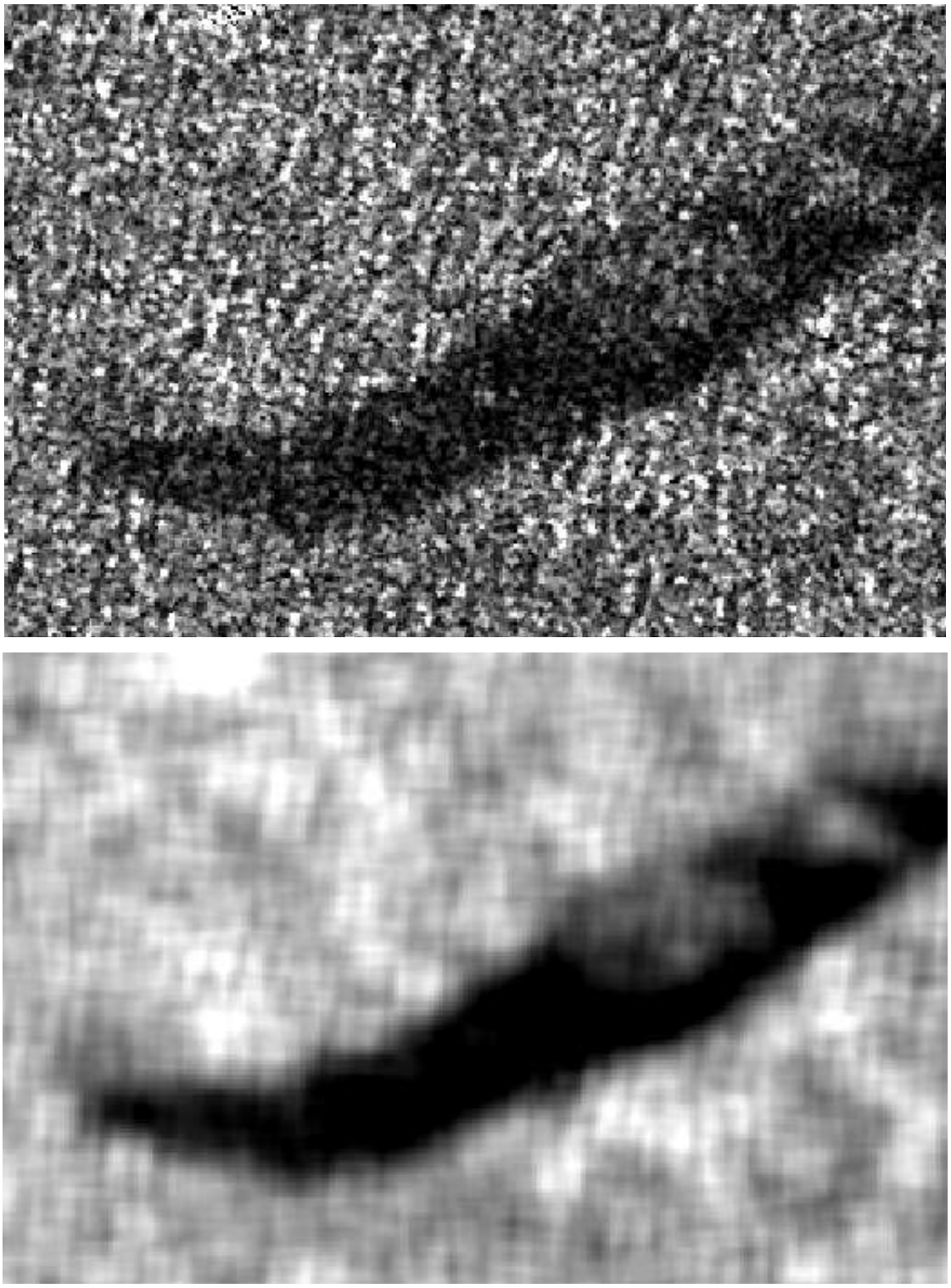

Figure 6.2. An example of a SAR image before speckle filtering (top image) and after speckle filtering (bottom image).

6.3 LINEAR DARKSPOT DETECTION

The study proposed a novel image segmentation method that focused on detecting possible oil slick (location and full extent) from SAR images, see Fig. 6.1. The proposed method solves both the threshold-based and region-based algorithm limitations by using a two-step approach. First, a threshold-based method was used to detect all linear darkspots (areas with a high oil slick probability). Second, a region-based approach was used to extract the full extent of the identified linear darkspot area. Details of the proposed linear darkspot detection process with reference to Fig. 6.1 follow.

6.3.1 Threshold-based segmentation

The proposed threshold-based algorithm uses a histogram-based algorithm known as Otsu's method [161]. The method automatically computes an optimal threshold (T_{Otsu}) and segments darkspots (with levels $[1,\ldots,T]$) from the surrounding sea (with levels $[T+1,\ldots,L]$). T is the chosen threshold value and L is the maximum gray-level value.

6.3.1.1 Otsu method description

Suppose $\mu, \sigma^2_{ds}(T)$, $\sigma^2_{ss}(T)$ represent the mean level of the image, the darkspot class variance and surrounding sea class variance, respectively:

$$\mu = \sum_{i=1}^{L} g_i p_i = P_0(T)\mu_0(T) + P_1(T)\mu_1(T), \tag{6.4}$$

$$\sigma^2_{ds}(T) = P_0(T)(\mu_0(T) - \mu)^2 + P_1(T)(\mu_1(T) - \mu)^2, \tag{6.5}$$

$$\sigma^2_{ss}(T) = P_0(T)\sigma^2_0(T) + P_1(T)\sigma^2_1(T). \tag{6.6}$$

Where

- g_i and p_i respectively denote gray-value i and the corresponding empirical probability value;
- $P_0(T) = \sum_{i=1}^{T} p_i$ and $P_1(T) = \sum_{i=T+1}^{L} p_i$ denote the cumulative probabilities;
- $\mu_0 = \sum_{i=1}^{T} g_i p_i$ and $\mu_1 = \sum_{i=T+1}^{L} g_i p_i$ denote the mean levels;
- $\sigma^2_0(T)$ and $\sigma^2_1(T)$ denote the variances of the classes C_0 and C_1.

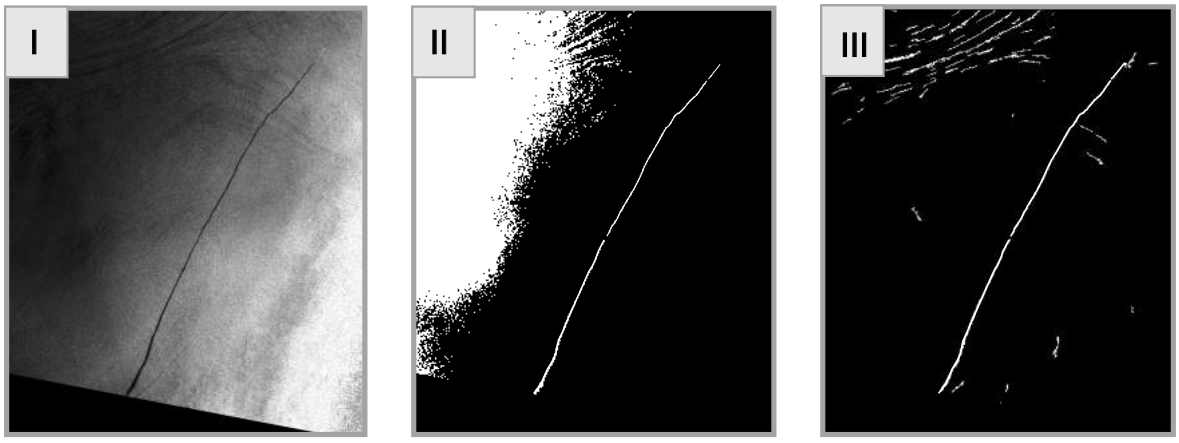

Figure 6.3. SEN1 enhanced image (I); Segmentation using the normal Otsu threshold algorithm (II) versus using Proposed Iterative Otsu algorithm (III).

According to [161], the threshold T_{Otsu} is decided by maximising the between-class variance:

$$T_{Otsu} = \underset{1 \leq T < L}{\operatorname{argmax}} \{\sigma_{ds}^2(T)\}, \tag{6.7}$$

which is also equivalent to minimising the within-class variance:

$$T_{Otsu} = \underset{1 \leq T < L}{\operatorname{argmin}} \{\sigma_{ss}^2(T)\}. \tag{6.8}$$

An optimal threshold (or set of thresholds) was selected by maximising the measure of separability between the darkspots and non-darkspot (sea) classes in grey intensity levels, see (6.7).

6.3.1.2 Iterative Otsu method description

SAR images, however, can have dark regions caused by a calm sea state which can reduce the visibility of small oil slick events [113]. These dark regions and high variations within the image made the selection of optimal threshold value difficult for the Otsu method, see illustration in Fig. (6.3:II). In order for the proposed framework to be robust to these challenges, a new threshold-based algorithm was proposed. The proposed threshold-based component, iteratively segmented darkspots while extracting potential oil slicks (linear darkspots), as shown in Fig. 6.4.

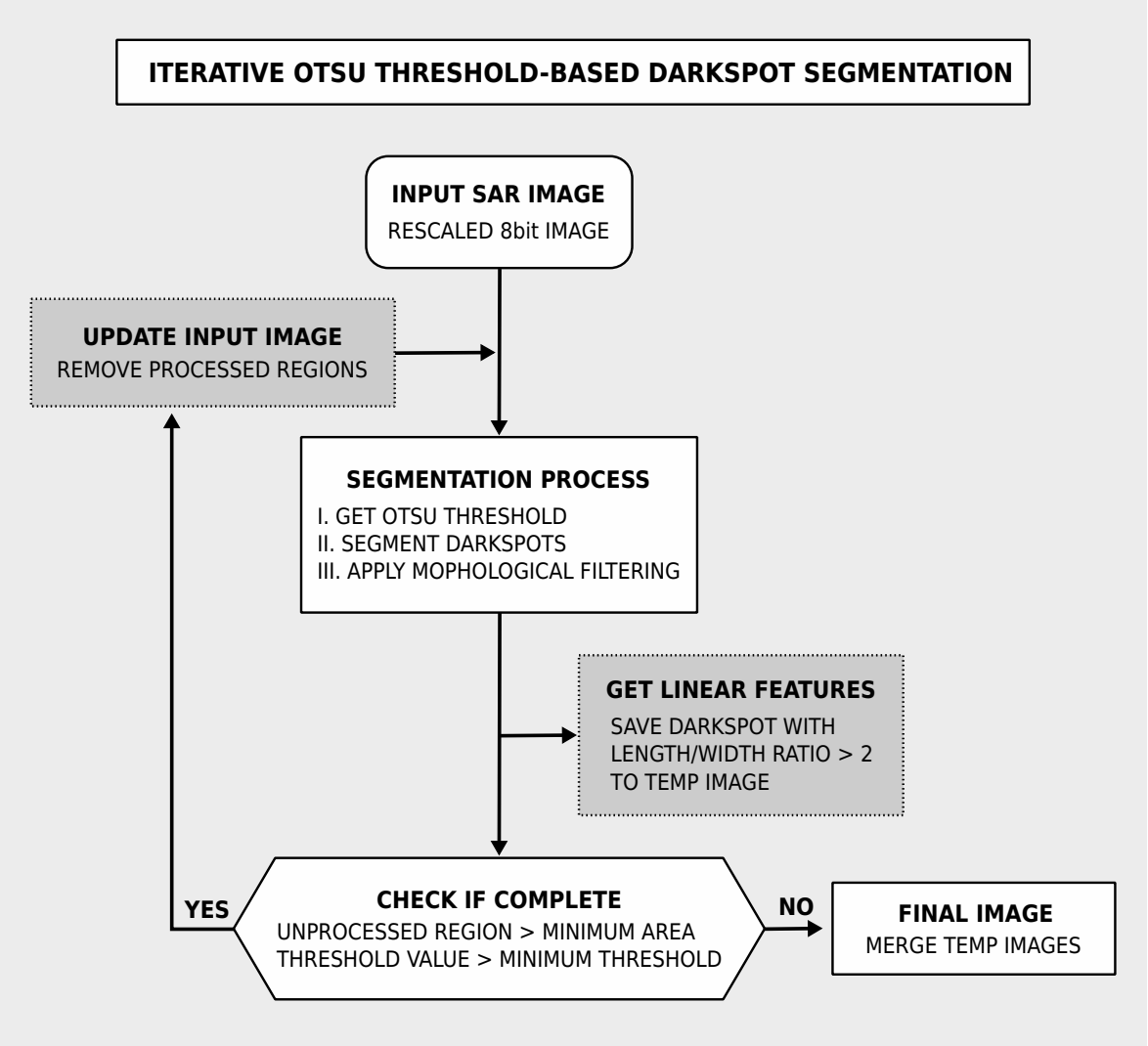

Figure 6.4. Detailed flowchart of the proposed iterative Otsu threshold linear darkspot segmentation algorithm.

Linear features were extracted using geometrical features (length, width and length to width ratio) from the detected darkspots. The length, width and aspect ratio were calculated automatically by fitting a rectangle around the detected darkspots. All detected linear features for each iteration are stored as temporal images until all regions of the input image have been processed or when the threshold value reaches zero or was no longer changing. A rectangle with an extended length was fitted around the detected linear features to merge nearby darkspots. A large square box was fit around the detected linear darkspots to extract the regions of interest. The region-based algorithm was then applied to these areas. The proposed iterative Otsu method showed improved detection of linear darkspots when compared to the normal Otsu threshold algorithm, Fig. (6.3:III).

6.3.2 Region-based segmentation

Threshold-based algorithms do not always detect the full extent of oil slick events as they can be split or oversegmented due to the limitations of the threshold-based algorithms [16]. The proposed framework used a region-based method that used an active contour model (ACM) and level set algorithm to overcome the shortcomings of threshold-based methods by detecting the full extent of oil slick events, see flowchart in Fig. 6.1. The ACM is based on a new region-based signed pressure force (SPF) function [162]. It utilises the statistical information inside and outside the contour to control the contour evolution. This property allowed the method to efficiently stop the contours at weak or blurred edges and thus can automatically detect the exterior and interior boundaries of potential oil slicks.

6.3.2.1 Active contour model description

Active contour model (ACM) methods represent a contour using a zero level (initial contour) of a function called the level set function (ϕ), and the image was segmented by evolving the level set formulation. The evolution equation was obtained by minimising an energy function of the signed pressure force (SPF) function [162]:

$$\frac{\partial \phi}{\partial t} = spf(I(x,y)) \cdot \alpha | \bigtriangledown \phi |, \qquad x,y \in \Omega, \tag{6.9}$$

where α is the balloon force, and Ω is a bounded subset of $I(x,y \in \Re^2)$ in the given image. The balloon force parameter controls the shrinkage/expanding of the contour evolution. A high α may cause the contour to pass weak edges while a low α may cause the contour not to pass narrow parts of the object.

Initialisation of the level set function ($\phi(x,t=0)$) is zero at the boundary, negative inside and positive outside the contour:

$$\phi(x,t=0) = \begin{cases} -\rho & x \in \Omega_0 - \partial\Omega_0, \\ 0 & x \in \partial\Omega_0, \\ \rho & x \in \Omega - \Omega_0, \end{cases} \tag{6.10}$$

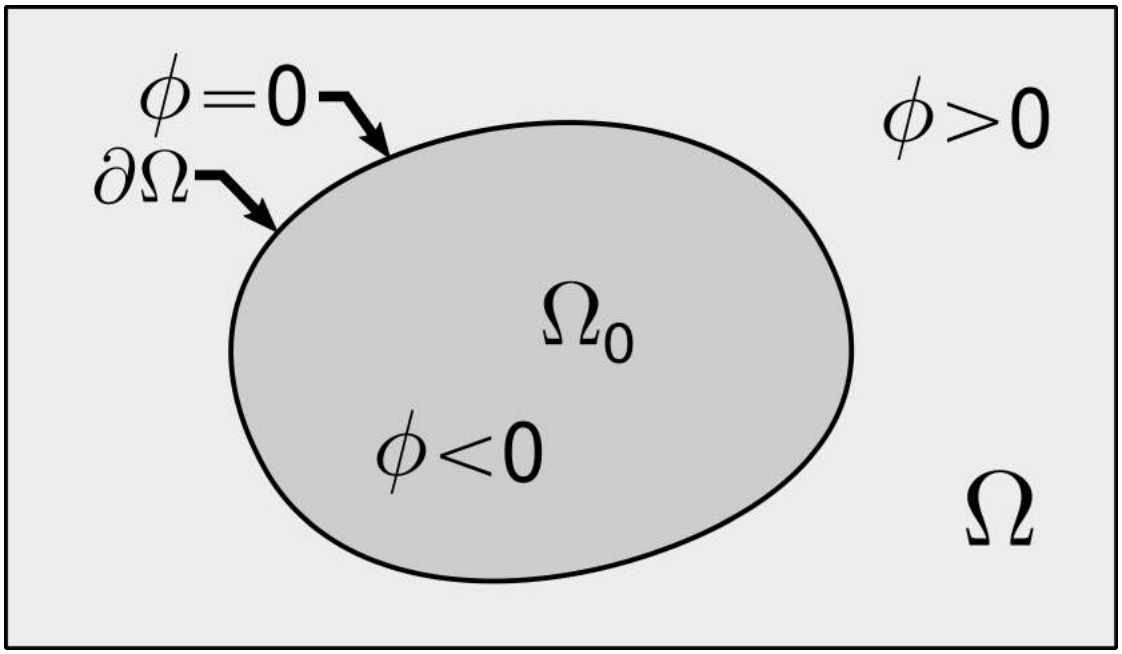

Figure 6.5. The level set formulation: the signs of the SPF function inside and outside the object.

where $\rho > 0$ is a constant, Ω_0 is a subset in the image domain Ω and $\partial\Omega_0$ is the boundary of Ω_0.

The proposed framework used the linear darkspot detected from the threshold-based algorithm as the initial contour ρ. The initial contour size determined the limited subset size. The signed pressure function (spf) has values in the range [-1, 1] and is defined as:

$$spf(I(x,y)) = \frac{I(x,y) - \frac{c_1+c_2}{2}}{\max(|I(x,y) - \frac{c_1+c_2}{2}|)}, \qquad x,y \in \Omega, \tag{6.11}$$

where the two constants, c_1 and c_2, are the average intensities inside and outside the contour, respectively. Constants $c_1(\phi)$ and $c_2(\phi)$ are defined by

$$c_1(\phi) = \frac{\int_\Omega I(x) \cdot H(\phi) dx}{\int_\Omega H(\phi) dx}, \tag{6.12}$$

$$c_2(\phi) = \frac{\int_\Omega I(x) \cdot (1 - H(\phi)) dx}{\int_\Omega (1 - H(\phi)) dx}. \tag{6.13}$$

$H(\phi)$ is the Heaviside function and is generally selected as:

$$H_\varepsilon(z) = \frac{1}{2}(1 + \frac{2}{\pi}\arctan(\frac{z}{\varepsilon})). \tag{6.14}$$

The level set function ϕ is then evolved according to (6.9). The SPF modulates the signs of the pressure forces inside and outside the region of interest so that the contour shrinks when outside the object or expands when inside the object, see Fig. 6.5. A Gaussian filter was used to regularise the level set to keep it stable and control its sensitivity to noise, that is: $\phi = \phi * G_\sigma$. The level set function ϕ evolved until converged. The standard deviation (σ) of the Gaussian filter is an essential parameters that are highly dependent on the image. Setting σ too low may cause the contour to be sensitive to noise while a high σ may smooth the images too much and cause edge leakage to occur.

The algorithm had both global and selective segmentation properties. The selective segmentation procedure is achieved by making the deviation $\Delta\phi$ that is far from the interface of level set function ϕ close to zero, and only the $\phi(x)$ near the interface will evolve [162]. Thus the level set function can start the contour near the object of interest to obtain the desired segmentation by setting $\phi = 1$ if $\phi > 0$; otherwise, $\phi = -1$. Using the selective property the initial contour can be placed contiguous to the object of interest.

6.4 OIL SPILL DISCRIMINATION

To reduce the number of false detections (i.e., look-alike detections) from a segmentation algorithm, the study proposed an improved discrimination process. The process involved three steps: firstly, identify the frequently used features in literature, secondly, identify the best features for our dataset, and lastly, classify oil spill events using the selected features.

6.4.1 Oil spill features

Several features need to be extracted to successfully discriminate oil spill events from look-alikes from a SAR image [141]. The first step was to determine all available (or the most relevant) darkspot features in literature, see Table 5.1 in section 5.4. A detailed description and calculations of the features reported in Table 5.1 are as follows [138, 141]:

- Area (A): the number of pixels of the darkspot objects.
- Perimeter (P): the length of the border pixels of the darkspot objects.
- Complexity ($C = P/2\sqrt{\pi A}$): describes how complex or simple the geometry of the darkspot objects are.
- Shape factor 1 (SP1): describes how long and thin the darkspot objects are. It is also referred to as spreading and as length to width ratio.
- Shape factor 2 (SP2): describes the general shape of the darkspot objects. It has also been referred to as first invariant planar moment, form factor and asymmetry.
- Mean (OMe or BMe): the mean of the intensity values of the darkspot objects or ocean background pixels.
- Std deviation (OSd or BSd): the standard deviation of the intensity values of the darkspot objects or ocean background pixels.
- Power to mean ratio (Opm or Bpm): the ratio between the standard deviation and mean values of the darkspot objects or ocean background pixels.
- Contrast local area (ConLa): the ratio between the mean value of the darkspot object (OMe) and the the mean of the intensity value of a window centred inside the darkspot object.

- Mean contrast (ConMe): the difference between the ocean background mean value (BMe) and the darkspot objects mean value (OMe).
- Mean border gradient (GMe): the mean of the magnitude of the gradient values of the region border area. It describes how dark the border gradient of the darkspot objects are. The Sobel operator [163, 164], is used to compute the gradients, see Fig. 6.6.
- Mean Haralick textures (THm) [139]: they are calculated as the average of the grey level co-occurrence values matrices of the sub-objects. The probability of the grey level co-occurrence values is defined as

$$p(i,j) = \frac{P(i,j;\theta,d)}{\sum_{i=1}\sum_{j=1} P(i,j;\theta,d)},$$

where $P(i,j;\theta,d)$ represents the number of occurrences of grey level i and j, which is separated by an offset d in direction θ.

The features were extracted from the calibrated and segmented SAR images, see experiment flowchart in Fig. 6.1. In the context of the oil-spill detection problem, the present state-of-the-art methods suggest to use features belonging to four classes, as presented in section 5.4.2. Features belonging to the fourth class include isolating the bright spots (ship candidates) from the image or using AIS information which may not always be visible in the image. The interest of the study is assessing the effectiveness of the proposed framework with regard to the quality of SAR data. As a consequence no contextual information could be derived. However, using ancillary information such as the knowledge of traffic routes, oil rigs and pipeline locations is critical for an operational oil spill detection monitoring system [17, 3, 76, 7].

6.4.2 Feature selection methods

Oil spill events can be related to different events, and depending on those, have different geometries which could influence which features are extracted/selected for the classification task. An important feature is one that enables the highest possible discrimination accuracy. The simple approach of selecting the best individual features is not trivial. It is therefore useful to employ feature selection techniques that take into account both the individual class separation capability and the dependencies

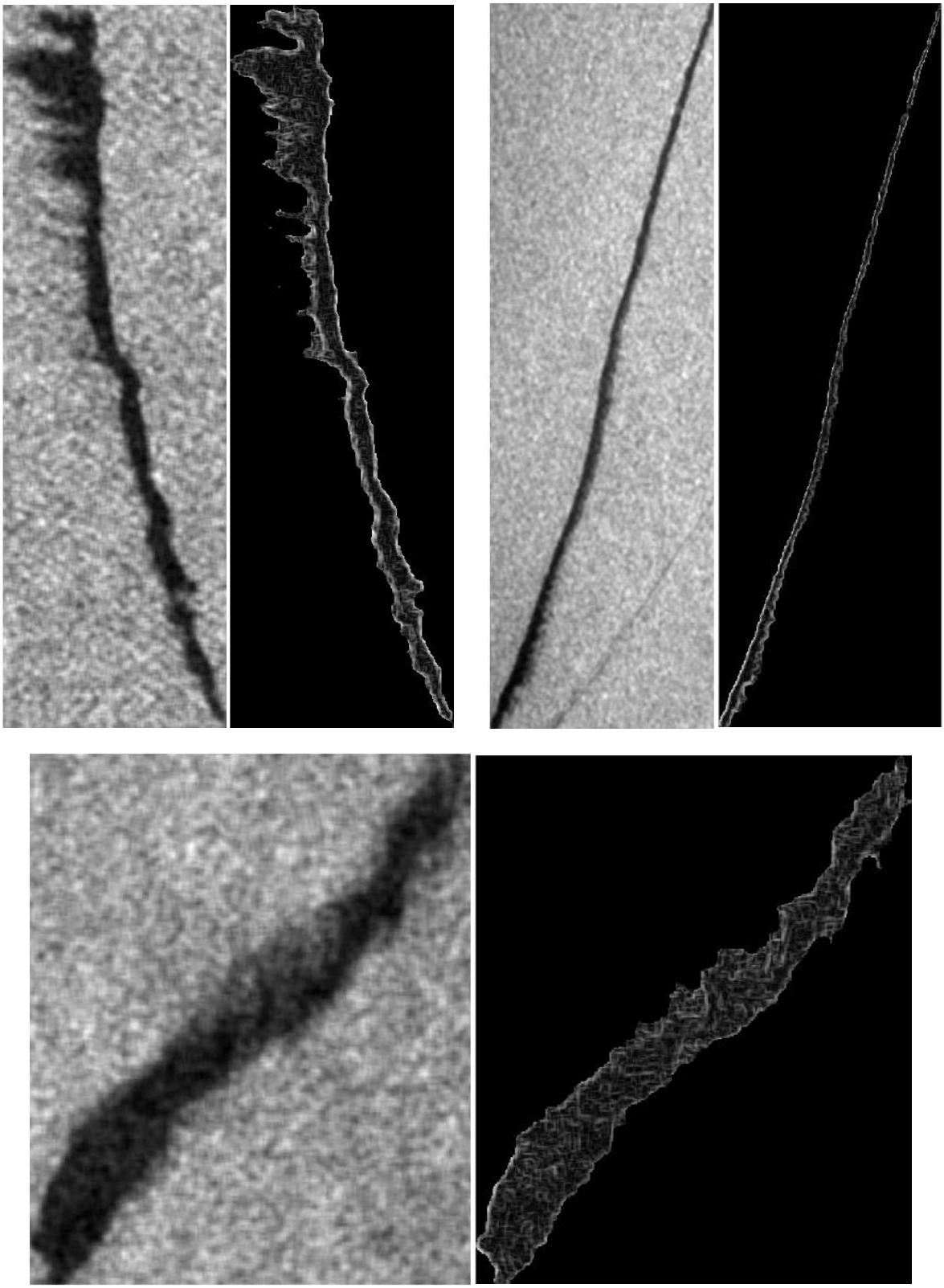

Figure 6.6. SAR subimages with darkspot gradients computed using the Sobel operator.

between the features. To select a small subset of very effective features, the study proposed a feature significance ranking system that evaluates the effectiveness of each feature using several feature selection algorithms.

6.4.2.1 Feature significance

Before describing the feature selection algorithms formally, the following definition of feature significance is introduced. Let $X_k = \{x_i : 1 \leq i \leq k, x_i \in Y\}$ be the set of k features from the set $Y = \{y_i : 1 \leq i \leq D\}$ of D available features. The *individual significance* $S_0(y_i)$ is the significance of the ith feature in $y_i, i = 1,2,\ldots,D$ according to a feature selection criterion function $J(y_i)$ [165]. The *significance* $S_{k-1}(x_j)$ of the feature $x_j, j = 1,2,\ldots,k$, in the set X_k is defined by

$$S_{k-1}(x_j) = J(X_k) - J(X_k - x_j), \tag{6.15}$$

where $J(\cdot)$ is the feature selection criterion function. Note that for $k = 1$, the term feature significance is equivalent to individual significance. The significance $S_{k+1}(y_j)$ of the feature y_j from the set $Y - X_k = \{y_i : i = 1,2,\ldots,D-k, y_i \in Y, y_i \neq x_i \text{ for all } x_i \in X_k\}$ with respect to the set X_k is defined by [165]:

$$S_{k+1}(y_i) = J(X_k + y_i) - J(X_k). \tag{6.16}$$

Using the above definitions, feature significance can be defined as follows [152, 165]:

- Feature x_j from the set X_k is:

  i) the most significant (best) feature in the set X_k if

  $$S_{k-1}(x_j) = \underset{1 \leq i \leq k}{\operatorname{argmax}}\, S_{k-1}(x_i) \tag{6.17}$$

  $$\Rightarrow J(X_k - x_j) = \underset{1 \leq i \leq k}{\operatorname{argmin}}\, J(X_k - x_i). \tag{6.18}$$

  ii) the least significant (worst) feature in the set X_k if

$$S_{k-1}(x_j) = \underset{1\leq i\leq k}{\operatorname{argmin}} S_{k-1}(x_i) \tag{6.19}$$

$$\Rightarrow J(X_k - x_j) = \underset{1\leq i\leq k}{\operatorname{argmax}} J(X_k - x_i). \tag{6.20}$$

- Feature y_j from the set $Y - X_k$ is

  i) the most significant (best) feature in the set X_k if

$$S_{k+1}(y_j) = \underset{1\leq i\leq D-k}{\operatorname{argmax}} S_{k+1}(y_i) \tag{6.21}$$

$$\Rightarrow J(X_k + y_j) = \underset{1\leq i\leq D-k}{\operatorname{argmax}} J(X_k + y_i). \tag{6.22}$$

  ii) the least significant (worst) feature in the set X_k if

$$S_{k+1}(y_j) = \underset{1\leq i\leq D-k}{\operatorname{argmin}} S_{k+1}(y_i) \tag{6.23}$$

$$\Rightarrow J(X_k + y_j) = \underset{1\leq i\leq D-k}{\operatorname{argmin}} J(X_k + y_i). \tag{6.24}$$

That is, a feature has significance if the accuracy measure is increased when it is removed as described in (6.18) or added as described in (6.22) in a feature set.

6.4.2.2 Feature ranking

In order to combine the results attained by different feature selection mechanisms, a heuristic approach is used [152]. Let m be the number of the feature selection techniques that should be combined. For each feature selection technique, a score based on the significance of each feature was measured. Feature ranking can be defined using a score system to each feature f_i as follows [152]:

$$\text{score}(f_i, k) = \sum_{j=1}^{m} \text{rank}(f_i, \text{sel}_j, k), \tag{6.25}$$

where the function rank(f_i,sel$_j$,k) is defined as

$$= \begin{cases} 1 & \text{if } f_i \text{ is ranked among the first } k \text{ values by sel}_j \\ 0 & \text{otherwise,} \end{cases} \tag{6.26}$$

where f_i is the ith feature (with $1 \leq i \leq D$), and sel_j is the jth selection technique (with $1 \leq j \leq m$). Then, we select the features f_i that satisfy

$$f_i(k) = \underset{i}{\text{argmax}}(\text{score}(f_i, k)). \tag{6.27}$$

Significant features are those that frequently rank high from the feature selection algorithms. Different values of k produced different subsets of features which were combined by considering the union of the subsets produced by different values of k. Features that satisfy (6.27) for different values of k can be considered to have a large discriminating capability [152]. A global score for each feature f_i, was measured for different values of k which satisfied (6.27). The study computed mean significance value assigned by the selection algorithms based on the majority voting criterion. In order to select a subset of features, the thresholds were chosen from low, medium and high rank features.

6.4.2.3 Feature selection procedure

The selection of the optimal subset of features for a given classification problem requires the evaluation of all the possible subsets with regard to some predefined evaluation criteria [152]. The feature selection process is stopped when a predefined maximum number of features (k) is selected, or the desired value of the evaluation criterion is attained. A number of evaluation criteria have been devised to estimate the effectiveness of the selected features [138, 141, 152].

In order to exploit the complementary of different selection algorithms and evaluation criteria, the study proposes to perform feature selection by combining four selection algorithms widely adopted in the literature, namely Recursive Feature Elimination, Forward Feature Selection and Analysis of Variance. The Gradient Boosted Tree (GBT) classifier was used as evaluation criteria to measure the effectiveness of each feature selection method.

Recursive Feature Elimination (RFE): The RFE method first considers all available features and then removes the remaining features one at a time, so that the next feature set is the one that provides the largest improvement of the evaluation criterion employed. Consider a set of features (x_k) at iteration k. Feature x^- is removed at iteration $(k-1)$ if the remaining features produce the largest improvement of the evaluation criterion $GBT(\cdot)$, that is

$$GBT(x_k - x^-) \geq GBT(x_k - x) \text{ for all } x \neq x^-. \tag{6.28}$$

Forward Feature Selection (FFS): The FFS method does the opposite of the RFE procedure. It first considers the most discriminating feature according to an evaluation criterion, and then adds the remaining features once at a time, so that the next added feature is the one that provides the largest improvement of the evaluation criterion employed. In other words, let Y_k be the set of features at iteration k. Feature x^+ is added at iteration $(k+1)$ if this addition produces the largest improvement of the evaluation criterion $J(\cdot)$, that is

$$J(Y_k + x^+) \geq J(Y_k + x) \text{ for all } x \neq x^+. \tag{6.29}$$

Statistical Analysis: A one way ANOVA is used to compare two means from two independent groups using the F-distribution. A one-way analysis of variance (ANOVA) was used to select the effective feature variables. ANOVA determines whether there were any statistically significant features using differences between the means of two or more independent features. That is, for each feature the sample mean and sample variance was estimated and compared using the F-test taken from Snedecor F-Table [166].

6.4.3 Gradient boosted tree classifier

Boosting refers to applying multiple weak estimators to produce a more powerful estimator. Gradient Boosted Tree (GBT) classifier builds an estimator by sequentially adding new tree learners to the expansion model. GBT sequence of tree expansions are of the form:

$$F_m = \sum_{m=1}^{M} T(x, \Theta_m), \tag{6.30}$$

where $T(x;\Theta)$ is the *weak tree estimator* of the input variables x, characterised by parameters Θ_m. For regression tree, the parameters Θ_m are the splitting variables, split locations and the terminal node of the individual trees [167].

Equation (6.30) is a minimisation problem that can be solved numerically using the steepest descent direction method [168]. The steepest descent direction is the negative gradient of the loss function evaluated at the current model (F_{m-1}):

$$F_m(x) = F_{m-1}(x) + \gamma_m T(x, \Theta_m), \tag{6.31}$$

where γ_m is the step length chosen using line search:

$$\gamma_m = \underset{\gamma}{\operatorname{argmin}} \sum_{i=1}^{N} L(y_i, F_{m-1}(x_i) + \gamma T(x_i, \Theta_m)).$$

Equation (6.31) can be calculated for any differentiable loss function. For classification, the negative binomial log-likelihood (also known as deviance) is the commonly used loss function $L(y,F)$:

$$log(1+e^{2yF}) \text{ for y } \in \{-1,1\}.$$

6.4.3.1 GBT parameters

The GBT classifier has the following critical parameters:

Number of Trees: This parameter controls the number of boosting stages to perform. GBT is relatively robust to over-fitting so a large number can be used without losing performance. However, oversized trees can substantially degrade performance and increase computation.

Shrinkage or Learning Rate: Shrinkage controls how strongly each tree tries to correct the mistakes of the previous trees and is dependent on the number of trees. Shrinkage is implemented by scaling the contribution of each tree by a factor α when it is added to the current approximation (6.31):

$$F_m(x) = F_{m-1}(x) + \alpha\gamma_m T(x, \Theta_m).$$

Sub-sampling: This parameter controls the number of samples to be used for fitting the individual base learners. Not only does the sampling reduce the computing time, but can also produce a more accurate model.

Feature Ranking: GBT measures the importance of each feature by averaging feature ranking over several trees. It provides a more stable measure of feature importance by reducing the variance of feature selection methods.

6.5 SUMMARY

The chapter presented a detailed description of the proposed framework for detecting oil spills from moving vessels from a SAR image. The proposed framework involved three main processes, including

preprocessing, linear darkspot detection and oil spill discrimination process. The preprocessing used suitable methods based on literature review. A novel segmentation-based linear darkspot detection method was proposed. The method used a combination of threshold-based and region-based algorithms to detect all possible oil slicks in a SAR image. The detected darkspot also included oil slick look-alikes. The study propose an improves discrimination process to remove the unwanted look-alikes. The discrimination process comprised of three steps. The first task was to identify commonly used features, based on literature, for oil spill detection. The second task was identifying significant features, using feature selection techniques, for the dataset. The final task is to use the identified significant features for classifying oil spills from look-alikes.

CHAPTER 7 RESULTS AND DISCUSSION

7.1 DATA DESCRIPTION

7.1.1 Real SAR data

The primary goal is to develop an automated system that detects oil spill events caused by ships (bilge dumping) using SAR data. A large number of SAR images with oil spill examples are critical in developing and evaluating an automated oil spill monitoring system. Numerous oil spill studies have been published. Oil spills in the ocean are expected to behave the same regardless of location, however, only a few studies test their methods in African oceans. The lack of studies in Africa, however, introduces a big problem as the oil spills (particularly illegal discharges) that occur in these areas are not documented. The limited studies in African areas are mainly due to inadequate data over these ocean areas. However, more data is now available with the sentinel missions [69], see Fig. 7.1. More SAR data may be available in the African coastal regions, but the lack of operational systems result in limited verified oil slick examples. For reasons mentioned above, the study covered oceans surrounding three African countries: A) Morocco, B) Mozambique and C) South Africa, as shown in Fig. 7.2.

Large swath SAR imagery has been used successfully to detect oil spill activities at sea. The study used C-band co-polarisation images for the study due to the stronger backscattering properties in oil spill studies, see section 4.3. The data consisted of historical and present data, see details in Table 7.1. The historical data had co-polarised Envisat Advanced SAR (ASAR) Wide Swath Medium (WSM) resolution images captured in South Africa's ocean from 2011 to 2012. The present data consisted of Sentinel-1 (SEN1) wide swath ground range data (GRD) with extra wide (EW) and interferometric wide (IW) modes captured in South Africa's, Mozambique's and Morocco's oceans from 2014 to 2017.

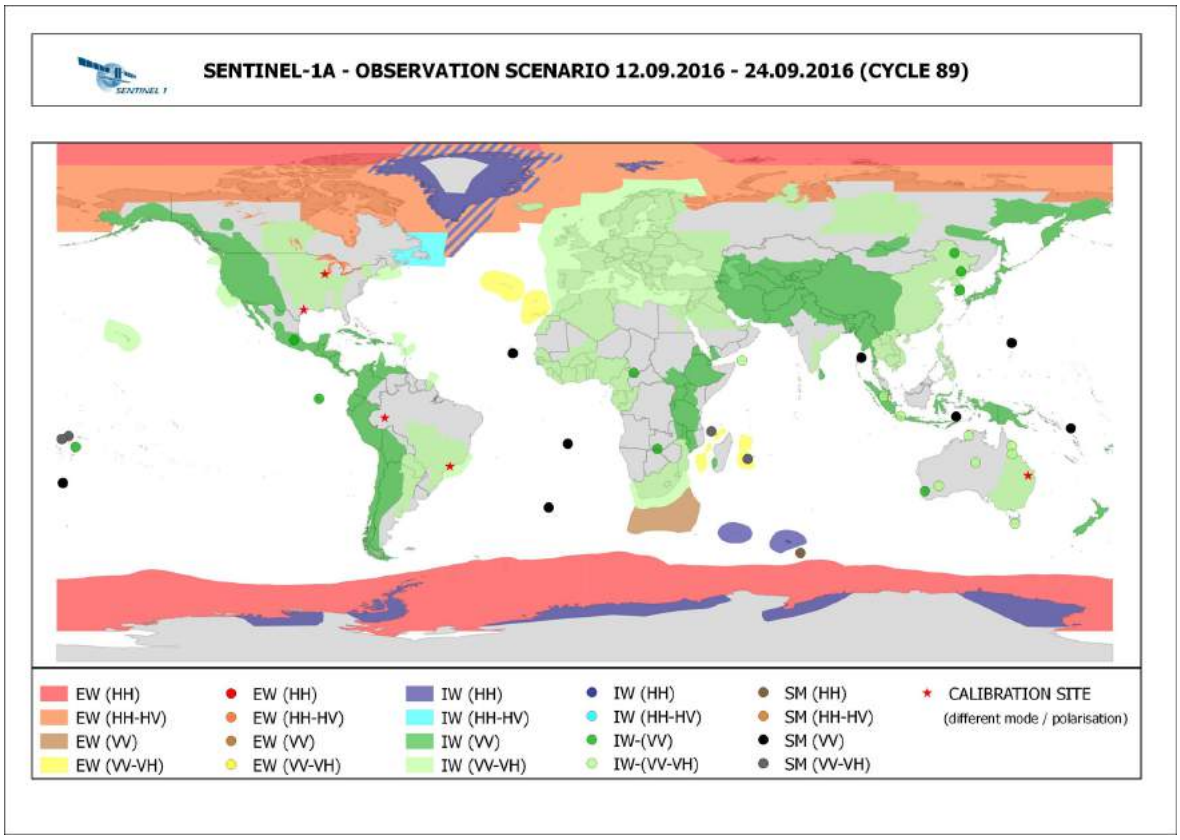

Figure 7.1. An example of the SENTINEL-1A observation scenario for September 2016. (Taken from [169], with permission).

The study also used Radarsat-2 OSVN mode image, captured on 10/10/2016 near Saint Pierre in the North Atlantic ocean, with a verified oil slick to evaluate the proposed methods outside African oceans, see descriptions in Table 7.1. Radarsat-2 (RS2) Maritime Satellite Surveillance Radar (MSSR) modes have been developed to further improve ocean surveillance [170]. The Ocean Surveillance Very-wide Near (OSVN) mode can monitor large areas, over 500 km, with a finer resolution.

Figure 7.2. A map showing the locations for the study including Morocco (marked A), Mozambique (marked B), and South Africa (marked C) coastal areas.

Table 7.1. A description of the SAR data used for testing the proposed novel oil spill detection framework

Satellite	EnviSat	RADARSAT-2	Sentinel-1A			
Product	ASAR-WSM	OSVN	EW-GRDH	EW-GRDM	IW-GRDH	IW-GRDM
Dates	2011-2012	2016	2014-2017	2014-2017	2014-2017	2014-2017
Polarisation	HH	HH	VV	VV	VV	VV
Resolution (m)	93 x 87	50 x 50	93 x 87	20 x 22	88 x 87	93 x 87
Pixel Spacing (m)	75 x 75	35 x 25	40 x 40	10 x 10	40 x 40	40 x 40
Swath (km)	400 x 400	530 x 500	400	400	250	250
No. of Images	10	1	9	6	33	42
No. of Oil Spills*	14	1	0**	12	88	0

Notes: a) All images were C-band.
b) The Radarsat image was captured on 10/10/2016 near Saint Pierre in the North Atlantic ocean.
c) The ENVISAT images were captured in South Africa's ocean only.
d) The SENTINEL images were captured in South Africa, Mozambique and Morocco's oceans.
* this number counts split oil slick, the actual number of oil spill events is lower.
** These images did not show any oil spills but contained several look-alike examples.

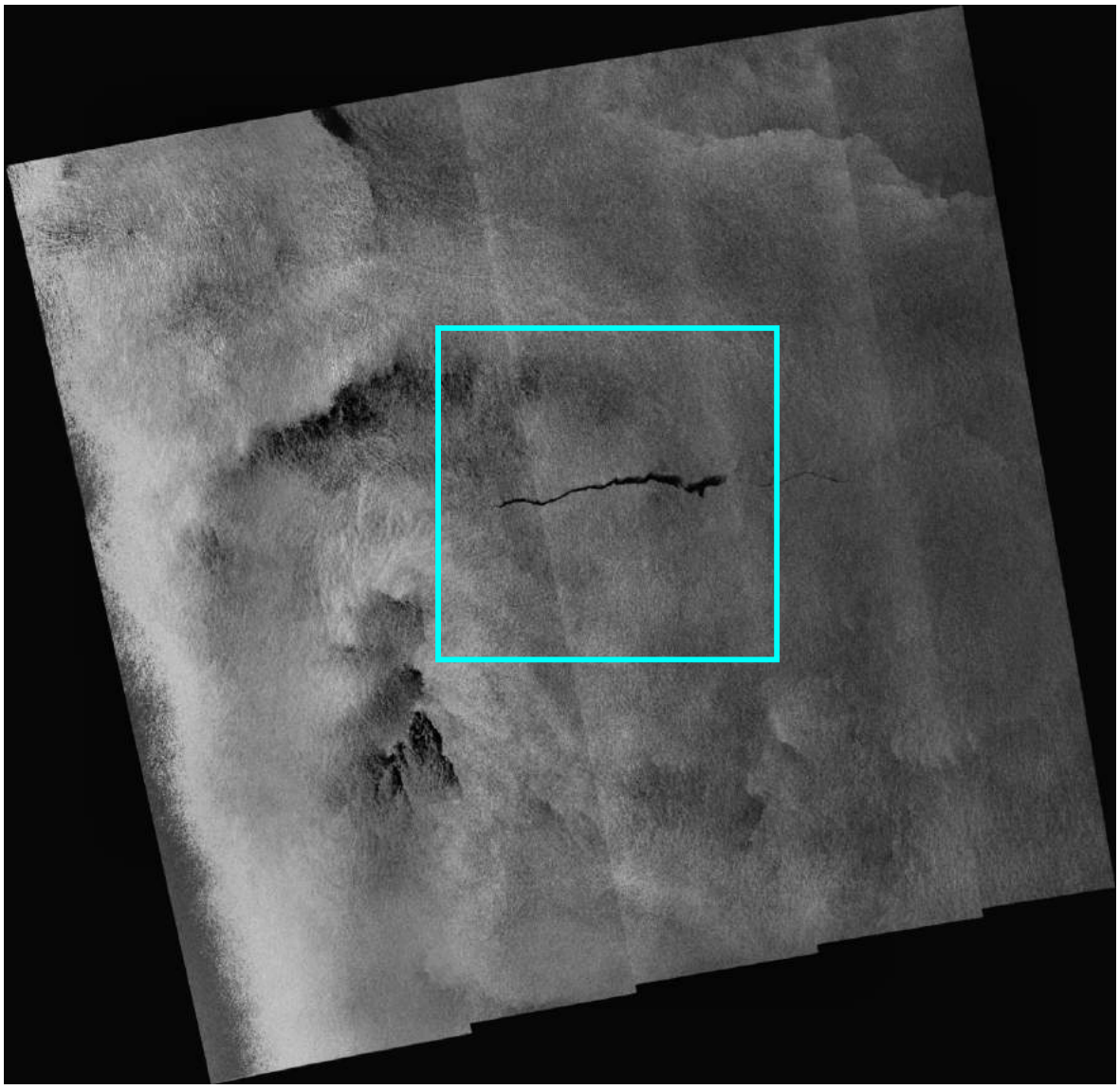

Figure 7.3. An example of the Sentinel-1A wide swath SAR image with oil spills.

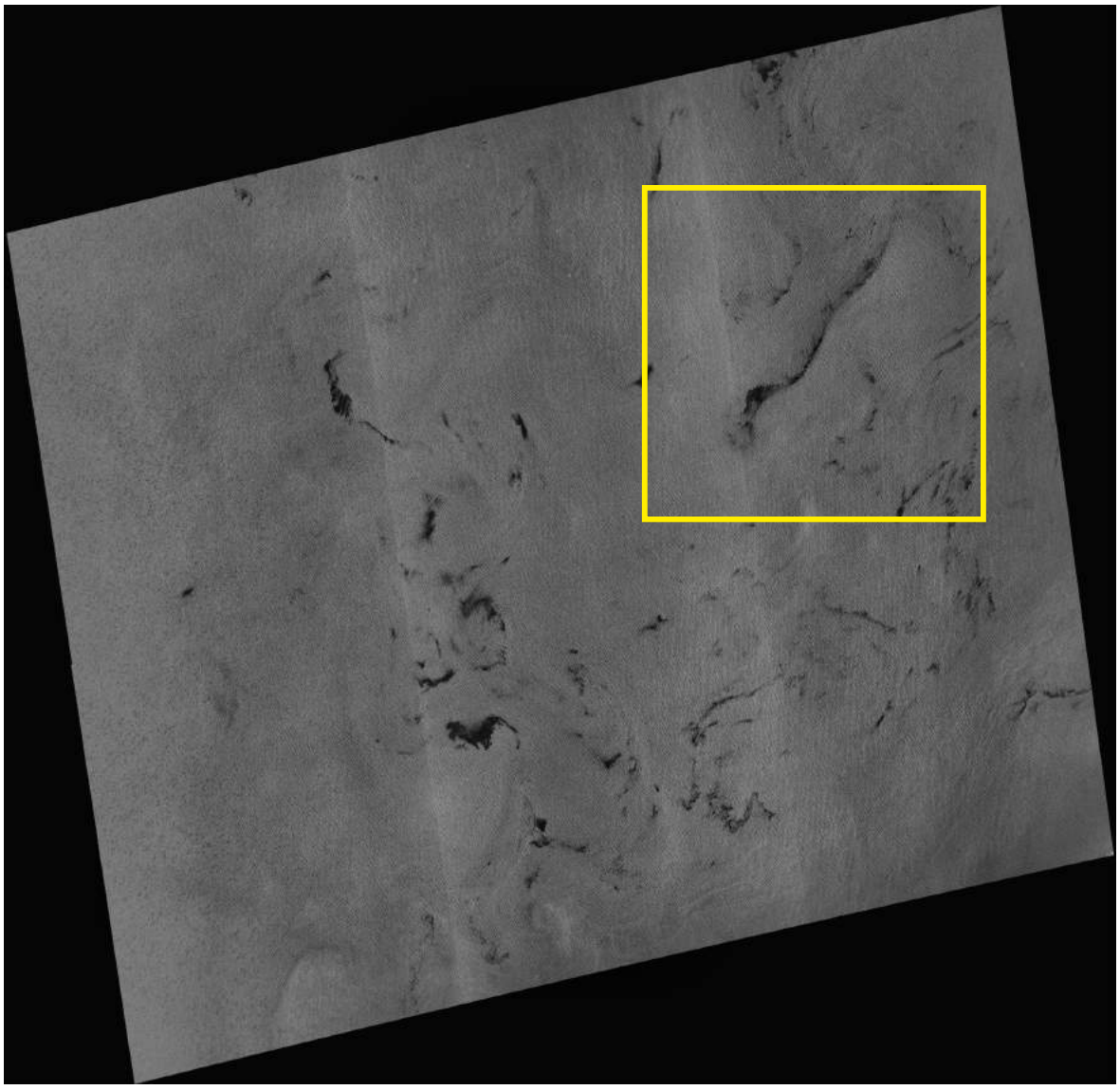

Figure 7.4. Sentinel-1A SAR images that did not have oil spills but had numerous possible look-alikes.

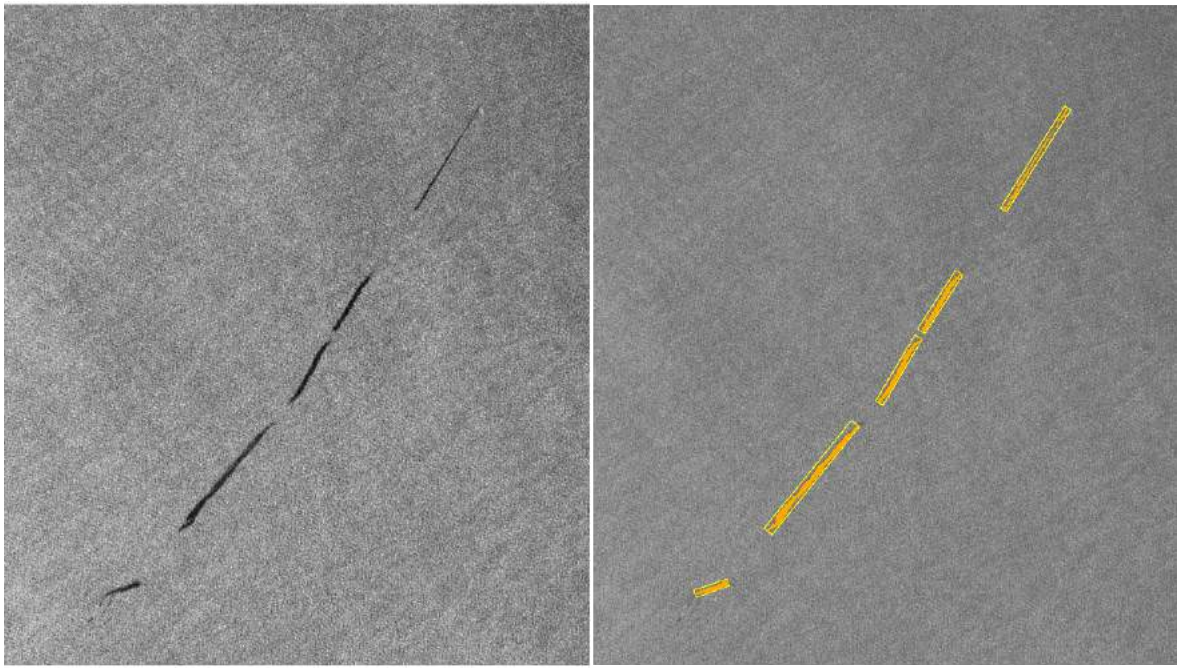

Figure 7.5. An oil spill event split in multiple parts.

An experienced operator was needed to visually validate oil slick events by taking into consideration the sea state (sea conditions, in this case, referring to wind and currents), the oil slick geometry as well as the occurrence of a vessel near the potential oil slick event, see oil spill example in Fig. 7.3. All the images had either oil spills, look-alikes or both as examples. Pixels containing oil spills were manually selected to create a mask for baseline results. The number of look-alikes was not reported in Table 7.1 because it was calculated as the number of false alarms detected by the proposed algorithms. That is, any detections that were not labelled as oil spills were counted as look-alike detections (false alarms). To test the proposed algorithms robustness, 51 Sentinel-1A SAR images that did not have oil spills but had numerous possible look-alikes were used to evaluate the robustness of the proposed discrimination process, see example in Fig. 7.4.

An oil slick database was then created from the verified oil slick events by calculating various statistics from each slick, see Table 7.2. Split oil slicks statistics were calculated individually and not summed up, such that, the total length of a long oil slick that was split to multiple parts was not used but only the length of split parts, see illustration in Fig. 7.5. The number oil slicks reported in Table 7.1 are the split oil slicks, and the number of oil spill events was fairly lower.

Table 7.2. Oil slick features database.

	Minimum	Maximum	Average	Stddev[a]
SNR[b]	-30.65	6.47	-13.28	10.13
Intensity (dB)	-27.35	-10.46	-17.61	2.28
Length (pixels)	84.01	1883.53	508.94	531.90
Width (pixels)	10.08	93.32	44.33	26.07
Length to width ratio	4.36	31.54	11.30	7.32

[a] Standard deviation.
[b] Signal to noise ratio.

7.1.2 Synthetic SAR data

The number of available oil slick examples, including historic data, was not enough to evaluate the proposed framework. Synthetic SAR data was therefore generated to test the robustness of the proposed framework. To simulate real SAR oil slicks, the synthetic SAR images were simulated according to parameters reported Table 7.2 as follows:

1. Generate a 2000×2000 image. The size was chosen based on the size of the linear darkspots features in Table 7.2.
2. Add a random linear darkspot that resembles an oil slick. The backscatter, length, width and length to width ratio values were randomly generated from minimum to maximum values reported in Table 7.2.
3. For fully developed speckles, the amplitude of the returns follow the Rayleigh distribution [71, 64, 171]. Thus the images were corrupted with Rayleigh distributed noise.

Steps 1 and 2 were repeated 200 times for each noise level to ensure nearly all possible oil slicks configurations were evaluated. The noise levels were varied high to low noise values, that is, from -36 to 12 in steps of 0.5. A total of 19200 synthetic SAR images were generated so that they were statistically similar to the actual SAR images.

Table 7.3. A two-by-two confusion matrix.

		Verified	
		Oil Spill	Look-alike
Predicted	Oil Spill	True Positive (TP)	False Positive (FP)
	Look-alike	False Negative (FN)	True Negative (TN)

7.2 EVALUATION PARAMETERS

Oil spill events from moving vessels were detected (classified) using a novel framework as presented in chapter 6. The performance of the proposed oil spill detection framework was evaluated using the receiver operating characteristics (ROC) evaluation metrics [172]. That is, given a classifier and a set of instances, a two-by-two confusion matrix (also known as error matrix) can be constructed representing the quantities of correctly classified and the errors of each class, see Table 7.3. The numbers along the major diagonal represent the correct decisions made (i.e., true detections), and the numbers of this diagonal represent the errors between the various classes (i.e., false detections). To compare the results of the algorithms analytically, reference images were manually segmented by an expert where potential oil slick darkspots were identified. The reference images were used to create ground truth data and was assumed to be 100% accurate. The study used a two class system, as illustrated in Table 7.3, where the positive class represents oil spill events and the negative class was look-alike samples. Using the ROC system, multiple accuracy and error measures were used to evaluate to the discrimination process:

- **Detection Accuracy (DA):** measured the accuracy of detected oil slick events,

$$\mathrm{DA} = \frac{\sum \text{detected oil slick events}}{\sum \text{known oil slick events}} \times 100\%, \tag{7.1}$$

  where known oil slick events were visually verified and segmented from the SAR images.

- **True Positive Rate (TPR):** measured the accuracy of correctly detected oil slick pixels. TPR was calculated as the number of detected oil spill pixels divided by the number of known oil spill pixels:

$$\text{TPR} = \frac{\sum \text{TP}}{\sum \text{TP} + \sum \text{FN}}. \tag{7.2}$$

- **True Negative Rate (TNR):** measured the accuracy of correctly classified look-alikes. TNR was calculated as the number of detected look-alikes pixels divided by the number of known look-alike pixels:

$$\text{TNR} = \frac{\sum \text{TN}}{\sum \text{TN} + \sum \text{FP}}. \tag{7.3}$$

- **False Negative Rate (FNR):** measured the missed rate of oil spill pixels. FNR is also known as the error of exclusion and was calculated as the number of incorrectly detected look-alike pixels divided by the number of known oil spill pixels:

$$\text{FNR} = \frac{\sum \text{FN}}{\sum \text{TP} + \sum \text{FN}}. \tag{7.4}$$

- **False Positive Rate (FPR):** measured the incorrectly included pixels to the oil spill class. FPR is also known as the error of inclusion or false alarm rate (FAR). It is calculated as the number of incorrectly detected oil spill pixels divided by the number of known look-alike pixels:

$$\text{FPR} = \frac{\sum \text{FP}}{\sum \text{TP} + \sum \text{FN}}. \tag{7.5}$$

7.3 LINEAR DARKSPOT DETECTION EVALUATION

Real and synthetic SAR images were used to evaluate the performance of the proposed framework and the comparison methods. For all the experiments, the input images were preprocessed as described in section 6.2. The preprocessed images were used to evaluate multiple segmentation-based algorithms.

7.3.1 Linear darkspot detection evaluation parameters

7.3.1.1 Proposed threshold-based segmentation (TSO)

TSO used the iterative Otsu segmentation **without the region-based algorithm**, as described in section 6.3.1. For each iteration, the input image was masked with the segmented image and reprocessed until there were no regions to segment or the threshold value was zero or no longer changing. An average of 5–8 iterations was observed. The threshold-based algorithm may split or oversegment darkspots and output small linear features. To ensure all linear features are detected, darkspots with length to width ratio greater than three were considered as linear darkspots. This was less than the minimum ratio from the oil slick features database in Table 7.2.

7.3.1.2 Proposed region-based segmentation (RSO)

RSO used the active contour model and level set segmentation **without the threshold algorithm input**, as described in section 6.3.2. The region-based component had two critical parameters, balloon force (α) and standard deviation (σ), that were dependent on the image. An optimal parameter search was conducted, and the algorithms were evaluated for optimal α and σ parameters.

7.3.1.3 Proposed linear darkspot detection (LDD)

LDD used a combination of threshold-based and region-based techniques to segment possible oil spills, see description in section 6.3. The region-based component was used to detect the full extent of the split or shorter linear darkspots detected from threshold-based segmentation. Only linear darkspots with a length to width ratio greater than four were labelled as potential oil slicks. These parameters were chosen according to the oil slick features database in Table 7.2.

7.3.1.4 Chaudhuri's curvilinear segmentation (CCS)

A segmentation-based algorithm proposed by Chaudhuri *et al.* [173] was considered for comparison. The authors proposed a threshold-based technique, based on the Otsu method [161], to detect dark

curvilinear features due to ocean disturbances caused by the wind, movements of surface or underwater objects and oil spills from SAR images. This made the method very comparable with the proposed threshold-based method used to segment dark linear features due to oil slick events from a moving vessel.

7.3.2 Linear darkspot detection evaluation results

The segmentation algorithms were evaluated for DA, TPR and FPR, where the results TPR and FPR were reported in Table 7.4 with the best average performance shown in bold. The results of the segmentation-based linear darkspot detection algorithms were compared and analysed.

Table 7.4. Algorithms evaluation on real SAR images.

Sub-image	TPR accuracy measure (FPR error measure) %			
	TSO[a]	**RSO**[b]	**LDD**[c]	**CCS**[d]
1	87.97 ($0 \times 10^{+00}$)	100.0 (4×10^{-02})	100.0 ($0 \times 10^{+00}$)	88.72 ($2 \times 10^{+00}$)
2	77.55 ($0 \times 10^{+00}$)	100.0 (2×10^{-01})	100.0 (3×10^{-03})	64.33 ($3 \times 10^{+00}$)
3	99.64 (5×10^{-04})	100.0 (5×10^{-02})	100.0 (2×10^{-04})	97.92 ($2 \times 10^{+00}$)
4	100.0 (4×10^{-02})	100.0 (9×10^{-02})	100.0 ($0 \times 10^{+00}$)	98.20 ($2 \times 10^{+00}$)
5	100.0 ($0 \times 10^{+00}$)	100.0 (3×10^{-01})	100.0 (3×10^{-02})	87.89 ($5 \times 10^{+00}$)
6	88.29 (4×10^{-02})	100.0 (2×10^{-01})	100.0 (7×10^{-02})	67.20 (2×10^{-01})
7	22.92 ($0 \times 10^{+00}$)	63.90 (1×10^{-01})	96.38 (6×10^{-02})	40.51 ($3 \times 10^{+00}$)
8	31.60 ($0 \times 10^{+00}$)	79.99 (2×10^{-01})	100.0 (2×10^{-02})	50.87 ($3 \times 10^{+00}$)
9	94.96 ($0 \times 10^{+00}$)	100.0 (2×10^{-01})	100.0 (4×10^{-04})	82.97 (2×10^{-01})
10	100.0 ($2 \times 10^{+00}$)	100.0 (7×10^{-01})	100.0 (9×10^{-02})	79.93 ($3 \times 10^{+00}$)
11	27.43 ($0 \times 10^{+00}$)	86.15 (4×10^{-02})	100.0 (7×10^{-02})	49.34 ($3 \times 10^{+00}$)
12	100.0 (4×10^{-01})	100.0 (1×10^{-02})	97.60 (7×10^{-03})	76.86 ($2 \times 10^{+00}$)
13	100.0 (1×10^{-01})	100.0 (5×10^{-02})	100.0 (1×10^{-02})	89.72 ($5 \times 10^{+00}$)
14	78.24 (4×10^{-01})	100.0 (2×10^{-02})	100.0 (1×10^{-02})	87.19 ($2 \times 10^{+00}$)
AVERAGE	83.58 (2×10^{-01})	95.00 (2×10^{-01})	**99.57** (**3×10^{-02}**)	75.83 ($3 \times 10^{+00}$)
STD DEV	27.29 (5×10^{-01})	10.90 (2×10^{-01})	**1.12** (**3×10^{-02}**)	18.54 ($1 \times 10^{+00}$)

[a] Proposed threshold-based segmentation only.
[b] Proposed region-based segmentation only.
[c] Proposed linear darkspot detection.
[d] Chaudhuri's curvilinear segmentation [173].

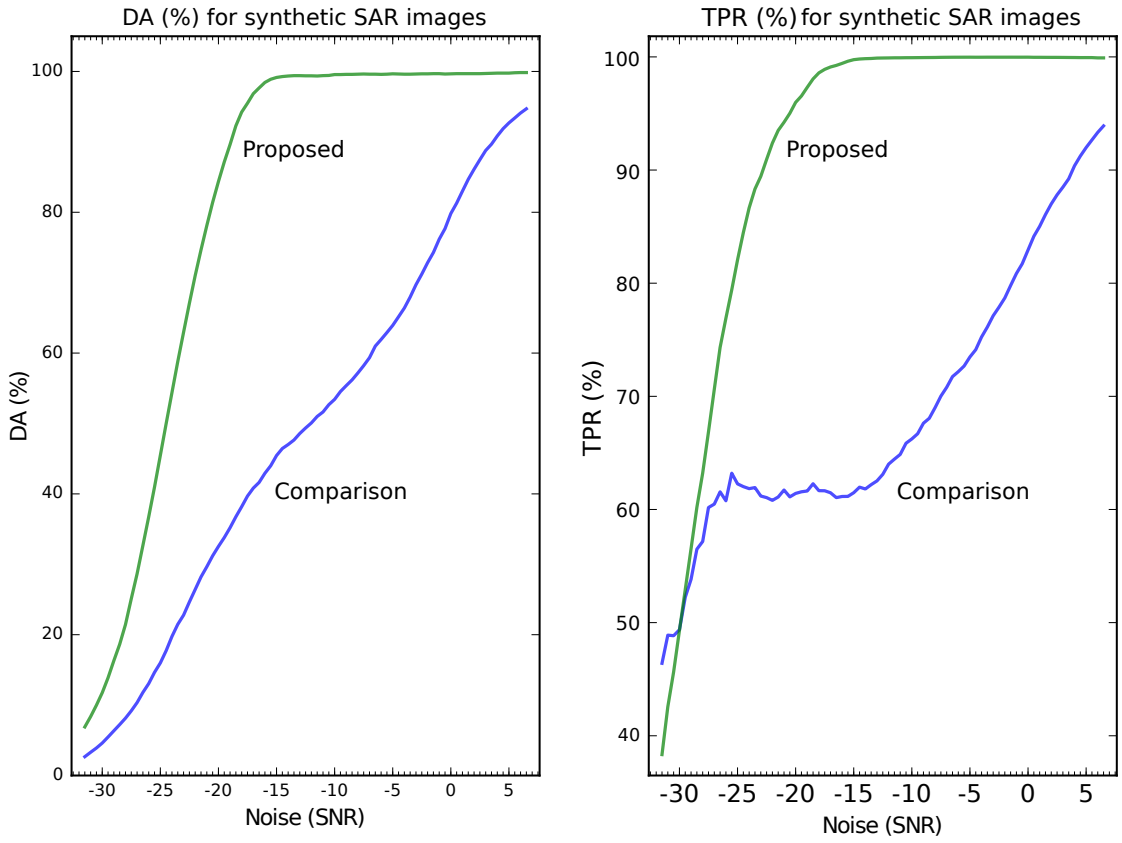

Figure 7.6. DA and TPR detections (%) plot on synthetic SAR data (SNR: -42 to 6 in steps of 0.1) using proposed threshold-based segmentation (**TSO**) (marked as "Proposed") and the comparison method proposed by Chaudhuri's curvilinear segmentation (**CCS**) [173] (marked as "Comparison").

7.3.2.1 Threshold-based methods segmentation

Both threshold-based methods (proposed threshold-based component and comparison threshold-based method by Chaudhuri *et al.* [173]) were able to detect all the oil slick events considered (i.e., DA was 100% across all images). However, the TPR and FPR results showed the proposed threshold-based method to have slightly better TPR performance (8% more) with less error (FPR) than the comparison method, see Table 7.4. The propose threshold-based algorithm showed promising results for linear darkspot segmentation.

The results of the framework are dependent on the performance of the threshold-based component, thus its effectiveness needs to be evaluated fully. The real SAR images test was unable to separate the

performance of the proposed and a threshold-based method proposed by Chaudhuri *et al.* [173]. To evaluate the robustness of the proposed threshold-based algorithm synthetic SAR data were used, see synthetic SAR details in section (7.1.2). The average DA and TPR results of the simulated images for each noise level were evaluated, see Fig. (7.6). The algorithms were not evaluated for FPR as look-alikes were not included in the simulations.

For each noise level, the proposed algorithm showed improved performance as both DA and TPR results were higher than the method by Chaudhuri *et al.* [173], see Fig. (7.6). The proposed algorithm was able to detect more oil slick events and also identified the oil slick's full extent as the noise level decreased. In contrast, the algorithm by Chaudhuri *et al.* [173] was unable to detect all the potential oil slick pixels accurately, particularly at high noise levels. The results showed the proposed threshold-based component to be sufficient in the detection of possible oil slicks, thus can be used with high confidence in the proposed framework.

7.3.2.2 Threshold-based vs region-based segmentation

The region-based algorithms showed a significant increase in TPR performance, with about 16% and 25% increase, when compared to the proposed threshold-based segmentation and Chaudhuri's curvilinear segmentation, respectively. This result is in agreement with the literature where region-based algorithms have been shown to outperform earlier efforts of threshold-based techniques [135, 132, 133, 174, 156, 175, 176], refer to section 5.3.

7.3.2.3 Proposed linear darkspot segmentation

The proposed linear darkspot detection and region-based component (without threshold input) algorithms were evaluated for the average DA performance over various (α and σ) combinations (α values from 4 – 12 in steps of 0.5 and σ values from 0.5 – 1.9 in steps of 0.1). The results showed the proposed framework results to be better across the different images where the DA was 87.76% while the comparison algorithm only achieved 54.46%. This result showed that the proposed framework was less dependent on (α and σ) parameters and a better algorithm overall.

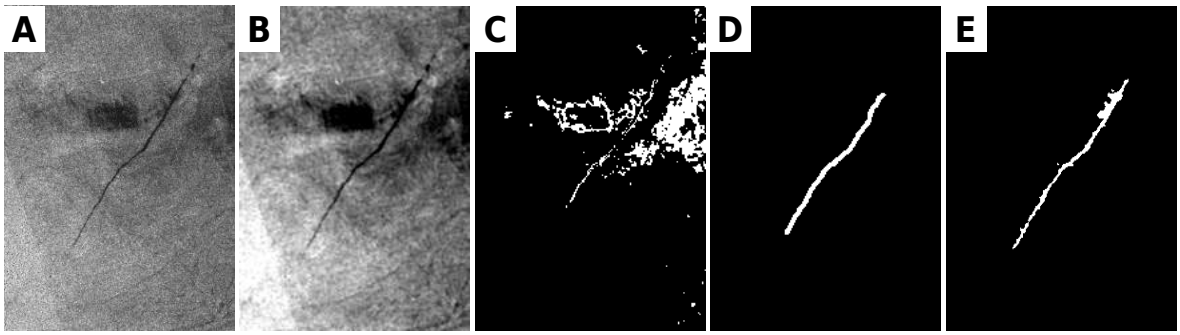

Figure 7.7. Linear darkspot and full extent extraction results. A) Envisat SAR image with oil spill (captured on 2007, Durban, South Africa); B) Image after preprocessing; C) Darkspots as potential oil slicks; D) Extracted linear darkspots; E) Final Linear Darkspot Detection.

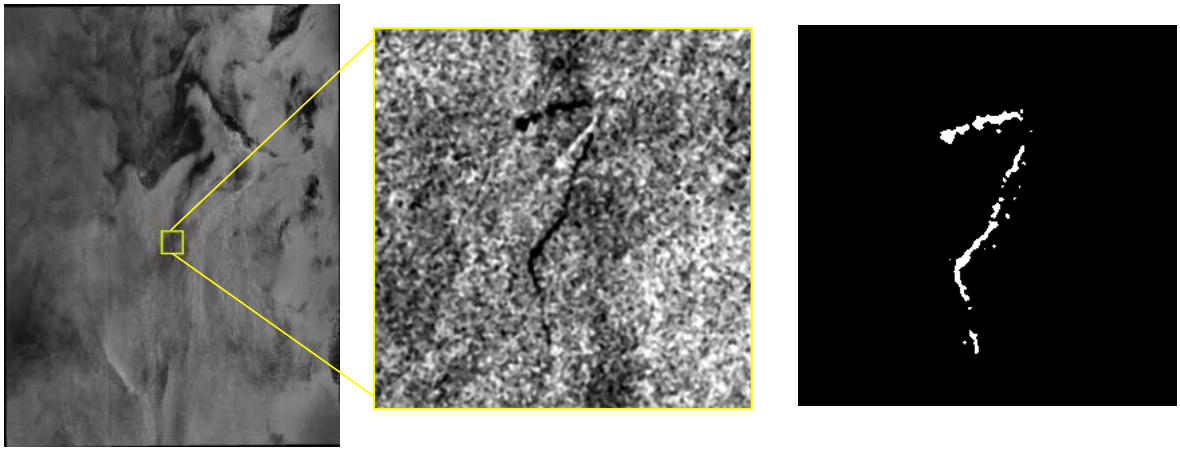

Figure 7.8. Proposed framework's experimental results for Radasat SAR image. Left: Large SAR image that covers more than 500km swath; Middle: A verified oil spill; Right: Oil spill segmentation result using proposed Linear Darkspot Detection algorithm.

Figs. 7.9, 7.7, 7.8, shows real SAR images' final segmentation output of potential oil slick events using the proposed linear darkspot detection algorithm. The proposed linear darkspot detection method worked well in detecting oil slicks from real SAR images. However, two of the sub-images showed TPR values less than 100% (the proposed method did not detect the full extent of the oil slicks), see Table 7.4. These images had multiple oil slicks from the same source, see example in Fig. (7.9, right most sub-image). Segments that were large enough were successfully detected while shorter slicks were discarded in the linear darkspot extraction process as they did not meet the minimum length or length to width ratio criterion.

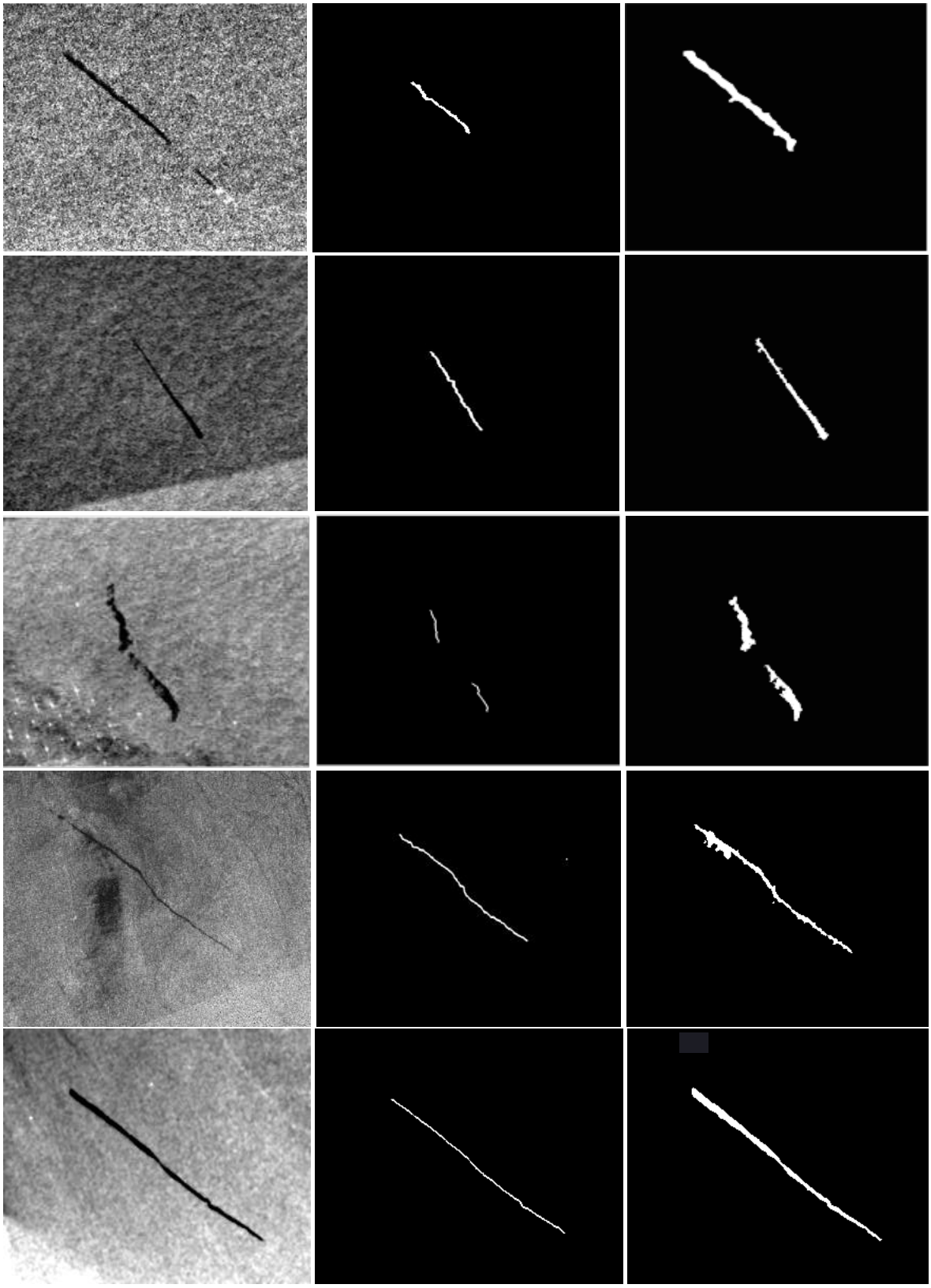

Figure 7.9. Proposed framework experimental results for Envisat (rows 1 and 2) and Sentinel (rows 3 to 5) SAR images. left column: Regions with potential oil slicks. Middle column: Threshold-based initial contours. Third column: Linear darkspot detections.

7.3.2.4 Proposed linear darkspot segmentation computation cost

The region-based algorithm used an active contour model and level sets algorithm that used an initial contour as input. The LDD algorithm used the output from the proposed threshold-based segmentation as the initial contours. The study investigates the computation performance cost of using the LDD algorithm over the standard region-based methods (with arbitrary initial contour).

The computation performance was measured by calculating the number of iterations (contour evolutions) needed by each region-based algorithm to detect the full extent (TPR) of a potential oil slick. An initial contour based on the proposed framework versus a rectangular initial contour (placed at the centre of an oil slick event in an image) was used to detect the full extent of potential oil slick events. The experiments (using optimal parameters) calculated the number of contour evolutions/iterations needed to detect all the oil slick pixels in a synthetic image with noise (SNR = 0). The results showed that the proposed framework was able to detect all the pixels of the region of interest with significantly fewer iterations (less than 100 iterations), see Fig. 7.10. In contrast, the region-based algorithm with rectangle shaped initial contour could not detect all the pixels after 400 iterations. The less iteration showed that the proposed framework was more efficient in computation performance than using the region-based algorithm with an arbitrary initial contour. Fig. 7.11 shows the number of iterations (contour evolutions) needed to detect the full extent using a real SAR image.

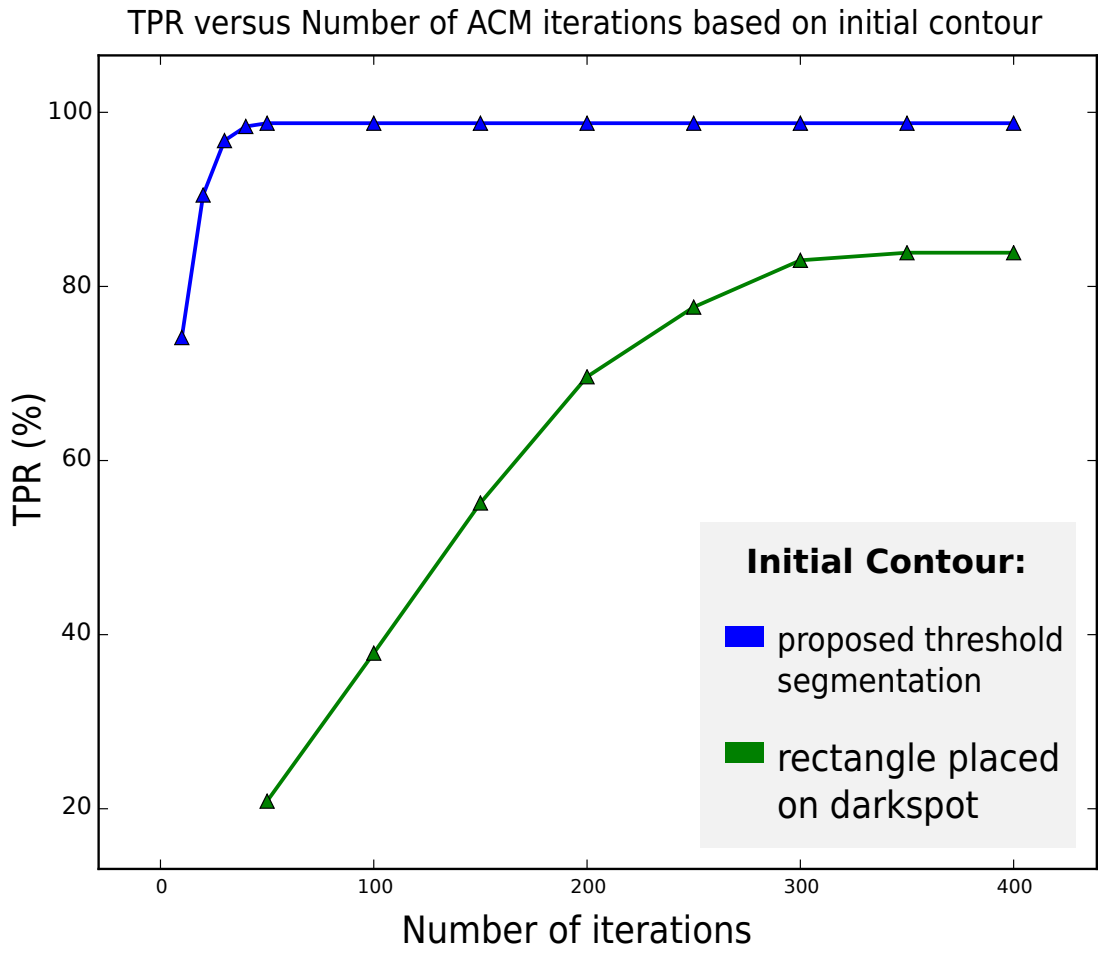

Figure 7.10. Oil spill detection rate for proposed (threshold segmentation as ACM input) initial contour versus generic rectangle initial contour using optimal parameters on a synthetic SAR image.

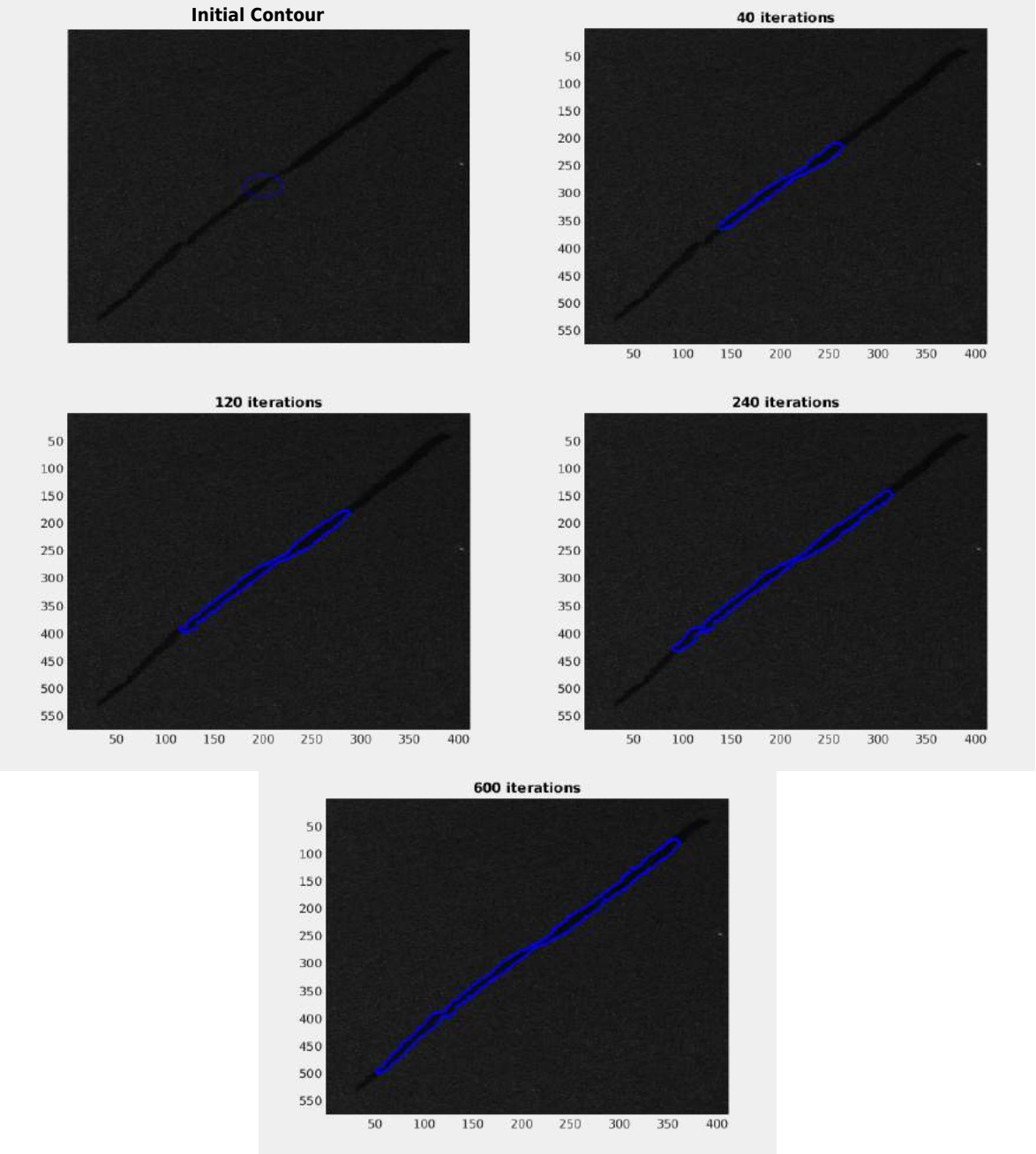

Figure 7.11. Region-based darkspot segmentation from a SAR image using a circle as initial contour.

7.4 OIL SPILL DISCRIMINATION EVALUATION

The highest possible detection accuracy is essential. The proposed novel segmentation-based Linear Darkspot Detection algorithm was demonstrated to be successful. However, the method did not separate look-alike from real oil spill events, see section 7.3. Verification of an oil spill can be costly and time-consuming. Therefore, the study proposed an oil spill discrimination process that will reduce the number of false detections (i.e., look-alike detections) from a segmentation algorithm. The improved discrimination process was accomplished using three steps. Firstly, the study identified the frequently used features in literature. Secondly, the study determined significant features using proposed Africa dataset and ranked them by significance. Lastly, the study distinguished possible oil spills from look-alikes using the selected features, see section 6.4.

7.4.1 Discrimination process data

The input dataset comprised all the linear darkspot detections, as discussed in section 6.3. The images were in binary format, that is, darkspots had a pixel value of 1 and the surroundings had a pixel value of 0, see example in Fig. 7.9. The binary image was used to extract geometric features. The dataset also included the calibrated NRCS (dB) images to calculate texture and physical features, please refer to the experiment flowchart in Fig. 6.1. Using the detected linear darkspots, the dataset was separated into two classes: oil slicks and look-alikes. The oil spill darkspots were visually verified by an expert and look-alikes were all the non-verified darkspots. Sentinel (EW and IW) imagery was used to evaluate the discrimination process. The data had a total of 149 look-alike samples and 100 oil spill samples. All considered features were extracted from the detected linear darkspots and a limited area outside the darkspot (oil spill free area), see example in Fig. 7.12.

7.4.2 Feature significance and ranking evaluation

The commonly used oil spill features in literature were investigated and found that the studies often did not use the same number of features. The disparity in the number of features was because the features were not of equal significance. That is, a particular feature may be critical in one study but removing the same feature improves the results of another study. The study determined significant features according to previous studies and feature selection methods using study dataset. However, the

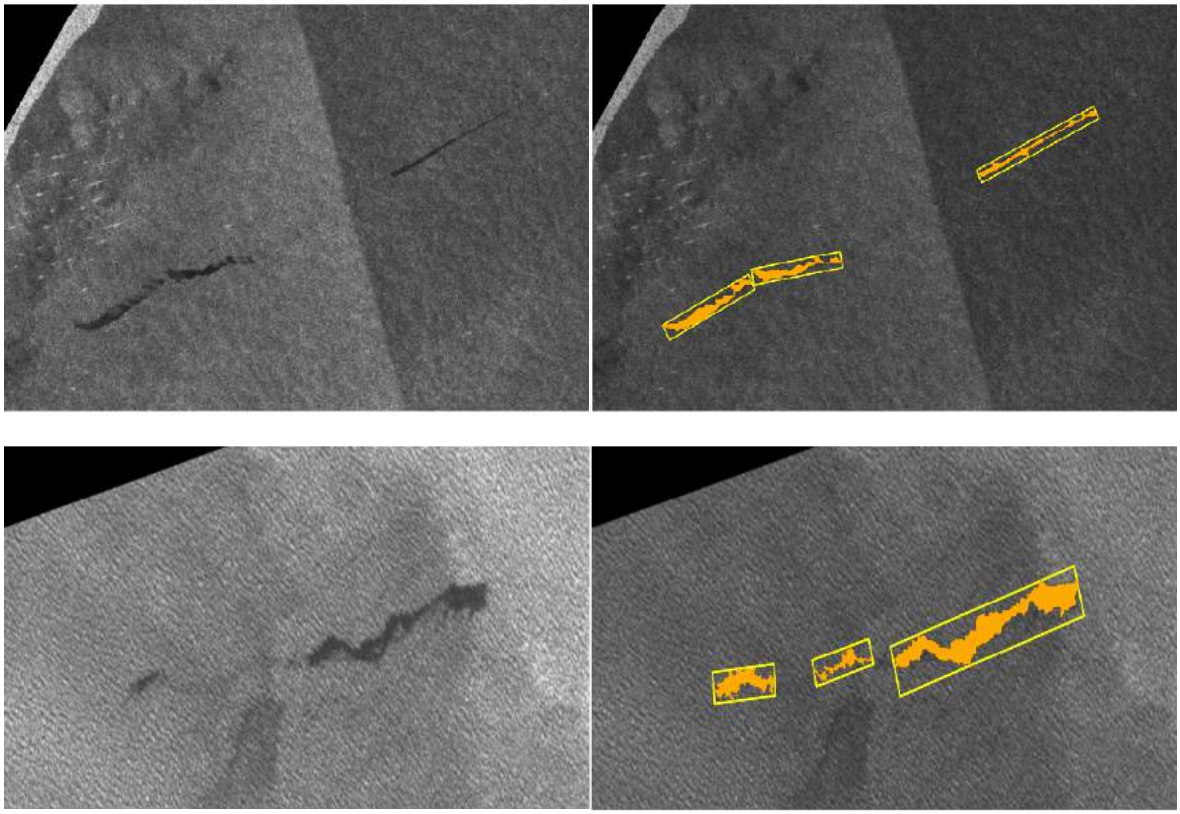

Figure 7.12. SAR subimages showing the darkspot and limited area (shown in yellow) used to extract physical features.

features were not of equal significance, each set of significant features had a different ranking. The study measured feature rankings based on how significant each feature was compared to other features in a given feature set, as described in section 6.4.2.2. All the measurements were normalised and divided into very low, low, medium and high feature significance and feature ranking, see Tables 7.5 and 7.6.

Table 7.5. Comparison of feature significance and feature rankings measured from literature and proposed feature selection methods.

	Description	Code	Feature Significance[a]		Feature Ranking[a]	
			Literature[b]	Study	Literature	Study
Geometry Features:						
1	Area	A	○	○	○	○
2	Perimeter	P	○○	•••	○○	○○
3	Perimeter to Area ratio	P/A	○○	○○	○○	○○
4	Complexity	C	•••	○○	○○	•••
5	Shape Factor 1	SP1	○○	••••	•••	•••
6	Shape Factor 2	SP2	••••	••••	••••	••••
Texture Features:						
7	Spectral texture	Tsp	○	○	○	○
8	Shape Texture	TSh	○	○	○	○
9	Mean Haralick Texture	THm	○○	○○	○○	•••

[a] Measure symbols: Very low (○), Low (○○), Medium (•••), High (••••).

[b] Literates studies: [141, 146, 16, 136, 177, 138, 148, 130, 142, 17].

Table 7.6. Comparison of feature significance and feature rankings measured from literature and proposed feature selection methods.

	Description	Code	Feature Significance[a]		Feature Ranking[a]	
			Literature[b]	Study	Literature	Study
Physical Features:						
10	Object Mean	OMe	•••	••••	○○	•••
11	Background Mean	BMe	•••	••••	•••	•••
12	Object Standard Deviation	OSd	••••	•••	••••	••••
13	Background Standard Deviation	BSd	••••	•••	••••	••••
14	Object Power to Mean Ratio	Opm	••••	•••	••••	••••
15	Background Power to Mean Ratio	Bpm	••••	•••	••••	•••
16	Ratio of Standard Deviation	RaSd	•••	○○	•••	••••
17	Ratio of Means	RaMe	○○	••••	•••	•••
18	Ratio of Power to Mean Ratios	Opm/Bpm	•••	○○	•••	•••
19	Max Contrast	ConMax	○	○	○	○
20	Mean Contrast	ConMean	○	○	○○	○○
21	Mean Contrast Ratio	ConRaMe	○○	○	○	○
22	Standard Deviation Contrast Ratio	ConRaSd	○○	○	○	○
23	Local Area Contrast Ratio	ConLa	•••	••••	•••	••••
24	Mean Border Gradient	GMe	•••	○○	••••	•••
25	Standard Deviation Border Gradient	GSd	•••	••••	••••	••••
26	Max Border Gradient	Gmax	○○	○	○○	○○
27	Min Border Gradient	Gmin	○	○	○	○
28	Power to Mean Border Gradient	Gpm	○○	○	○○	○○
29	Mean Difference to Neighbours	Ndm	○○	○	○	○

[a] Measure symbols: Very low (○), Low (○○), Medium (•••), High (••••).

[b] Literates studies: [141, 146, 16, 136, 177, 138, 148, 130, 142, 17].

7.4.2.1 Literature feature significance and ranking

Numerous studies have presented essential features using SAR, these features vary in importance and rankings. An average ranking of each feature was determined based on previous studies in literature [141, 146, 16, 136, 177, 138, 148, 130, 142, 17], see Tables 7.5 and 7.6. The study measured how often features were selected as significant to determine a general feature set of significant features based on the literature studies. A total of 29 features were considered based on Table 5.1. From the literature studies, 13 features were found with medium significance while 5 features had high significance in oil spill discrimination, see Tables 7.5 and 7.6. The literature feature rankings showed that 7 of the 29 standard features were of high rank, these include *SP2, OSd, BSd, Opm, Bpm, GMe* and *GSd* features.

7.4.2.2 Proposed study feature significance and ranking

A feature significance measure was done using the study dataset and ANOVA and RFE feature selection methods, see descriptions in section 6.4.2. From the study, 12 features were found with medium significance while 7 features had high significance in oil spill discrimination, see Tables 7.5 and 7.6. Gradient boosted tree (GBT) was used to measure feature rankings for all significant features (very low to high significance). GBT can reduce the variance of feature selection methods by averaging them over several trees and was thus considered a reliable measure. The study feature rankings showed that 5 of the 29 standard features were of high rank, these include *SP2, OSd, BSd, Opm, Conla* and *GSd* features.

7.4.3 Oil spill classification evaluation

A supervised GBT classifier with optimised parameters was used to distinguish oil spills from look-alikes from the selected features. A k-fold cross-validation method ($k = 5$) was used to split training and testing set and to evaluate the overall classification accuracy of each feature set considered. To measure how well a classifier was able to distinguish between two or more classes, the area under the ROC curve (AUC) was also calculated. The AUC was calculated for the 5 ROC curves and then averaged, giving an estimate of the true area and an estimate of its standard error, calculated from the standard deviation of the 5 areas. This was done using different number of features as input, see

Table 7.7. Cross-validation Accuracy Scores.

Feature Selection	No. of Features	Mean Acc[a] (+/- Std[b])	Min	Max	TPR[c]	TNR[d]
GBT*	All	77.4 (13.8)	61.9	98.4	78	63
GBT**	6	91.6 (6.36)	82.5	99.2	84	80
	9	93.9 (5.02)	87.7	99.6	81	80
	15	85.7 (11.3)	70.2	100	79	76
RFE	6	83.1 (7.37)	72.6	95.2	77	70
	9	81.0 (9.95)	69.4	96.4	74	60
	15	75.8 (11.53)	64.5	95.6	77	63
ANOVA	4	87.8 (9.89)	75.0	99.6	84	77
	9	87.1 (7.58)	72.2	92.9	81	66
	15	83.6 (12.3)	69.4	99.2	78	67

[a]Mean Accuracy Score.
[b]Standard Deviation.
[c]True Positive Rate.
[d]True Negative Rate.

section 6.4.2.1, where the true detection rates for both oil spill and look-alikes was evaluated. The mean, standard deviation, minimum and maximum classification accuracy score were also evaluated and the number of features that had the most significant changes in the mean classification accuracy score are reported in Table 7.7.

GBT*: All the 29 features were used as input and were evaluated with the GBT classifier. The GBT* without any feature optimisation showed the lowest accuracy (77.4%).

GBT:** The ranked significant features found in the study (please refer to Tables 7.5 and 7.6) were used as input using the FFS method and evaluated with the GBT classifier. Starting with the most significant feature based on the feature ranking, features were sequentially added to a feature set and then re-evaluated. For each feature added, a classification (GBT**) accuracy was determined and the smallest feature set with the highest accuracy was 93.9% with nine features.

RFE: Significant features that were in RFE results were evaluated with the GBT classifier. The least important features were sequentially removed, and features that remained were evaluated. For each feature removed, a classification accuracy was determined and the smallest feature set with

the highest accuracy was 83.1% with nine features.

ANOVA: Significant features that were in ANOVA results were evaluated with the GBT classifier. Input features were then ranked statistically according to their significance using F-test. The least important features were sequentially removed, and features that remained were evaluated with GBT classifier. For each feature removed a classification accuracy was determined and the smallest feature set with the highest accuracy was 87.8% using six features.

7.5 SUMMARY

An oil spill detection framework that focused on the task of detecting oil from moving vessels using SAR imagery was proposed and evaluated. The proposed framework consists of three main steps, that is, the preprocessing, the linear darkspot detection, and the oil spill discrimination, see flowchart in Fig. 6.1. The framework used a novel linear darkspot detection and an improved discrimination process.

The linear detection process used a segmentation-based algorithm to isolate linear darkspots from other features in the image, see illustration in Fig. 7.13. The proposed linear darkspot algorithm also aimed to solve both the threshold-based and region-based algorithm limitations by combining them to form a more efficient framework. Threshold-based algorithms are limited by choice of a threshold value, which can result in split oil slicks or partial detection of the oil slick extent. Region-based algorithms overcome the latter by detecting the full size of the split or partially detected potential oil slick. The region-based algorithm may be superior in identifying the full extent of oil slicks, but it was not ideal for large SAR images due to its high computation cost. Using the threshold-based algorithm results as input to the region-based method improved the ACM contour initialisation problem and the computation performance. The proposed framework used a threshold-based algorithm to quickly scan for areas with potential bilge events and only used the region-based algorithm to detect the full extent of oil slicks from those regions. The proposed framework was tested on both real SAR and synthetic SAR images and was robust to intensity variations, weak boundaries and was also more computationally efficient when compared to the region-based method without the threshold-based input. The threshold component significantly reduced computation time while the region-based component improves the final segmentation result. The proposed segmentation framework showed to be more efficient when compared to each component (i.e., the threshold-based and region-based framework components) and

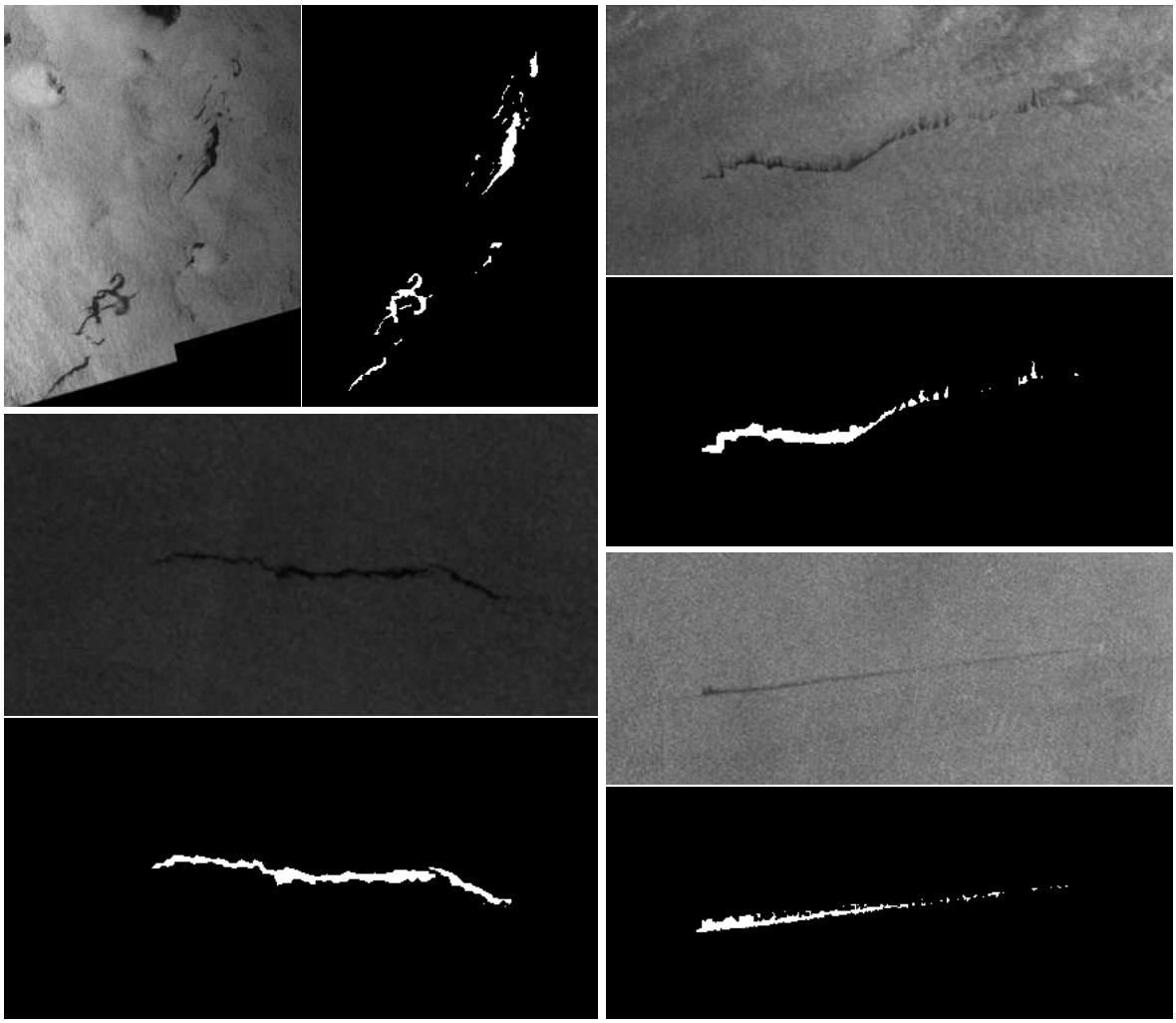

Figure 7.13. SAR subimages with segmented linear darkspots image (binary images).

the method by Chaudhuri et al. [173] in oil slick detection from SAR images. The proposed linear darkspot detection method worked well in detecting oil slicks from real SAR images, with the highest true positive rate of 99.6% and lowest standard deviation of 1.1%.

The proposed linear darkspot algorithm was successfully demonstrated, however, had a high number of false detection (look-alike detections). The results were further improved upon by using a discrimination process that identified the most relevant oil spill features for separating oil spills and look-alikes. Oil spill feature selection depends on many factors which could influence which features were extracted and selected for the classification task. In this study, we classified oil spill events from moving vessels, and the most important features were determined. The classification task used an optimised Gradient Boosting Tree Classifier (GBT). The most important features were determined

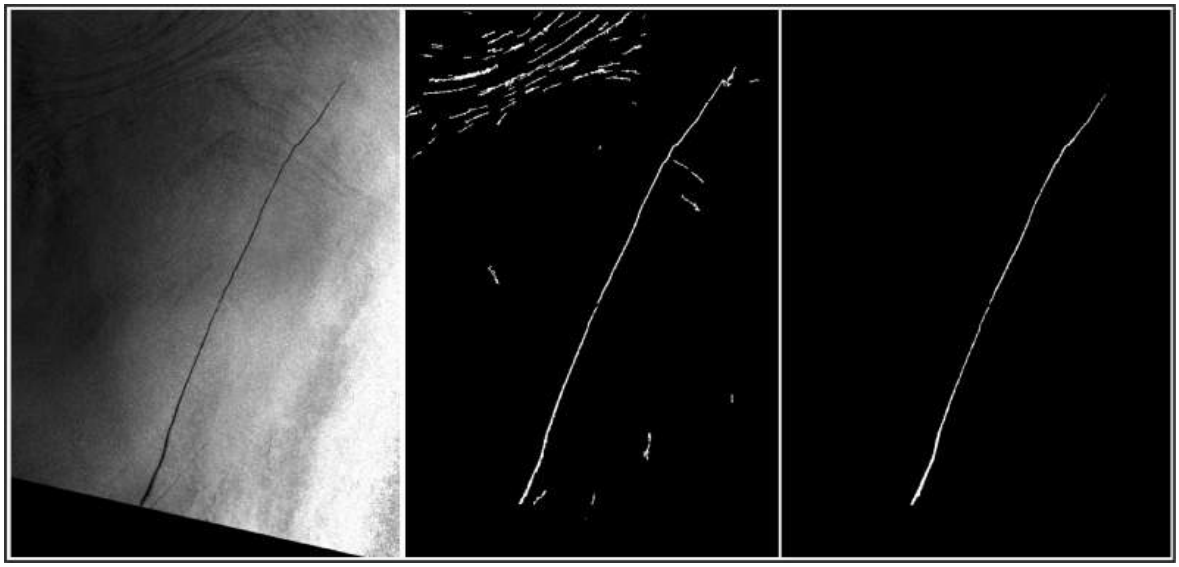

Figure 7.14. Input image (left), segmented linear darkspots image (middle) and final discrimination image (right).

using multiple feature selection methods, including ANOVA and RFE. The study also used significant features from various literature studies. The results showed that using all available features is not the most efficient way to distinguish oil spills from look-alikes. Only half of the commonly used features was needed for acceptable results. The study ranked critical features with a high selection frequency and less critical features in high accuracy discrimination tasks. Using a feature selection step showed the notable improvement in the results, from 77% to 94% on average classification score. Seven features were determined as the most important with five being consistent across methods and two being less consistent. The five features included one geometry feature based on object shape (*SP2*), the rest were physical features (*OSd, BSd, Opm, GSd*) and no texture features. The shape factor (*SP2*) was measured as the general shape of the object. The *OSd* and *BSd* measured the standard deviation of the intensity values of the pixels belonging to the object and background. The object power to mean ratio (*Opm*) measured the ratio between the standard deviation (*OSd*) and the mean (*OMe*) values of the object. The last significant feature, standard deviation border gradient (GSd) measured the backscatter values spreading of the border gradient of the object. The results showed that significant feature can determined across literature and the proposed study with minimum variation. The identified features and the discrimination process was showed successful in classifying oil spills and look-alikes, as shown in Fig. 7.14.

CHAPTER 8 CONCLUSION

8.1 FINAL REMARKS

An oil spill is a form of pollution that is due to the intentional or unintentional release of oil to the ocean environment. Ship accidents and illegal operational discharges are the prominent sources of maritime oil pollution. Oil spill events often result in severe environmental costs and pose significant threats to wildlife, human beings, and the natural ecological system. The impact of oil spills on the coastal environment depends heavily upon the type, viscosity, toxicity, amount, as well as to the sensitivity of the local organisms and the length of exposure. The law requires the retrieval of oily bilge wastewater to be in the harbours. However, ships find an economic advantage in illegally discharging bilge waste. Operational discharges of oil from vessels, whether accidental or deliberate, is a growing concern as the levels of maritime traffic increase. Oil tankers and other kinds of ships are among the suspected offenders of illegal discharges. The international legislation contains minor and well-defined exceptions related to ocean areas (internal waters, marine protected areas, MARPOL "special" areas, territorial seas or exclusive economic zones). These areas often determine whether an action is considered legal or not, and define the rights and obligations, including law enforcement obligations.

The study focused on the task of detecting oil spills from moving vessels using only the most critical features derived from a SAR image. A novel oil spill detection framework from SAR imagery was proposed. The framework used a novel linear darkspot detection algorithm and an improved oil spill discrimination process. The linear detection process used a segmentation-based algorithm to isolate linear darkspots (potential oil spills) from other features in the image. The process involved a more efficient feature selection and classification process. The results demonstrated the proposed linear darkspot segmentation approach to be robust to intensity variations, weak boundaries and more efficient when compared to the state-the-art segmentation methods.

To reduce false alarms from the segmentation-based algorithm, the study further improved upon the segmentation results by improving the discrimination process. Oil spill feature selection depends on many factors which could influence which features are used for the classification task. The improved discrimination process identified the significant feature that would yield the highest classification accuracy. Consistently high valued features include shape description, the object and background standard deviation measure, the ratio object standard deviation and mean values and the object border standard deviation. The less essential features include contrast, area and texture features. Using relevant features, the study showed an improved segmentation-based linear darkspot detection and an improved discrimination process that achieved a mean classification score above 90%.

8.2 FUTURE WORK

Future work includes developing an alert system will detect potential oil spill events and classify them according to confidence and alert levels. Feature selection and classification of oil spill events from look-alikes using only SAR data can be a difficult task. Therefore, the alert system will incorporate contextual information such as oil spill source. The confidence levels will describe the quality of the detected oil spill (based on the probability measures of the observed darkspot feature). The alert level will describe the risk of the oil spill based on contextual information and confidence level. The system will also automatically extract contextual features such as ship/platform locations, ship traffic lane information and the position of environmentally sensitive areas. More SAR data will be analysed by expanding the study area.

8.3 RESEARCH CONTRIBUTIONS

Manuscript ready for submission:

Authors: L. W. Mdakane and W. Kleynhans

Title: Improved oil spill discrimination using wide-swath SAR data in African oceans.

Journal: Remote Sensing Journal

Year: 2018

Accepted articles:

1. L. W. Mdakane, W. Kleynhans and C. P. Schwegmann, "Bilge dump detection from SAR imagery using local binary patterns," in *International Geoscience and Remote Sensing Symposium (IGARSS)*. IEEE, 2015, pp. 357–360.
2. L.W. Mdakane, W. Kleynhans and C. P. Schwegmann, "Using an active contour method to detect bilge dumps from SAR imagery," in *International Geoscience and Remote Sensing Symposium (IGARSS)*, IEEE, 2016, pp. 5015–5018.
3. L.W Mdakane, W. Kleynhans, C. P. Schwegmann and R. G. Meyer, "Image segmentation-based oil slick detection using SAR Radarsat-2 OSVN maritime data," in *International Geoscience and Remote Sensing Symposium (IGARSS)*, IEEE, 2017, pp. 3113–3116.
4. L. W. Mdakane and W. Kleynhans, "An image-segmentation-based framework to detect oil slicks from moving vessels in the Southern African oceans using SAR imagery," IEEE Journal of Selected Topics in Applied Earth Observations and Remote Sensing, 2017.

REFERENCES

[1] M. N. Jha, J. Levy, and Y. Gao, "Advances in remote sensing for oil spill disaster management: state-of-the-art sensors technology for oil spill surveillance," *Sensors*, vol. 8, no. 1, pp. 236–255, 2008.

[2] D. Tang, J. Gower, G. Levy, K. Katsaros, M. Heron, and R. Singh, *Remote Sensing of the changing Oceans*. Springer, 2011.

[3] M. Migliaccio and M. Tranfaglia, "Oil spill observation by SAR: a review," in *USA-Baltic Internation Symposium, 2004*. IEEE, 2004, pp. 1–6.

[4] M. Gianinetto, P. Maianti, R. Tortini, F. Rota Nodari, and G. Lechi, "Evaluation of modis data for mapping oil slicks - the deepwater horizon oil spill case," in *Geographic Technologies applied to Marine Spatial Planning and Integrated Coastal Zone Management*. Universidade Dos Açores, 2010, pp. 61–67.

[5] Office of Response and Restoration, National Ocean Service, National Oceanic and Atmospheric Administration (NOAA). http://photos.orr.noaa.gov/Photos/. Accessed: 2018-03-20.

[6] M. F. Gauthier, L. Weir, Z. Ou, M. Arkett, and R. De Abreu, "Integrated satellite tracking of pollution: A new operational program," *International Geoscience and Remote Sensing Symposium (IGARSS)*, pp. 967–970, 2007.

[7] A. H. S. Solberg, "Remote sensing of ocean oil-spill pollution," *Proc. of the IEEE*, vol. 100, no. 10, pp. 2931–2945, 2012.

[8] J. Burger, *Oil spills. New Brunswick*. NJ: Rutgers University Press, 1997.

[9] P. R. Epstein, J. Selber, S. Borasin, S. Foster, K. Jobarteh, N. Link, J. Miranda, E. Pomeranse, J. Rabke-Verani, D. Reyes *et al.*, "A life cycle analysis of its health and environmental impacts," *The Center for Health and the Global Environment. Harvard Medial School. EUA*, 2002.

[10] International Tanker Owners Pollution Federation (ITOPF). http://www.itopf.com/knowledge-resources/library/image-library/image/. Accessed: 2018-03-20.

[11] European Maritime Safety Agency (EMSA). (2013) Addressing illegal discharges in the marine environment. http://www.emsa.europa.eu/emsa-documents/latest/77-publications/1879-addressing-illegal-discharges-in-the-marine-environment.html. Accessed: 2017-08-15.

[12] M. Fingas, *The basics of oil spill cleanup*. CRC press, 2012.

[13] R. B. Clark, C. Frid, M. Attrill *et al.*, *Marine pollution*. Clarendon Press Oxford, 1989, vol. 4.

[14] Office of Response and Restoration, National Oceanic and Atmospheric Administration (NOAA). https://response.restoration.noaa.gov/download/file/fid/5852. Accessed: 2018-03-20.

[15] F. Nunziata, A. Gambardella, and M. Migliaccio, "On the degree of polarization for SAR sea oil slick observation," *ISPRS Journal of Photogrammetry and Remote Sensing*, vol. 78, pp. 41–49, 2013.

[16] A. H. S. Solberg, G. Storvik, R. Solberg, and E. Volden, "Automatic detection of oil spills in ERS SAR images," *IEEE Transactions on Geoscience and Remote Sensing*, vol. 37, no. 4, pp. 1916–1924, 1999.

[17] C. Brekke and A. H. S. Solberg, "Oil spill detection by satellite remote sensing," *Remote Sensing of Environment*, vol. 95, no. 1, pp. 1–13, 2005.

[18] A. Lewis and F. Henderson, *Manual of Remote Sensing, Principles and Applications of Imaging Radar*. Wiley & Sons, NY, 1998.

[19] J. C. Curlander and R. N. McDonough, *Synthetic Aperture Radar Systems and Signal Processing*. John Wiley & Sons New York, NY, USA, 1991, vol. 396.

[20] K. Tomiyasu, "Tutorial review of synthetic aperture radar (SAR) with applications to imaging of the ocean surface," *Proceedings of the IEEE*, vol. 66, no. 5, pp. 563–583, 1978.

[21] J. P. Fitch, *Synthetic aperture radar*. Springer Science & Business Media, 2012.

[22] M. Nordquist, S. N. Nandan *et al.*, *United Nations Convention on the Law of the Sea 1982, Volume VII: A Commentary*. Martinus Nijhoff Publishers, 2011, vol. 7.

[23] M. Gade, W. Alpers, H. Hühnerfuss, H. Masuko, and T. Kobayashi, "Imaging of biogenic and anthropogenic ocean surface films by the multifrequency/multipolarization SIR-C/X-SAR," *Journal of Geophysical Research: Oceans*, vol. 103, no. C9, pp. 18 851–18 866, 1998.

[24] K. Vyas, P. Shah, U. Patel, T. Zaveri *et al.*, "Oil spill detection from sar image data for remote monitoring of marine pollution using light weight imagej implementation," in *Engineering (NUiCONE), 2015 5th Nirma University International Conference on*. IEEE, 2015, pp. 1–6.

[25] M. Fingas, B. Fieldhouse, and P. Jokuty, "Vegetable oil spills: oil properties and behaviour," *Handbook Oil Spill Science Technology*, vol. 79, 2014.

[26] J. L. Ramseur, "Deepwater horizon oil spill: the fate of the oil," in *Congressional Research Service, Library of Congress Washington, DC*, 2010.

[27] National Research Council (US). Steering Committee for the Petroleum in the Marine Environment Update, *Oil in the sea: inputs, fates, and effects*. National Academies, 1985, vol. 1.

[28] K. Grüner, R. Reuter, and H. Smid, "A new sensor system for airborne measurements of maritime pollution and of hydrographic parameters," *GeoJournal*, vol. 24, no. 1, pp. 103–117, 1991.

[29] Exxon Valdez Oil Spill Trustee Council. Exxon Valdez tanker Image Gallery. http://www.evostc.state.ak.us/static/images/. Accessed: 2018-03-20.

[30] Y. Zhang, Y. Li, and H. Lin, "Oil-spill pollution remote sensing by synthetic aperture radar," *Advanced Geoscience Remote Sensing*, 2014.

[31] International Tanker Owners Pollution Federation (ITOPF). (2018) Oil tanker spill statistics 2017. http://www.itopf.com/fileadmin/data/Photos/Statistics/Oil_Spill_Stats_2017_web.pdf. Accessed: 2018-02-13.

[32] K. N. Topouzelis, "Oil spill detection by SAR images: dark formation detection, feature extraction and classification algorithms," *Sensors*, vol. 8, no. 10, pp. 6642–6659, 2008.

[33] C. Yang, Z. Wang, B. P. Hollebone, C. E. Brown, Z. Yang, and M. Landriault, "Chromatographic fingerprinting analysis of crude oils and petroleum products," *Handbook of oil spill science and technology*, pp. 93–163, 2015.

[34] G. Ferraro, S. Meyer-Roux, O. Muellenhoff, M. Pavliha, J. Svetak, D. Tarchi, and K. Topouzelis, "Long term monitoring of oil spills in european seas," *International Journal of Remote Sensing*, vol. 30, no. 3, pp. 627–645, 2009.

[35] National Ocean Service, National Oceanic and Atmospheric Administration (NOAA). Deepwater horizon image gallary. https://oceanservice.noaa.gov/deepwaterhorizon/images/. Accessed: 2018-03-20.

[36] J. B. Curtis, "Vessel-source oil pollution and marpol 73/78: an international success story," *Envtl. L.*, vol. 15, p. 679, 1984.

[37] B. Hollebone, "Measurement of oil physical properties," in *Oil Spill Science and Technology*. Elsevier, 2011, pp. 63–86.

[38] Y. Shu, J. Li, H. Yousif, and G. Gomes, "Dark-spot detection from SAR intensity imagery with spatial density thresholding for oil-spill monitoring," *Remote Sensing of Environment*, vol. 114,

no. 9, pp. 2026–2035, 2010.

[39] D. O'Rourke and S. Connolly, "Just oil? the distribution of environmental and social impacts of oil production and consumption," *Annual Review of Environment and Resources*, vol. 28, no. 1, pp. 587–617, 2003.

[40] I. MacDonald, "Deepwater disaster: How the oil spill estimates got it wrong," *Significance*, vol. 7, no. 4, pp. 149–154, 2010.

[41] C. H. Peterson, "The" exxon valdez" oil spill in alaska: acute, indirect and chronic effects on the ecosystem," *Advances in Marine Biology*, vol. 39, pp. 1–103, 2001.

[42] M. Migliaccio, M. Tranfaglia, and S. A. Ermakov, "A physical approach for the observation of oil spills in SAR images," *IEEE Journal of Oceanic Engineering*, vol. 30, no. 3, pp. 496–507, 2005.

[43] C. Camphuysen, "Chronic oil pollution in europe, a status report," *Report Royal Netherlands Institute for Sea Research, commissioned by International Fund for Animal Welfare (IFAW), Brussels*, 2007.

[44] J. Lu, "Marine oil spill detection, statistics and mapping with ERS SAR imagery in south-east Asia," *International Journal of Remote Sensing*, vol. 24, no. 15, pp. 3013–3032, 2003.

[45] F. K. Wiese and G. J. Robertson, "Assessing seabird mortality from chronic oil discharges at sea," *Journal of Wildlife Management*, vol. 68, no. 3, pp. 627–638, 2004.

[46] J. F. Piatt and R. G. Ford, "How many seabirds were killed by the exxon valdez oil spill," in *American Fisheries Society Symposium*, vol. 18, no. 1993, 1996, pp. 2–5.

[47] L. H. Schwacke, C. R. Smith, F. I. Townsend, R. S. Wells, L. B. Hart, B. C. Balmer, T. K. Collier, S. De Guise, M. M. Fry, L. J. Guillette Jr *et al.*, "Health of common bottlenose dolphins (tursiops truncatus) in barataria bay, louisiana, following the deepwater horizon oil spill," *Environmental science & technology*, vol. 48, no. 1, pp. 93–103, 2013.

[48] K. Topouzelis, D. Tarchi, M. Vespe, M. Posada, O. Muellenhoff, and G. Ferraro, "Detection, tracking, and remote sensing," *Handbook of Oil Spill Science and Technology*, pp. 357–383, 2015.

[49] International Maritime Organization (IMO), "Visibility limits of oil discharges of annex I of MARPOL 73/78," Maritime Environment protection Committee, MEPC Resolution 61(34), Tech. Rep., 1993.

[50] G. Mattson, "Marpol 73/78 and annex i: an assessment of its effectiveness," *Journal of International Wildlife Law and Policy*, vol. 9, no. 2, pp. 175–194, 2006.

[51] A. H. S. Solberg, C. Brekke, and P. O. Husøy, "Oil spill detection in Radarsat and Envisat SAR images," *IEEE Transactions on Geoscience and Remote Sensing*, vol. 45, no. 3, pp. 746–754, 2007.

[52] G. Ferraro, B. Baschek, G. de Montpellier, O. Njoten, M. Perkovic, and M. Vespe, "On the SAR derived alert in the detection of oil spills according to the analysis of the EGEMP." *Marine pollution bulletin*, vol. 60, no. 1, pp. 91–102, 2010.

[53] R. Meyer, C. Schwegmann, and W. Kleynhans, "Vessel classification features using spatial bayesian inference from historical ais data," in *International Geoscience and Remote Sensing Symposium (IGARSS)*. IEEE, 2017, pp. 2629–2632.

[54] J. A. Richards, "Sources and characteristics of remote sensing image data," in *Remote Sensing Digital Image Analysis*. Springer, 1993, pp. 1–37.

[55] M. I. Skolnik, "Introduction to radar," *Radar Handbook*, vol. 2, 1962.

[56] A. Prakash, "Thermal remote sensing: concepts, issues and applications," *International Archives of Photogrammetry and Remote Sensing*, vol. 33, no. B1; PART 1, pp. 239–243, 2000.

[57] F. T. Ulaby, R. K. Moore, and A. K. Fung, "Microwave remote sensing: Active and passive, volume ii: Radar remote sensing and surface scattering and emission theory," *Artech house*, p.

855, 1982.

[58] M. Fingas and C. Brown, "Review of oil spill remote sensing," *Marine pollution bulletin*, vol. 83, no. 1, pp. 9–23, 2014.

[59] R. Goodman, "Overview and future trends in oil spill remote sensing," *Spill Science & Technology Bulletin*, vol. 1, no. 1, pp. 11–21, 1994.

[60] O. McMahon, T. Murphy, and E. Brown, "Remote measurement of oil spill thickness," Environmental Research Institute of Michigan, Ann Arbor, MI (United States), Tech. Rep., 1997.

[61] C. P. Schwegmann, W. Kleynhans, J. Engelbrecht, L. W. Mdakane, and R. G. Meyer, "Subsidence feature discrimination using deep convolutional neural networks in synthetic aperture radar imagery," in *International Geoscience and Remote Sensing Symposium (IGARSS)*. IEEE, 2017, pp. 4626–4629.

[62] M. Soumekh, *Synthetic aperture radar signal processing*. New York: Wiley, 1999, vol. 7.

[63] C. Elachi and J. J. Van Zyl, *Introduction to the physics and techniques of remote sensing*. John Wiley & Sons, 2006, vol. 28.

[64] C. Oliver and S. Quegan, *Understanding synthetic aperture radar images*. SciTech Publishing, 2004.

[65] C. P. Schwegmann, W. Kleynhans, B. Salmon, L. W. Mdakane, and R. G. Meyer, "Synthetic aperture radar ship discrimination, generation and latent variable extraction using information maximizing generative adversarial networks," in *International Geoscience and Remote Sensing Symposium (IGARSS)*. IEEE, 2017, pp. 2263–2266.

[66] R. G. Meyer, W. Kleynhans, and C. P. Schwegmann, "Small ships don't shine: Classification of ocean vessels from low resolution, large swath area SAR acquisitions," in *International Geoscience and Remote Sensing Symposium (IGARSS)*. IEEE, 2016, pp. 975–978.

[67] K. Ouchi, "Recent trend and advance of synthetic aperture radar with selected topics," *Remote Sensing*, vol. 5, no. 2, pp. 716–807, 2013.

[68] C. V. Jakowatz, D. E. Wahl, P. H. Eichel, D. C. Ghiglia, and P. A. Thompson, *Spotlight-Mode Synthetic Aperture Radar: A Signal Processing Approach*. Springer Science & Business Media, 2012.

[69] European Space Agency (ESA), "Sentinel-1 product handbook," https://sentinel.esa.int/documents/247904/685163/Sentinel-1_User_Handbook, 2013, accessed:2018-02-16.

[70] C. Oliver, "Synthetic-aperture radar imaging," *Journal of Physics D: Applied Physics*, vol. 22, no. 7, p. 871, 1989.

[71] J.-S. Lee and E. Pottier, *Polarimetric radar imaging: from basics to applications*. CRC press, 2009.

[72] K. Hasselmann, R. Raney, W. Plant, W. Alpers, R. Shuchman, D. R. Lyzenga, C. Rufenach, and M. Tucker, "Theory of synthetic aperture radar ocean imaging: A MARSEN view," *Journal of Geophysical Research: Oceans*, vol. 90, no. C3, pp. 4659–4686, 1985.

[73] M. Gade and W. Alpers, "Using ERS-2 SAR images for routine observation of marine pollution in European coastal waters," *Science of the Total Environment*, vol. 237-238, no. July 2015, pp. 441–448, 1999.

[74] I. Lin and V. Khoo, "Computer-based algorithm for ship detection from ERS-SAR imagery," in *Third ERS Symposium on Space at the service of our Environment*, vol. 414, 1997, p. 1411.

[75] T. Wahl, K. Eldhuset, and A. Skoelv, "Ship traffic monitoring using the ERS-1 SAR," *European Space Agency-Publications-ESA SP*, vol. 359, pp. 823–823, 1993.

[76] H. A. Espedal, O. M. Johannessen, J. A. Johannessen, E. Dano, D. Lyzenga, and J. Knulst, "COASTWATCH'95: ERS 1/2 SAR detection of natural film on the ocean surface," *Journal of*

Geophysical Research: Oceans, vol. 103, no. C11, pp. 24 969–24 982, 1998.

[77] U. Gessner, M. Machwitz, T. Esch, A. Tillack, V. Naeimi, C. Kuenzer, and S. Dech, "Multi-sensor mapping of west african land cover using modis, asar and tandem-x/terrasar-x data," *Remote Sensing of Environment*, vol. 164, pp. 282–297, 2015.

[78] D. Perissin, Z. Wang, and H. Lin, "Shanghai subway tunnels and highways monitoring through cosmo-skymed persistent scatterers," *ISPRS Journal of Photogrammetry and Remote Sensing*, vol. 73, pp. 58–67, 2012.

[79] T. Esch, M. Marconcini, A. Felbier, A. Roth, W. Heldens, M. Huber, M. Schwinger, H. Taubenböck, A. Müller, and S. Dech, "Urban footprint processor - fully automated processing chain generating settlement masks from global data of the tandem-x mission," *IEEE Geoscience and Remote Sensing Letters*, vol. 10, no. 6, pp. 1617–1621, 2013.

[80] S. Martin, *An introduction to ocean remote sensing*. Cambridge University Press, 2014.

[81] G. L. Turin, "An introduction to digitial matched filters," *Proceedings of the IEEE*, vol. 64, no. 7, pp. 1092–1112, 1976.

[82] C. Elachi, "Spaceborne radar remote sensing: applications and techniques," *New York, IEEE Press, 1988, 285 p.*, 1988.

[83] P. and C.J.Oliver, "Optimum detection and segmentation of oil-slicks," in *IEEE Proceedings - Radar, Sonar and Navigation*, vol. 147, no. 6, 2000, pp. 309–321.

[84] W. M. Brown, "Synthetic aperture radar," *IEEE Transactions on Aerospace and Electronic Systems*, no. 2, pp. 217–229, 1967.

[85] J. J. van Zyl, *Synthetic aperture radar polarimetry*. John Wiley & Sons, 2011, vol. 2.

[86] J. J. van Zyl and K. Yunjin, *Synthetic aperture radar polarimetry*. John Wiley & Sons, 2010, vol. 1.

[87] L. Chang, Z. Tang, S. Chang, and Y. Chang, "A region-based GLRT detection of oil spills in SAR images," in *Pattern Recognition Letters*, vol. 29, no. 14, 2008, pp. 1915–1923.

[88] J. P. Fitch, "Synthetic Aperture Radar," *New York, Springer-Verlag, 1988*, 1988.

[89] Y. L. Neo, F. H. Wong, and I. G. Cumming, "Processing of azimuth-invariant bistatic SAR data using the range doppler algorithm," *IEEE Transactions on Geoscience and Remote Sensing*, vol. 46, no. 1, pp. 14–21, 2008.

[90] A. Moreira, P. Prats-iraola, M. Younis, G. Krieger, I. Hajnsek, and K. P. Papathanassiou, "A Tutorial on Synthetic Aperture Radar," *IEEE Geoscience and Remote Sensing Magazine*, no. March, pp. 6–43, 2013.

[91] R. Bamler, "Principles of synthetic aperture radar," *Surveys in Geophysics*, vol. 21, no. 2-3, pp. 147–157, 2000.

[92] J. W. Goodman, "Some fundamental properties of speckle," *JOSA*, vol. 66, no. 11, pp. 1145–1150, 1976.

[93] F. Argenti, A. Lapini, L. Alparone, and T. Bianchi, "A Tutorial on Speckle Reduction in Synthetic Aperture Radar Images," *IEEE Geoscience and Remote Sensing Magazine*, no. September, 2013.

[94] G. R. Valenzuela, "Theories for the interaction of electromagnetic and oceanic waves–a review," *Boundary-Layer Meteorology*, vol. 13, no. 1-4, pp. 61–85, 1978.

[95] W. Alpers and H. A. Espedal, "Oils and surfactants," *SAR marine user's manual*, pp. 263–275, 2004.

[96] D. B. Ross, J. Overland, W. J. Plerson Jr, V. J. Cardone, R. D. McPherson, and T.-W. Yu, "Oceanic surface winds," in *Advances in Geophysics*, vol. 27. Elsevier, 1985, pp. 101–140.

[97] A.H.S Solberg and R Solberg, "A large-scale evaluation of features for automatic detection of oil spills in ERS SAR images," in *International Geoscience and Remote Sensing Symposium (IGARSS)*, vol. 3. IEEE, 1996, pp. 1484–1486.

[98] P. Liu, C. Zhao, X. Li, M. He, and W. Pichel, "Identification of ocean oil spills in SAR imagery based on fuzzy logic algorithm," *International Journal of Remote Sensing*, vol. 31, no. 17-18, pp. 4819–4833, 2010.

[99] J. Kim, D. Kim, S. Kim, and B. Hwang, "Iceberg detection using full-polarimetric radarsat-2 sar data in west antarctica," in *Synthetic Aperture Radar (APSAR), 2011 3rd International Asia-Pacific Conference*. IEEE, 2011, pp. 1–4.

[100] C. P. Schwegmann, W. Kleynhans, and B. P. Salmon, "Manifold adaptation for constant false alarm rate ship detection in south african oceans," in *IEEE Journal of Selected Topics in Applied Earth Observations and Remote Sensing*, vol. 8, no. 7. IEEE, 2015, pp. 3329–3337.

[101] C. P. Schwegmann, W. Kleynhans, B. P. Salmon, L. W. Mdakane, and R. G. Meyer, "Very deep learning for ship discrimination in synthetic aperture radar imagery," in *International Geoscience and Remote Sensing Symposium (IGARSS)*. IEEE, 2016, pp. 104–107.

[102] P. Trivero and W. Biamino, "Observing marine pollution with synthetic aperture radar," in *Geoscience and remote sensing new achievements*. InTech, 2010.

[103] M. K. Hsu, A. K. Liu, and C. Liu, "A study of internal waves in the china seas and yellow sea using SAR," *Continental Shelf Research*, vol. 20, no. 4-5, pp. 389–410, 2000.

[104] P. Heimbach and K. Hasselmann, "Development and application of satellite retrievals of ocean wave spectra," in *Elsevier oceanography series*, vol. 63. Elsevier, 2000, pp. 5–33.

[105] A. Y. Ivanov and A. I. Ginzburg, "Oceanic eddies in synthetic aperture radar images," *Journal of Earth System Science*, vol. 111, no. 3, p. 281, 2002.

[106] R. Gens, "Oceanographic applications of SAR remote sensing," *GIS & Remote Sensing*, vol. 45, no. 3, pp. 275–305, 2008.

[107] A. H. S. Solberg, "Remote sensing of ocean oil-spill pollution," *Proceedings of the IEEE*, vol. 100, no. 10, pp. 2931–2945, 2012.

[108] G. Staples and D. F. Rodrigues, "Maritime environmental surveillance with radarsat-2," in *XVI Brazilian Remote Sensing Symposium (SBSR)*, 2013, pp. 8445–8452.

[109] M. Migliaccio, A. Gambardella, and M. Tranfaglia, "SAR polarimetry to observe oil spills," *IEEE Transactions on Geoscience and Remote Sensing*, vol. 45, no. 2, pp. 506–511, 2007.

[110] M. Migliaccio, F. Nunziata, and A. Gambardella, "On the co-polarized phase difference for oil spill observation M." *International Journal of Remote Sensing*, vol. 30, no. 6, pp. 1587–1602, 2009.

[111] M. Indregard, A. Solberg, and P. Clayton, "D2-report on benchmarking oil spill recognition approaches and best practice," *Oceanides project, European Commision*, 2004.

[112] F. Del Frate, A. Petrocchi, J. Lichtenegger, and G. Calabresi, "Neural networks for oil spill detection using ERS-SAR data," *IEEE Transactions on geoscience and remote sensing*, vol. 38, no. 5, pp. 2282–2287, 2000.

[113] G. Suresh, C. Melsheimer, J.-H. Körber, and G. Bohrmann, "Automatic estimation of oil seep locations in synthetic aperture radar images," *IEEE Transactions on Geoscience Electronics*, vol. 53, no. 8, pp. 4218–4230, 2015.

[114] A. H. S. Solberg, C. Brekke, and P. O. Husoy, "Oil spill detection in radarsat and envisat SAR images," *IEEE Transactions on Geoscience Electronics*, vol. 45, no. 3, pp. 746–755, 2007.

[115] Y. D. Y. Dong, A. Milne, and B. Forster, "A review of SAR speckle filters: texture restoration and preservation," in *International Geoscience and Remote Sensing Symposium (IGARSS)*, vol. 2. IEEE, 2000, pp. 0–2.

[116] S. Goze and A. Lopes, "A MMSE speckle filter for full resolution SAR polarimetric data," *Journal of electromagnetic waves and applications*, vol. 7, no. 5, pp. 717–737, 1993.

[117] J. Lee, M. R. Grunes, and S. A. Mango, "Speckle reduction in multipolarization, multifrequency SAR imagery," *IEEE Transactions on Geoscience and remote sensing*, vol. 29, no. 4, pp. 535–544, 1991.

[118] L. M. Novak and M. C. Burl, "Optimal speckle reduction in polarimetric SAR imagery," *IEEE Transactions on Aerospace and Electronic Systems*, vol. 26, no. 2, pp. 293–305, 1990.

[119] J. S. Lee, M. R. Grunes, and G. De Grandi, "Polarimetric SAR speckle filtering and its implication for classification," *IEEE Transactions on Geoscience and remote sensing*, vol. 37, no. 5, pp. 2363–2373, 1999.

[120] Y. Domg, A. K. Milne *et al.*, "Toward edge sharpening: a SAR speckle filtering algorithm," *IEEE Transactions on Geoscience and Remote Sensing*, vol. 39, no. 4, pp. 851–863, 2001.

[121] J.-S. Lee, "Refined filtering of image noise using local statistics," *Computer graphics and image processing*, vol. 15, no. 4, pp. 380–389, 1981.

[122] V. S. Frost, J. A. Stiles, K. S. Shanmugan, and J. C. Holtzman, "A model for radar images and its application to adaptive digital filtering of multiplicative noise," *IEEE Transactions on pattern analysis and machine intelligence*, no. 2, pp. 157–166, 1982.

[123] D. Kuan, A. Sawchuk, T. Strand, and P. Chavel, "Adaptive restoration of images with speckle," *IEEE Transactions on Acoustics, Speech, and Signal Processing*, vol. 35, no. 3, pp. 373–383, 1987.

[124] F. Argenti, T. Bianchi, and L. Alparone, "Multiresolution MAP despeckling of SAR images based on locally adaptive generalized Gaussian pdf modeling," *IEEE Transactions on Image Processing*, vol. 15, no. 11, pp. 3385–3399, 2006.

[125] H. Espedal, "Satellite SAR oil spill detection using wind history information," *International Journal of Remote Sensing*, vol. 20, no. 1, pp. 49–65, 1999.

[126] L. Salvatori, S. Bouchaib, F. Frate, J. Lichtenneger, and Y. Samara, "Estimating the wind vector from radar SAR images when applied to the detection of oil spill pollution," in *International Symposium on GIS and Computer Cartography for Coastal Zone Management*, 2003.

[127] A. El-Zaart and A. A. Ghosn, "Sar images thresholding for oil spill detection," in *Electronics, Communications and Photonics Conference (SIECPC), 2013 Saudi International*. IEEE, 2013, pp. 1–5.

[128] T. F. N. Kanaa, E. Tonye, G. Mercier, V. d. P. Onana, J. M. Ngono, P. L. Frison, J. P. Rudant, and R. Garello, "Detection of oil slick signatures in SAR images by fusion of hysteresis thresholding responses," in *International Geoscience and Remote Sensing Symposium (IGARSS)*, vol. 4. IEEE, 2003, pp. 2750–2752.

[129] A. Gasull, X. Fabregas, J. Jiménez, F. Marqués, V. Moreno, and M. A. Herrero, "Oil spills detection in SAR images using mathematical morphology," in *Signal Processing Conference, 2002 11th European*. IEEE, 2002, pp. 1–4.

[130] G. Suresh, G. Heygster, C. Melsheimer, and G. Bohrmann, "Natural oil seep location estimation in SAR images using direct and contextual information," in *International Geoscience and Remote Sensing Symposium (IGARSS)*. IEEE, 2014, pp. 1678–1681.

[131] F. Bandiera, A. Masciullo, and G. Ricci, "A bayesian approach to oil slicks edge detection based on SAR Data," *IEEE Transactions on Geoscience and Remote Sensing*, vol. 52, no. 5, pp. 2901–2909, 2014.

[132] K. Karantzalos and D. Argialas, "Automatic detection and tracking of oil spills in SAR imagery with level set segmentation," *International Journal of Remote Sensing*, vol. 29, no. 21, pp. 6281–6296, 2008.

[133] Y. Zhang, H. Lin, Q. Liu, J. Hu, X. Li, and K. Yeung, "Oil-spill monitoring in the coastal waters of hong kong and vicinity," *Marine Geodesy*, vol. 35, no. 1, pp. 93–106, 2012.

[134] K. Topouzelis, V. Karathanassi, P. Pavlakis, and D. Rokos, "Detection and discrimination between oil spills and look-alike phenomena through neural networks," *ISPRS Journal of Photogrammetry and Remote Sensing*, vol. 62, no. 4, pp. 264–270, 2007.

[135] B. Huang, H. Li, and X. Huang, "A level set method for oil slick segmentation in SAR images," *International Journal of Remote Sensing*, vol. 26, no. 6, pp. 1145–1156, 2005.

[136] S. Singha, T. J. Bellerby, and O. Trieschmann, "Satellite Oil Spill Detection Using Artificial Neural Networks," *IEEE Journal of selected topics in applied earth observations and remote sensing*, vol. 6, no. 6, pp. 2355–2363, 2013.

[137] O. Garcia-Pineda, I. R. MacDonald, X. Li, C. R. Jackson, and W. G. Pichel, "Oil spill mapping and measurement in the gulf of mexico with Textural Classifier Neural Network Algorithm (TCNNA)," *IEEE Journal of Selected Topics in Applied Earth Observations and Remote Sensing*, vol. 6, no. 6, pp. 2517–2525, 2013.

[138] K. Topouzelis, D. Stathakis, and V. Karathanassi, "Investigation of genetic algorithms contribution to feature selection for oil spill detection," *International Journal of Remote Sensing*, vol. 30, no. 3, pp. 611–625, 2009.

[139] R. M. Haralick, "Statistical and structural approaches to texture," in *Proceedings of the IEEE*, vol. 67, no. 5. IEEE, 1979, pp. 786–804.

[140] P. Liu and C. Zhao, "Oil Spill Identification in Marine SAR Images Based on Texture Feature and Fuzzy Logic System," in *2009 Sixth International Conference on Fuzzy Systems and Knowledge Discovery*, 2009, pp. 433–437.

[141] D. Stathakis, K. Topouzelis, and V. Karathanassi, "Large-scale feature selection using evolved neural networks," in *Remote Sensing*, vol. 6365, no. 5, 2006, pp. 636 513–636 513–9.

[142] F. Nirchio, M. Sorgente, A. Giancaspro, W. Biamino, R. Ravera, G. S. Centre, and G. S. Centre, "Automatic detection of oil spills from SAR images," *International Journal of Remote Sensing*, vol. 26, no. 6, pp. 1157–1174, 2007.

[143] O. Garcia-Pineda, B. Zimmer, M. Howard, W. Pichel, X. Li, and I. R. MacDonald, "Using SAR images to delineate ocean oil slicks with a texture-classifying neural network algorithm (TCNNA)," *Canadian Journal of Remote Sensing*, vol. 35, no. 5, pp. 411–421, 2009.

[144] S. Kubat, Miroslav and Holte, Robert C and Matwin and F. Provost, "Machine Learning for the Detection of Oil Spills in Satellite Radar Images," *Machine learning*, vol. 215, pp. 195–215, 1998.

[145] A. K. Jain, R. P. W. Duin, and J. Mao, "Statistical pattern recognition: A review," *IEEE Transactions on pattern analysis and machine intelligence*, vol. 22, no. 1, pp. 4–37, 2000.

[146] B. Fiscella, a. Giancaspro, F. Nirchio, P. Pavese, and P. Trivero, "Oil spill detection using marine SAR images," *International Journal of Remote Sensing*, vol. 21, no. 18, pp. 3561–3566, 2000.

[147] T. W. Anderson, T. W. Anderson, T. W. Anderson, T. W. Anderson, and E.-U. Mathématicien, *An introduction to multivariate statistical analysis*. Wiley New York, 1958, vol. 2.

[148] K. Topouzelis and A. Psyllos, "Oil spill feature selection and classification using decision tree forest on SAR image data," *ISPRS Journal of Photogrammetry and Remote Sensing*, vol. 68, pp. 135–143, 2012.

[149] S. Chehresa, A. Amirkhani, G. A. Rezairad, and M. R. Mosavi, "Optimum features selection for oil spill detection in SAR image," *Journal of the Indian Society of Remote Sensing*, vol. 44, no. 5, pp. 775–787, 2016.

[150] M. Konik and K. Bradtke, "Object-oriented approach to oil spill detection using envisat ASAR images," *ISPRS Journal of Photogrammetry and Remote Sensing*, vol. 118, pp. 37–52, 2016.

[151] I. Keramitsoglou, C. Cartalis, and C. T. Kiranoudis, "Automatic identification of oil spills on satellite images," *Environmental modelling & software*, vol. 21, no. 5, pp. 640–652, 2006.

[152] A. Gambardella, G. Giacinto, M. Migliaccio, and A. Montali, "One-class classification for oil spill detection," *Pattern Analysis and Applications*, vol. 13, no. 3, pp. 349–366, 2010.

[153] M. Barni, M. Betti, and A. Mecocci, "A fuzzy approach to oil spill detection an SAR images," in *International Geoscience and Remote Sensing Symposium (IGARSS)*, vol. 1. IEEE, 1995, pp. 157–159.

[154] K. Topouzelis, V. Karathanassi, P. Pavlakis, and D. Rokos, "Oil spill detection: SAR multiscale segmentation and object features evaluation," in *Remote Sensing of the Ocean and Sea Ice*, vol. 4880. International Society for Optics and Photonics, 2003, pp. 77–88.

[155] L. A. Zadeh, "Toward a theory of fuzzy information granulation and its centrality in human reasoning and fuzzy logic," *Fuzzy sets and systems*, vol. 90, no. 2, pp. 111–127, 1997.

[156] Y. Jing, J. An, and Z. Liu, "A novel edge detection algorithm based on global minimization active contour model for oil slick infrared aerial image," *IEEE Transactions on Geoscience and Remote Sensing*, vol. 49, no. 6, pp. 2005–2013, 2011.

[157] C. McLaughlin, D. Falatko, R. Danesi, and R. Albert, "Characterizing shipboard bilgewater effluent before and after treatment," *Environmental Science and Pollution Research*, vol. 21, no. 8, pp. 5637–5652, 2014.

[158] N. Miranda, P. Meadows, D. TYPE, and T. NOTE, "Radiometric calibration of S-1 level-1 products generated by the S-1 IPF," *Viewed at https://sentinel.esa.int/documents/247904/685163/S1-Radiometric-Calibration-V1.0.pdf*, 2015.

[159] A. Lopes, R. Touzi, and E. Nezry, "Adaptive speckle filters and scene heterogeneity," *IEEE Transactions on Geoscience and Remote Sensing*, vol. 28, no. 6, pp. 992–1000, 1990.

[160] J.-S. Lee, "Digital image enhancement and noise filtering by use of local statistics," *IEEE transactions on pattern analysis and machine intelligence*, no. 2, pp. 165–168, 1980.

[161] N. Otsu, "A threshold selection method from gray-level histograms," *Automatica*, vol. 11, no. 285-296, pp. 23–27, 1975.

[162] K. Zhang, L. Zhang, H. Song, and W. Zhou, "Active contours with selective local or global segmentation: a new formulation and level set method," *Image and Vision comp.*, vol. 28, no. 4, pp. 668–676, 2010.

[163] I. Sobel, "An isotropic 3× 3 image gradient operator," *Machine vision for three-dimensional scenes*, pp. 376–379, 1990.

[164] W. Gao, X. Zhang, L. Yang, and H. Liu, "An improved sobel edge detection," *Computer Science and Information Technology (ICCSIT), 2010 3rd IEEE International Conference on*, vol. 5, pp. 67–71, 2010.

[165] P. Pudil, J. Novovičová, and J. Kittler, "Floating search methods in feature selection," *Pattern recognition letters*, vol. 15, no. 11, pp. 1119–1125, 1994.

[166] M. B. Brown and A. B. Forsythe, "Robust tests for the equality of variances," *Journal of the American Statistical Association*, vol. 69, no. 346, pp. 364–367, 1974.

[167] L. Breiman, J. Friedman, C. J. Stone, and R. A. Olshen, *Classification and regression trees*. CRC press, 1984.

[168] J. Friedman, T. Hastie, and R. Tibshirani, *The elements of statistical learning*. Springer series in statistics New York, 2001, vol. 1.

[169] European Space Agency (ESA) - Sentinel Online, https://sentinel.esa.int/web/sentinel/missions/sentinel-1/observation-scenario/archive , accessed: 2018-03-27.

[170] MDA. Radarsat-2 product description. http://mdacorporation.com/docs/default-source/technical-documents/geospatial-services/52-1238_rs2_product_description.pdf. Accessed: 2017-01-10.

[171] J.-M. Nicolas, S. Le Hégarat-Mascle, F. Adragna, A. Lopès, R. Garello, F. Tupin, D. Ducrot, H. Maître, E. Trouvé, and J.-M. Le Caillec, *Processing of synthetic aperture radar images*. Wiley Online Library, 2008.

[172] T. Fawcett, "An introduction to roc analysis," *Pattern recognition letters*, vol. 27, no. 8, pp. 861–874, 2006.

[173] D. Chaudhuri, A. Samal, A. Agrawal, A. Mishra, V. Gohri, and R. C. Agarwal, "A Statistical Approach for Automatic Detection of Ocean Disturbance Features From SAR Images," *Selected Topics in Applied Earth Observations and Remote Sensing, IEEE Journal of*, vol. 5, no. 4, pp. 1231–1242, 2012.

[174] C. Li, C. Y. Kao, J. C. Gore, and Z. Ding, "Minimization of region-scalable fitting energy for image segmentation," *IEEE Transactions on Image Processing*, vol. 17, no. 10, pp. 1940–1949, 2008.

[175] H. Song, B. Huang, and K. Zhang, "A Globally Statistical Active Contour Model for Segmentation of Oil Slick in SAR Imagery," *IEEE Journal of Selected Topics in Applied Earth Observations and Remote sensing*, vol. 6, no. 6, pp. 2402–2409, 2013.

[176] S. Robla, E. G. Sarabia, J. R. Llata, C. Torre-Ferrero, and J. Pérez Oria, "An approach for detecting and tracking oil slicks on satellite images," *MTS/IEEE Seattle, OCEANS*, 2010.

[177] V. Karathanassi, K. Topouzelis, P. Pavlakis, and D. Rokos, "An object-oriented methodology to detect oil spills," *International Journal of Remote Sensing*, vol. 27, no. 23, pp. 5235–5251, 2006.